Simulation of a concept for a compact ultrafast X-ray pulse source based on RF and THz technologies

T. Vinatier[1,†], R. W. Assmann[1], U. Dorda[1], F. Lemery[1], B. Marchetti[1]
[1]Deutsches Elektronen Synchrotron, Notkestrasse 85, 22607 Hamburg, Germany
[†]Corresponding author: thomas.vinatier@desy.de

Abstract
We study through simulations a layout mixing RF and THz technologies for a compact ultrafast X-ray pulse source based on Inverse Compton Scattering (ICS), aiming to deliver few femtoseconds to sub-femtosecond pulses. The layout consists of an S-band gun as electron source and a dielectric-loaded circular waveguide driven by a multicycle THz pulse to accelerate and longitudinally compress the bunch, before X-ray generation via ICS with a laser pulse. We detail several schemes allowing optimizing the electron bunch properties. This optimization leads to a preliminary layout and various working points able to deliver 0.1 to 5 pC bunches, ranging from 15 to 18 MeV average kinetic energy, 0.4 to 5 fs rms length, 0.1 to 2.6% rms energy spread and 5 to 13 µm rms transverse size. Simultaneously, the beamline is kept compact (≈ 1.3 m up to the ICS point), which has not yet been achieved using only conventional RF technologies. The properties of the X-ray pulse are investigated with simulations, showing the possibility to tune its energy between 2.9 and 11.5 keV. For 400 mJ of laser energy, $1.5*10^4$ to $7.7*10^4$ photons/pulse in 1.5% rms bandwidth or $6.2*10^3$ to $3.5*10^4$ photons/pulse with lower bandwidths (0.56 to 1.5% rms along the energy range) can be expected. The properties of the dielectric-loaded waveguide and of the THz pulse driving it, the state-of-the-art of the THz pulse generation schemes and the influence of various jitters and the limits that they should not exceed for a reasonably stable operation are finally given.

1. Introduction

A concept for a compact X-ray source aiming to deliver fs to sub-fs X-ray pulses through Inverse Compton Scattering (ICS) has been recently presented by the authors in Ref. 1. This concept is based on the use of a conventional S-band RF gun as electron bunch source and injector for a THz[a] linac consisting in a cylindrical partially dielectric-loaded waveguide (DLW), as depicted in Fig. 1. The latter is driven by a multi-cycle THz pulse which is used to simultaneously accelerate the electron bunch up to 15-20 MeV and compress it to an rms length on the single femtosecond order or below. The S-band gun assumed in our study is a 1.6 cells gun operating at 2.9985 GHz with its peak field amplitude fixed to 140 MV/m, which corresponds to the maximal gradient experimentally achieved with a BNL/SLAC/UCLA gun[2,3]. A schematic layout of the concept is displayed in Fig. 2. This hybrid concept is studied within the context of the AXSIS project[4] at DESY, where AXSIS stands for Attosecond X-ray Science: Imaging and Spectroscopy. The AXSIS project is funded by an ERC grant and aims to develop a compact ultrafast X-ray pulse source based on the use of THz accelerating fields. The reasons leading to study this hybrid concept in parallel with the fully THz-driven one intended as a baseline design for the AXSIS project have been exposed in details in our previous article[1]. The main one is that the THz guns are still in the early phase of their development[5-7] and that several technical and beam dynamics challenges have to be overcome before the delivered electron bunch properties can approach the ones delivered by the current state-of-the-art S-band guns, which are nowadays still the best sources to provide ultrashort and high-brightness electron bunches. Furthermore, when dealing with developing technologies, it is always preferable to introduce only one part at a time (the THz linac for the concept we are developing) and to keep the other components conservative and well-established.

The study performed in Ref. 1 was based on start-to-end beam dynamics simulations from the photocathode up to the ICS point (excluding the interaction with the laser), used to explain the relevant physical phenomena involved in each part of the layout shown in Fig. 2 and the choices made to fix the values of some parameters. A first set of simulated bunch properties at the ICS point was also presented, revealing the excellent potential of the proposed concept to be a compact source delivering fs to sub-fs X-ray pulses. The present article aims to continue this work by presenting various schemes enabling the optimization of the concept and the generation of significantly better transverse and longitudinal bunch properties at the ICS point, simulating the ICS interaction to evaluate the properties of the generated X-ray pulse for various working points and defining some of the technical requirements of the concept.

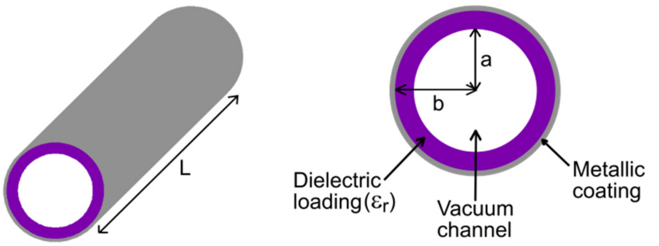

Fig. 1. Schematic of a cylindrical partially dielectric-loaded waveguide.

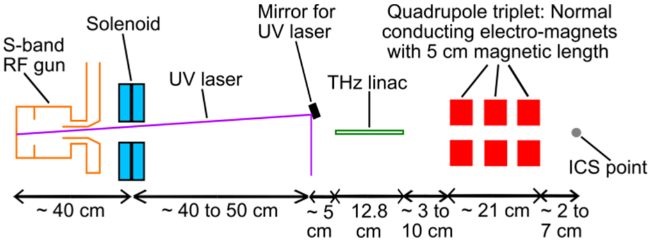

Fig. 2. Schematic layout of the ultrafast X-ray pulse source concept introduced in Ref. 1 and further developed in this paper.

Section 2 introduces the basic concepts and formulas for the cylindrical DLW used as accelerating structure. Section 3 presents several schemes to optimize the concept of compact ultrafast X-ray pulse source defined in Ref. 1. Especially in

---

[a] In this paper we consider the THz range of frequency as being between 100 GHz and 10 THz.

subsection 3.1, it is shown that an appropriate choice of the relative position of the transverse and longitudinal focal points after the quadrupole triplet (see Fig. 2) leads to a significant space-charge induced decrease of the electron bunch energy spread previously induced in the THz linac to generate longitudinal compression. In subsection 3.2, the improvement of the transverse and longitudinal bunch properties resulting from a simple transverse shaping of the UV laser pulse driving the S-band RF-gun is presented. Finally in subsection 3.3, the importance of the fine-tuning of the phase velocity of the THz pulse driving the linac is also reported. Section 4 presents the electron bunch properties simulated at the ICS point for various potential working points, before presenting simulation results for the X-ray pulse properties obtained after ICS interaction with a laser. Ways for extending the tunability range of the proposed X-ray source are also introduced. The fifth and last section deals with some of the technical requirements for the proposed concept of ultrafast X-ray pulse source: required properties for the cylindrical DLW and for the THz pulse driving it (including power); generation of the required THz power; impact of various jitters on the bunch properties simulated at the ICS point.

2. Basic concepts and formulas for cylindrical dielectric-loaded waveguides

The mode used for electron bunch acceleration and compression in the cylindrical DLW is the TM_{01} mode[8,9], for which the analytical expression in cylindrical coordinate (r,θ,z) can be expressed in its complex form as:

$$E_z = \begin{cases} E_{ml} J_0(k_1 r) e^{i(2\pi f t - k_z z + \varphi_0)} & if\ 0 \le r < a \\ A F_{00}(k_2 r) e^{i(2\pi f t - k_z z + \varphi_0)} & if\ a \le r \le b \end{cases}, \qquad (1)$$

$$E_r = \begin{cases} -\frac{i k_z E_{ml}}{k_1} J_0'(k_1 r) e^{i(2\pi f t - k_z z + \varphi_0)} & if\ 0 \le r < a \\ -\frac{i k_z A}{k_2} F_{00}'(k_2 r) e^{i(2\pi f t - k_z z + \varphi_0)} & if\ a \le r \le b \end{cases}, \qquad (2)$$

$$H_\theta = \begin{cases} -\frac{2 i \pi f \varepsilon_0 E_{ml}}{k_1} J_0'(k_1 r) e^{i(2\pi f t - k_z z + \varphi_0)} & if\ 0 \le r < a \\ -\frac{2 i \pi f \varepsilon_0 \varepsilon_r A}{k_2} F_{00}'(k_2 r) e^{i(2\pi f t - k_z z + \varphi_0)} & if\ a \le r \le b \end{cases}, \qquad (3)$$

$$A = E_{ml} \frac{J_0(k_1 a) Y_0(k_2 b)}{J_0(k_2 a) Y_0(k_2 b) - J_0(k_2 b) Y_0(k_2 a)},$$

$$F_{00}(k_2 r) = J_0(k_2 r) - \frac{J_0(k_2 b)}{Y_0(k_2 b)} Y_0(k_2 r),$$

where i is the complex number, a and b are the dimensions defined in Fig. 1, E_{ml} is the on-axis peak field, f the THz pulse central frequency, φ_0 a phase shift, t the time, c the speed of light in vacuum, v_{ph} the phase velocity of the THz pulse in the DLW, ε_0 the vacuum dielectric permittivity, ε_r the relative dielectric permittivity of the dielectric filling (assumed without losses), $k_z = 2\pi f/v_{ph}$, $k_1^2 = k_0^2 - k_z^2$, $k_2^2 = \varepsilon_r k_0^2 - k_z^2$ ($k_0 = 2\pi f/c$) and J_n and Y_n are respectively the Bessel function of the first kind and second kind (Neumann function)[10]. The prime symbol (′) indicates the first derivative of a function. The physical electromagnetic field in the DLW is simply given by the real part of Eqs. (1), (2) and (3). The constant A and the functions $F_{00}(k_2 r)$ and $F_{00}'(k_2 r)$ in Eqs. (1), (2) and (3) are real as long as k_2 is real (namely when $v_{ph} \ge c/\sqrt{\varepsilon_r}$) and become complex when k_2 becomes imaginary (namely when $v_{ph} < c/\sqrt{\varepsilon_r}$). In this paper, we consider only relativistic electron bunches (≥ 5 MeV) implying that for efficient acceleration v_{ph} has to be always very close to c (namely less than 0.5% different from c). A, $F_{00}(k_2 r)$ and $F_{00}'(k_2 r)$ are therefore always real in our study, since we assume $\varepsilon_r = 4.41$ (quartz), and we will consider only this case afterwards in the paper.

The first parameter to be fixed when designing a cylindrical DLW is the radius of the central vacuum channel a (see Fig. 1). It is first limited by the fact that a has to be big enough such that the TM_{01} mode can propagate in the DLW. Namely, f has to remain above the cut-off frequency of the TM_{01} mode in the DLW. The value of a is then also dictated by considerations on beam dynamics (the beam charge has to be transmitted through the DLW and the effects of the off-axis electromagnetic fields must not significantly affect the beam quality), on the required THz power (which for a given desired peak field E_{ml} scales as a^2) and on the coupling efficiency of the THz pulse into the DLW (which decreases when a decreases).

Then, for a given frequency f and a given dielectric material with the relative dielectric permittivity ε_r, the thickness $b - a$ of the dielectric material is solely a function of the desired v_{ph}, which is fixed by beam dynamics consideration (limitation of the phase slippage between the electron bunch and the accelerating field). The required value of b is determined by solving the dispersion relation, arising from the boundary conditions in the DLW, which for the TM_{01} mode is given by Eq. (4) (see for example Ref. 11). In Eq. (4) the only unknown is b, appearing in the term $F_{00}'(k_2 a)/F_{00}(k_2 a)$, all the other parameters being fixed as previously described:

$$\frac{\varepsilon_0 J_0'(k_1 a)}{k_1 a J_0(k_1 a)} - \frac{\varepsilon_0 \varepsilon_r F_{00}'(k_2 a)}{k_2 a F_{00}(k_2 a)} = 0. \qquad (4)$$

The dispersion curve $\omega(k_z)$ (where $\omega = 2\pi f$) of the TM_{01} mode around the desired frequency f can also be computed from Eq. (4). For b being fixed to the previously determined value, this is numerically done by solving Eq. (4) for k_z (≡ v_{ph}) for several frequencies surrounding the desired central frequency f of the THz pulse. The group velocity v_g of the THz pulse in the DLW is then obtained by computing the derivative of the dispersion curve $\omega(k_z)$ of the TM_{01} mode at the central frequency f of the THz pulse. From this, the minimal duration T of the THz pulse driving the DLW required for an acceleration length (≡ THz linac length) L can be computed. It is simply equal to the difference of travel time between the electron bunch and the THz pulse over the length L. Assuming relativistic electrons for which the velocity remains always very close to c, which is the case in this paper, it can be approximated by:

$$T = \frac{L(c - v_g)}{c v_g}. \qquad (5)$$

The last important formula is the one to compute the required THz power in the DLW to obtain the desired peak field E_{ml}. This can be derived using the complex Poynting vector $\vec{S}$:

$$\vec{S} = \frac{1}{2}\vec{E} \times \vec{H}^*,$$

with $\vec{E}$ being the electric field and $\vec{H}^*$ the complex conjugate of the magnetic induction $\vec{H}$. The average power over one period, which is in our case equal to the average power, flowing through a surface is given by the real part of the integral of $\vec{S}$ over this surface. For the TM_{01} mode and in our case where k_2 is real, one has $S_\theta = 0$, S_r purely imaginary and S_z purely real. The average power in the DLW $< P >_{THz}$ is therefore given by the integral of S_z ($= E_r H_\theta^*$) over a transverse cross-section of the DLW perpendicular to its revolution axis (including both vacuum and dielectric parts). Considering that the TM_{01} mode is cylindrically symmetric, one finally obtains:

$$< P >_{THz} = \pi \int_{r=0}^{r=b} E_r H_\theta^* r dr. \qquad (6)$$

The minimal energy to be contained in the THz pulse driving the TM_{01} mode in the DLW to reach both the required peak accelerating field E_{ml} and acceleration length L is trivially given by:

$$E_{THz} = < P >_{THz} T. \qquad (7)$$

Note that E_{THz} is the energy of the THz pulse required inside the DLW and therefore does not include the losses due to the fact that the coupling efficiency into the DLW is lower than 100%. The THz energy required for the concept is therefore effectively higher than E_{THz}.

3. Optimization schemes of the compact ultrafast X-ray pulse source concept

The bunch properties at the ICS point presented in Ref. 1 lead us to the conclusion that several aspects have to be deeply studied in order to optimize the concept of compact ultrafast X-ray pulse source shown in Fig. 2. Especially, the bunch transverse emittance and energy spread obtained in Ref. 1 were still rather high for an X-ray source based on ICS. In this section, we detail several schemes we use to improve the bunch properties at the ICS point in ASTRA simulations[12] and optimize our X-ray pulse source concept.

In the rest of the paper, the following notations will be used:

- Z will be the longitudinal position along the beamline (zero corresponding to the photocathode).
- Parameters related to the S-band gun section: E_{mg} (S-band gun peak field), B_0 (solenoid peak field), $\sigma_{r,UV}$ and $\sigma_{t,UV}$ (rms transverse size and length of the UV laser pulse driving the S-band gun).
- Parameters related to the THz linac section: Z_l (distance between the photocathode and the THz linac entrance), E_{ml} (THz linac peak field), f and v_{ph} (central frequency and phase velocity of the THz pulse driving the THz linac).
- G_{Q1}, G_{Q2} and G_{Q3} will denote the gradients of the three quadrupoles used for the final transverse focusing (a positive gradient is chosen as being a quadrupole focusing in the horizontal plane and defocusing in the vertical plane).
- Electron bunch properties: Q (charge), $<E>$ (mean kinetic energy), σ_E (rms energy spread), σ_t (σ_z) (rms duration/length), σ_x and σ_y (horizontal and vertical rms sizes) and ε_x and ε_y (horizontal and vertical rms normalized emittances).

3.1. Space-charge induced reduction of the correlated energy spread induced in the THz linac

One of the key features of the ICS process is that all the electrons constituting the bunch contribute equally to the emitted radiation, while for a free electron laser (FEL) only a slice of the electron bunch is involved. The consequence is that the projected values of ε_x, ε_y and σ_E have to be minimized to maximize the quality of the emitted radiation, and not just only the slice values of these quantities. This is a challenging objective for the hybrid concept presented in this paper. First, as explained in Ref. 1, ε_x and ε_y are limited by the fact that $\sigma_{r,UV}$ has to be set to a rather large value to minimize the bunch length at the THz linac entrance, implying a proportionally large value of the thermal emittance at the cathode[13]. Second, the electron bunch has to be injected off-crest in the THz linac in order to produce the correct chirp to compress it by velocity bunching[14]. Due to the high-frequencies simulated in the THz linac ($f \geq 150$ GHz), it results in a large increase of the correlated energy spread of the bunch $\sigma_{E,corr}$.

3.1.1. Introduction to the phenomenon

Fortunately, the correlated energy spread induced by the compression in the THz linac and the transverse emittances can be reduced significantly during the final transverse focusing of the electron bunch by the quadrupole, but ε_x and ε_y still remain ultimately limited by the thermal emittance. These effects are illustrated in Fig. 3, where the evolutions of σ_x, σ_y, σ_t, ε_x, ε_y and σ_E from the THz linac exit up to the ICS point are displayed for a typical example case and compared with the quadrupole triplet for the final transverse focusing switched off and on.

Fig. 3 (right plots) clearly shows that the final focusing helps to significantly reduce σ_E. This decrease of σ_E is generated by the space-charge forces, which are the forces generated on any electron of the bunch by the bunch electromagnetic field. Indeed, at the THz linac exit the electron bunch exhibits a negative chirp of its longitudinal phase-space, namely with the fastest electrons in the tail and the slowest in the head, implying a ballistic compression (left plots). During this compression phase the space-charge forces, which imply a gain of energy for the electrons in the head and a loss of energy for those in the tail, naturally reduce the energy spread. This reduction is already visible without final transverse focusing by the quadrupole triplet (top right plot), but is strongly amplified by the final transverse focusing (bottom right plot) because the electron bunch becomes much denser and therefore the space-charge forces much stronger. Note that this reduction of σ_E reduces the velocity differences between the electrons of the bunch and therefore weakens the strength of the compression. This effect is visible by comparing the top left and bottom left plots of Fig. 3. However, since the chirp induced by the THz linac is very strong and the decrease of σ_E mainly happens very close from the ICS point, this effect remains limited (σ_t at the ICS point increases from 0.9 fs to 1.2 fs in the example case of Fig. 3 when the quadrupole triplet is switched on). More explanations on how the trade-off between σ_E and σ_t is defined are given in Secs. 3.1.2 and 3.1.3.

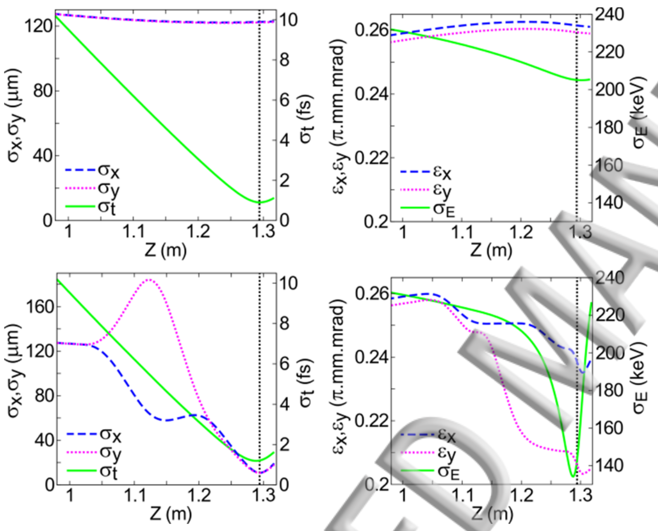

Fig. 3. Evolution of σ_x, σ_y and σ_t (left plots) and of ε_x, ε_y and σ_E (right plots) from the THz linac exit up to the ICS point. Quadrupole triplet for final transverse focusing switched off (top plots) and on (bottom plots). Conditions: Q = 1 pC; E_{mg} = 140 MV/m; E_{ml} = 115 MV/m; f = 300 GHz; v_{ph} = c; L = 12.8 cm; B_0 = 0.258 T; $\sigma_{r,UV}$ = 0.5 mm; $\sigma_{t,UV}$ = 75 fs; Z_l = 85 cm; G_{Q1} = +9 T/m; G_{Q2} = -19.5 T/m; G_{Q3} = +20.5 T/m; Final mean kinetic energy: 17.7 MeV. By appropriate settings of the gradients and position of the triplet, the position of the transverse focal point (bottom left) has been adjusted to be the same than the position of the longitudinal focal point when the quadrupole triplet is switched off (top left). The vertical line at Z = 1.295 m marks this position which is the one of the ICS point.

Fig. 3 (right plots) also shows that the final transverse focusing causes a reduction of the transverse emittances, but that it is not symmetric between ε_x and ε_y. It is indeed stronger in the plane where the bunch is defocused by the first quadrupole and then undergoes a strong focusing (bottom right plot), which is the y plane in our example.

The effect of the final transverse focusing on ε_x and ε_y remains almost unchanged if the conditions other than the gradients of the quadrupoles are changed. This is not the case for σ_E and σ_t which are especially sensitive to two conditions: the position of the ICS point (≡ of the electron bunch transverse focal point) and the electron bunch transverse size at the THz linac exit (≡ at the entrance of the quadrupole triplet).

3.1.2. Influence of the position of the ICS point

To quantify a change of the position of the ICS point along the beamline, noted Z_{ICS} thereafter, a reference independent on the quadrupole triplet settings is required. We choose to use for this purpose the position of the longitudinal focal point along the beamline when the quadrupole triplet is switched off, noted Z_{long} thereafter. A change of the position of the ICS point is then quantified by the parameter ΔZ_{lt} = $Z_{ICS} - Z_{long}$.

Practically, we studied the influence of the position of the ICS point on the achieved bunch properties by changing the position of the quadrupole triplet compared to the case shown in Fig. 3, for which Z_{long} = 1.295 m, which results in a change of Z_{ICS} and thus ΔZ_{lt}. Namely, a global longitudinal translation of the quadrupole triplet has been applied and G_{Q3} has been in some cases slightly modified (at maximum by 0.15 T/m compared to the case of Fig. 3) to keep the minima of σ_x and σ_y at the same Z position along the beamline (Z_{ICS}). Fig. 4 displays the impact of the position of the ICS point, quantified by ΔZ_{lt}, on the bunch properties at the ICS point. ΔZ_{lt} = -24 mm corresponds in this example to the case where the field of the first quadrupole starts right at the THz linac exit, which is the lowest possible value of ΔZ_{lt}. Fig. 5 displays the evolution of σ_E and σ_t from the THz linac exit up to the ICS point and around the ICS point for three cases extracted from Fig. 4: ΔZ_{lt} = -24 mm, -10 mm and +10 mm.

Fig. 4 (top) shows that σ_E and σ_t at the ICS point evolve differently with ΔZ_{lt}, namely σ_t exhibits a minimum around ΔZ_{lt} = +10 mm while σ_E decreases with ΔZ_{lt} and is still not minimized for the lowest possible value of -24 mm. A trade-off has therefore to be made between σ_E and σ_t at the ICS point. Fig. 5 (left plots) illustrates the reason explaining these different behaviors. Namely, an increase of ΔZ_{lt} implies that the final transverse focusing with the quadrupole triplet, and therefore the decrease of σ_E shown in Fig. 3 (right), will start farther from the THz linac exit, that is to say at a point where the bunch compression is more advanced and a larger part of the correlated σ_E has already been transferred to uncorrelated σ_E (which cannot be removed by space-charge forces). As a result, the reduction of σ_E by the space-charge forces becomes less efficient (see Fig. 5 top left). On the other hand, the less efficient reduction of σ_E with the increase of ΔZ_{lt} implies that the bunch compression is less affected and is therefore more efficient (see Fig. 5 bottom left). However, if ΔZ_{lt} becomes too high σ_t will start to increase again simply because the ICS point (≡ transverse focal point) is located too far after the position of the longitudinal focal point when the quadrupole triplet is switched off. Note that in principle, there is a value of ΔZ_{lt} below which σ_E at the ICS point should start to increase again because σ_t in the final focusing region would become too big, implying that the bunch density and therefore the space-charge forces decrease too much and reduce the efficiency of the reduction of σ_E. This value of ΔZ_{lt} is however not achievable for the example presented in this section.

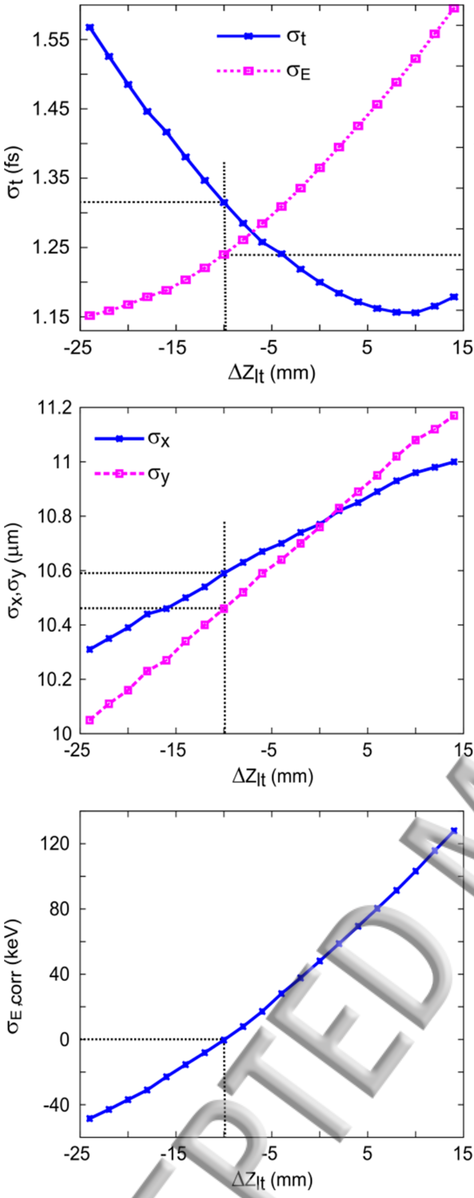

Fig. 4. σ_E and σ_t at the ICS point as a function of ΔZ_{lt} (top), σ_x and σ_y at the ICS point as a function of ΔZ_{lt} (middle), $\sigma_{E,corr}$ at the ICS point as a function of ΔZ_{lt} (bottom). The black lines mark the point where $\sigma_{E,corr}$ at the ICS point is null. Conditions: see caption of Fig. 3.

Fig. 4 (middle) shows that the choice of the position of the ICS point has a limited impact on the transverse aspect of the bunch at the ICS point, since the bunch always remains almost transversely symmetric and the variation of $\sigma_{x,y}$ are within 10%. We will therefore not use $\sigma_{x,y}$ as a primary criterion to fix the position of the ICS point. We choose to fix ΔZ_{lt} at the value where $\sigma_{E,corr}$ at the ICS point is zero which is around -10 mm in this example case (see Fig. 4 bottom plot). As visible in Fig. 4 (top) this point is a good trade-off between σ_E and σ_t, and Fig. 4 (middle) also indicates that σ_x and σ_y are close to each other (almost transversely symmetric bunch) and not significantly bigger than at ΔZ_{lt} = -24 mm. Furthermore, Fig. 5 (right plots) shows that this value of ΔZ_{lt} allows obtaining first order derivatives of σ_E and σ_t with respect to Z which are close to zero at the ICS point. This implies that σ_E and σ_t exhibit small variations in the Z interval where the electron bunch interacts with the laser around the ICS point[b], which is a desired property. Note that the variations would be higher for a different choice of ΔZ_{lt} (see Fig. 5 right plots).

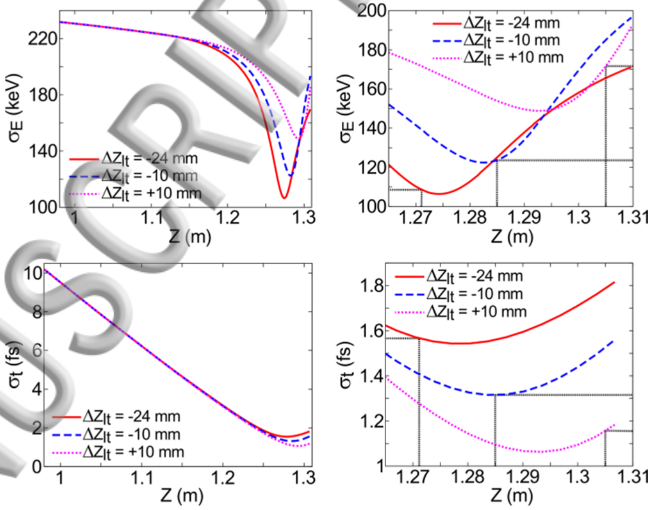

Fig. 5. Evolution of σ_E (top left) and σ_t (bottom left) from the THz linac exit to the ICS point for three cases extracted from Fig. 3: ΔZ_{lt} = -24 mm, -10 mm and +10 mm. The plots on the right are zooms around the ICS point. The black lines mark the position of the ICS point (≡ transverse focal point). Conditions: see caption of Fig. 3.

3.1.3. Influence of the bunch transverse size at the THz linac exit

Fig. 6 displays the impact of the bunch transverse size at the THz linac exit on the bunch properties at the ICS point for ΔZ_{lt} fixed to -10 mm (see Fig. 5). The transverse bunch size at the THz linac exit has been artificially varied in ASTRA and does not come from a change in the simulation conditions.

Fig. 6 (top) shows that σ_E and σ_t at the ICS point evolve differently as a function of the bunch transverse size at the THz linac exit, namely σ_t exhibits a minimum (around 155 µm in this case) while σ_E decreases with this size. A trade-off has therefore once again to be made between σ_E and σ_t at the ICS point. The reason for the decrease of σ_E at the ICS point is simply that when the transverse bunch size at the THz linac exit is reduced, the bunch density and therefore the space-charge forces increases, making the reduction of σ_E presented in Fig. 3 (right) more efficient. This more efficient reduction of σ_E intrinsically comes with an increase of σ_t at the ICS point (see Fig. 6 top). Fig. 6 (top) also shows that if the transverse size at the THz linac exit is too large, σ_t at the ICS

---

[b] In the case of a head-on collision, the interaction distance with the laser Z_{int} is estimated to two times the duration T_l of the laser pulse (multiplied by c) if this value is shorter than two Rayleigh lengths, otherwise it is estimated to two Rayleigh lengths: $Z_{int} = 2cT_l$ or $Z_{int} = 8\pi\sigma_l^2/\lambda_l$.

point will start to increase again. This is due to a simple geometrical effect, namely that the larger the beam the more difference in the path length, and therefore travel time, of the transversely innermost and outermost electrons of the bunch in the focusing region up to the ICS point. This effect leads to an increase of σ_t which is more than linear with the transverse bunch size at the THz linac exit. If the transverse bunch size at the THz linac exit becomes too large, this geometrical increase of σ_t overcomes the gain due to the decrease of space-charge forces and σ_t at the ICS point starts to increase again.

Finally, Fig. 6 (bottom) illustrates an additional reason not to use too small transverse bunch size at the THz linac exit. Namely, σ_x and σ_y increase which reduces the number of X-ray photons generated via ICS. Furthermore, σ_x and σ_y significantly differ from each other meaning that the bunch has a strong transverse asymmetry at the ICS point. This makes the transverse matching with the laser driving the ICS more difficult and is therefore not desired. For the example presented in this section a good trade-off between σ_E, σ_t, σ_x and σ_y is to have a transverse bunch size between 110 and 130 µm at the THz linac exit. Note that the optimal value of this transverse size depends strongly on the case considered and is also a function of the first derivative of $\sigma_{x,y}$ respective to Z at the THz linac exit and typically increases if this derivative decreases.

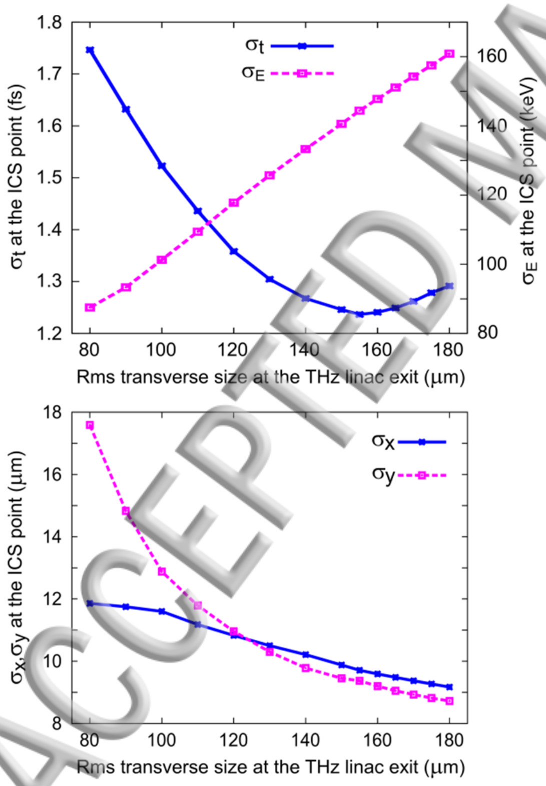

Fig. 6. σ_E and σ_t at the ICS point as a function of the bunch transverse size at the THz linac exit (top). σ_x and σ_y at the ICS point as a function of the bunch transverse size at the THz linac exit (bottom). ΔZ_{lt} is fixed to -10 mm (see Fig. 5). Conditions: see caption of Fig. 3. Note: the transverse bunch size at the THz linac exit has been varied artificially in ASTRA and does not come from a change in the simulation conditions.

3.2. Transverse shaping of the UV laser pulse driving the S-band RF-gun

In Ref. 1, we used in our simulations a 3D Gaussian laser pulse to drive the S-band RF-gun, which is not optimal for our concept. The laser pulse rms length $\sigma_{t,UV}$ we use in our simulations is 75 fs, which is too short to perform any longitudinal shaping. We therefore fixed it to be purely Gaussian and restrain ourselves to study the influence of a transverse shaping of the laser driving the RF-gun on the achievable bunch properties.

We compared four different transverse profiles for the UV laser driving the S-band RF-gun, having all the same rms transverse size $\sigma_{r,UV}$ = 0.5 mm. They are shown in Fig. 7 and their projections along a radial direction are depicted in Fig. 8. The first one is the Gaussian transverse profile, which is simple to generate experimentally but is known to lead to highly non-linear space-charge forces. The second one is the radial transverse profile, which is a transversely uniformly filled cylinder, for which the projection is a half-ellipse and the non-linear effects of the space-charge forces are limited to the transverse edges of the electron bunch. The third one is a transversely uniformly filled ellipsoid, for which the projection is an inverted parabola and the space-charge forces are purely linear. The last one is a Gaussian cut at 1σ and has been studied based on the fact that the second order Taylor expansion of a Gaussian is an inverted parabola. This profile is therefore close to the uniform ellipsoid, as visible in Fig. 8, and shows deviation to it, and therefore non-linear effects of the space-charge forces, mainly in the transverse edges of the electron bunch.

We simulated the electron bunch properties obtained at the ICS point with this four transverse profiles in almost identical conditions on a typical reference case. G_{Q3} has been slightly modified between the cases in order to keep the minima of σ_x and σ_y coincident at the ICS point. The position of the first quadrupole respective to the linac exit has also been modified in order to ensure that the contribution of the space-charge induced reduction of the correlated energy spread (see Sec. 3.1) remains the same for the four cases, which means having the same ratio between $\sigma_{E,corr}$ and σ_E. The results of this comparison are gathered in Table 1.

Table 1 shows that the radial, ellipsoid and Gaussian cut at 1σ transverse profiles all lead to a significant improvement of all the electron bunch properties (including σ_E and σ_t) compared to the purely Gaussian transverse profile. Between these three profiles only marginal differences appear in the bunch properties. We therefore choose to use in the following the Gaussian cut at 1σ transverse profile for three reasons. First, it is technically feasible since in our simulations we use only rather large values of $\sigma_{r,UV}$ (≥ 0.3 mm) to establish the various potential working points. Second, it is technically much simpler to generate than the uniformly filled ellipsoid. Finally, it will require less energy in the UV laser pulse than the radial profile, which is often generated by cutting a Gaussian profile much tighter than 1σ. Other less destructive techniques, like the use of diffractive optical elements (see for example Ref. 15), are currently used to generate a radial profile while more preserving the initial laser pulse energy. But they are also technically more complicated to implement than a cut at 1σ of a Gaussian transverse profile.

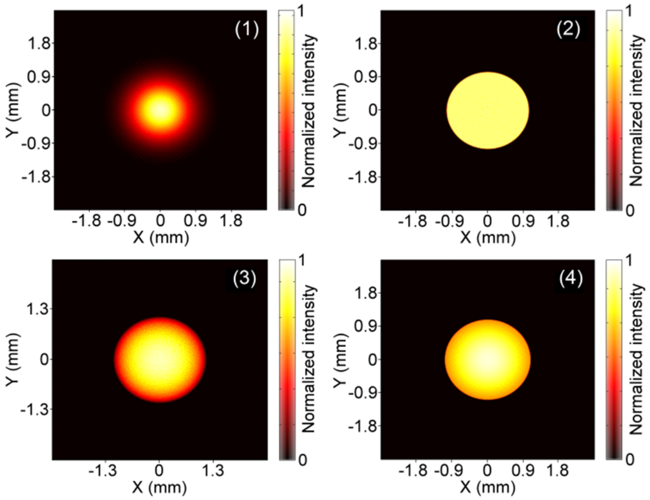

Fig. 7. The four transverse profiles compared for the UV laser pulse driving the S-band RF-gun. (1): Gaussian; (2): radial; (3): uniformly filled ellipsoid; (4): Gaussian cut at 1σ. All profiles have the same rms transverse size $\sigma_{r,UV}$ = 0.5 mm. Note that (4) is therefore not a cut of (1).

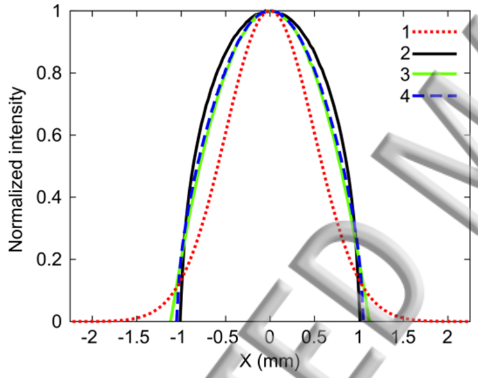

Fig. 8. Projections on a radial direction of the four transverse profiles depicted in Fig. 7. (1): Gaussian; (2): radial; (3): uniformly filled ellipsoid; (4): Gaussian cut at 1σ. All profiles have the same rms transverse size $\sigma_{r,UV}$ = 0.5 mm. Note that (4) is therefore not a cut of (1).

This significant improvement of the bunch properties with an appropriate choice of the initial transverse profile can be explained by comparing the evolution along the beamline of the electron bunch properties for the Gaussian and Gaussian cut at 1σ transverse profiles of the UV laser driving the gun.

Concerning the transverse properties, Fig. 9 shows that the transverse emittance improvement is located between the photocathode and the THz linac entrance, the relative difference remaining almost constant thereafter. This improvement is explained by the linearization of the space-charge forces induced by the Gaussian cut at 1σ profile compared to the Gaussian one. This leads to an almost constant transverse emittance before the THz linac, while it is almost doubled for the Gaussian transverse profile.

Table 1. Bunch properties simulated at the ICS point with the four transverse profiles at the cathode introduced in Figs. 7 and 8. Conditions: Q = 1 pC; E_{mg} = 140 MV/m; E_{ml} = 115 MV/m; f = 300 GHz; $v_{ph} = c$; L = 12.8 cm; B_0 = 0.258 T; $\sigma_{r,UV}$ = 0.5 mm; $\sigma_{t,UV}$ = 75 fs; Z_l = 85 cm; G_{Q1} = +9 T/m; G_{Q2} = -20.2 T/m; G_{Q3} = 24.5 T/m (Gaussian), 24.2 T/m (ellipsoid), 24.1 T/m (radial) and 24.3 T/m (Gaussian cut at 1σ).

Profile	*Gaussian*	*Radial*	*Ellipsoid*	*Gaussian cut at 1σ*
$<E>$ (MeV)	17.7	17.7	17.7	17.7
σ_E (keV)	212.8	113.5	118.4	118.2
σ_t (fs)	1.6	1.4	1.5	1.4
σ_x/σ_y (µm)	12.7/15.9	8.8/10.5	8.5/10.1	8.4/10.2
$\varepsilon_x/\varepsilon_y$ (π.mm.mrad)	0.396/ 0.329	0.236/ 0.205	0.228/ 0.195	0.226/ 0.196

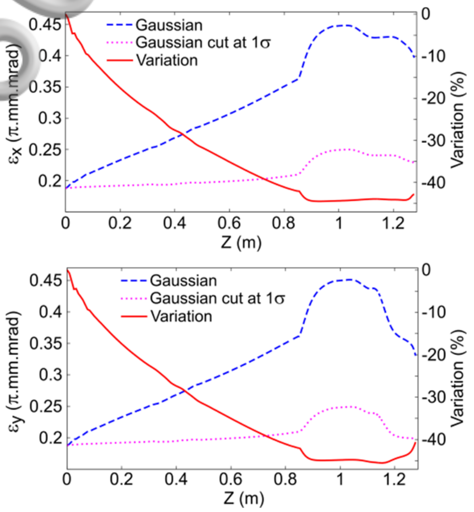

Fig. 9. Evolution of ε_x (top) and ε_y (bottom) from the cathode to the ICS point for the cases presented in Table 1 with Gaussian and Gaussian cut at 1σ transverse profiles for the UV laser driving the gun. Variation refers to the relative difference between the value for the Gaussian profile cut at 1σ and the value for the Gaussian profile. Conditions: see caption of Table 1.

Fig. 10 shows that the transverse size improvement happens at the end of the final focusing by the quadrupole triplet. It is a direct consequence of the reduction of the transverse emittance, which naturally allows for a tighter transverse focusing of the electron bunch.

For the longitudinal properties, Fig. 11 shows that the reduction of σ_t mainly happens in the gun and especially close from the photocathode, namely in the first two centimeters that is to say the first half-cell of the gun. This decrease is explained by the fact that the travel time of an electron in the gun quadratically depends on, and actually quadratically increases with, its transverse offset. This is due to the facts that the longitudinal electric field, and therefore the energy gain, decreases with the transverse offset and also that the path length becomes longer because of the force imprinted by the RF magnetic field in the gun. The Gaussian cut at 1σ

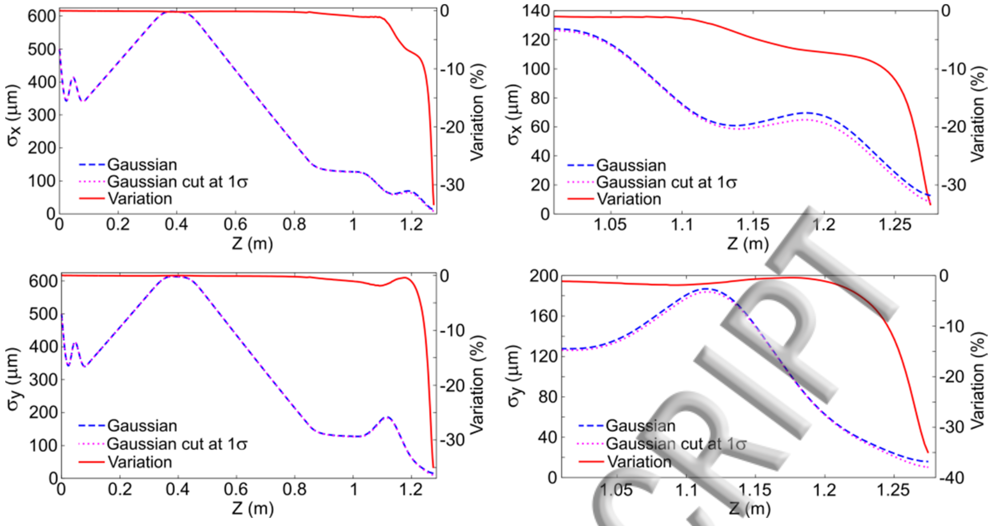

Fig. 10. Evolution of σ_x (top left) and σ_y (bottom left) from the cathode to the ICS point for the cases presented in Table 1 with Gaussian and Gaussian cut at 1σ transverse profiles for the UV laser driving the gun. Top (bottom) right: zoom on the final focusing region for σ_x (σ_y). Variation refers to the relative difference between the value for the Gaussian profile cut at 1σ and the value for the Gaussian profile. Conditions: see caption of Table 1.

transverse profile exhibits less electrons with large transverse offsets than the purely Gaussian one (see Fig. 7). As previously explained, these outer electrons exhibit much larger travel times than the inner ones. This results in a smaller spread of the travel times of the electrons in the gun and therefore a shorter bunch length. After the gun, the variation of σ_t is slightly reduced in the drift up to the THz linac entrance and is almost constant in the region of longitudinal compression between the THz linac entrance and the ICS point.

Fig. 12 shows that the reduction of σ_E for the Gaussian cut at 1σ transverse profile compared to the Gaussian transverse profile takes place at 3 different points of the beamline: in the gun, in the THz linac (especially right after the entrance) and at the end of the final focusing by the quadrupole triplet. In the gun, this reduction comes from the fact that σ_t is shorter for the Gaussian cut at 1σ transverse profile and therefore the RF-induced energy spread is lower. At the linac entrance, σ_t is still shorter for the Gaussian cut at 1σ transverse profile (see Fig. 11). As a result, the energy spread induced by the off-crest injection in the THz linac, necessary for bunch compression, is smaller which explains that the variation of σ_E compared to the Gaussian transverse profile becomes greater in the first centimeters of the THz linac. At the end of the final focusing region, the electron bunch is shorter (see Fig. 11) and transversely tighter focused (see Fig. 10) for the Gaussian cut at 1σ transverse profile. The space-charge forces are therefore stronger, by a factor around 2.7, and the space-charge induced reduction of the correlated energy spread presented in Sec. 3.1 is much more efficient, explaining that σ_E decreases much more than for the Gaussian transverse profile at the end of the final focusing by the quadrupole triplet.

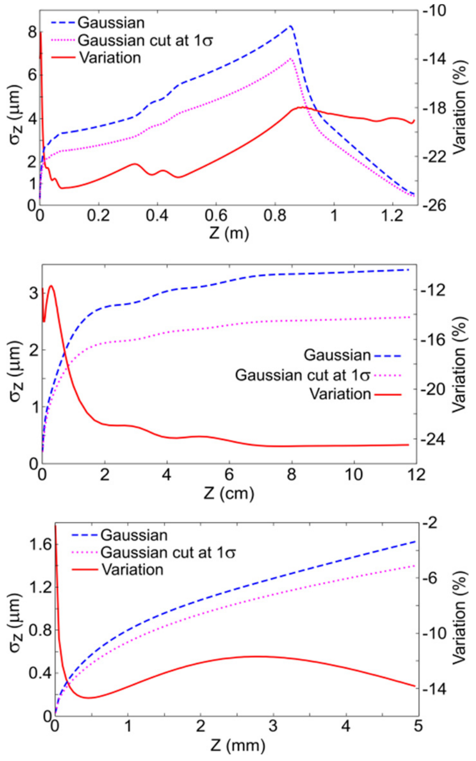

Fig. 11. Evolution of σ_z from the cathode to the ICS point (top) for the cases presented in Table 1 with Gaussian and Gaussian cut at 1σ transverse profiles for the UV laser driving the gun. Middle plot: zoom on the gun region. Bottom plot: zoom on the cathode region. Variation refers to the relative difference between the value for the Gaussian profile cut at 1σ and the value for the Gaussian profile. Conditions: see caption of Table 1.

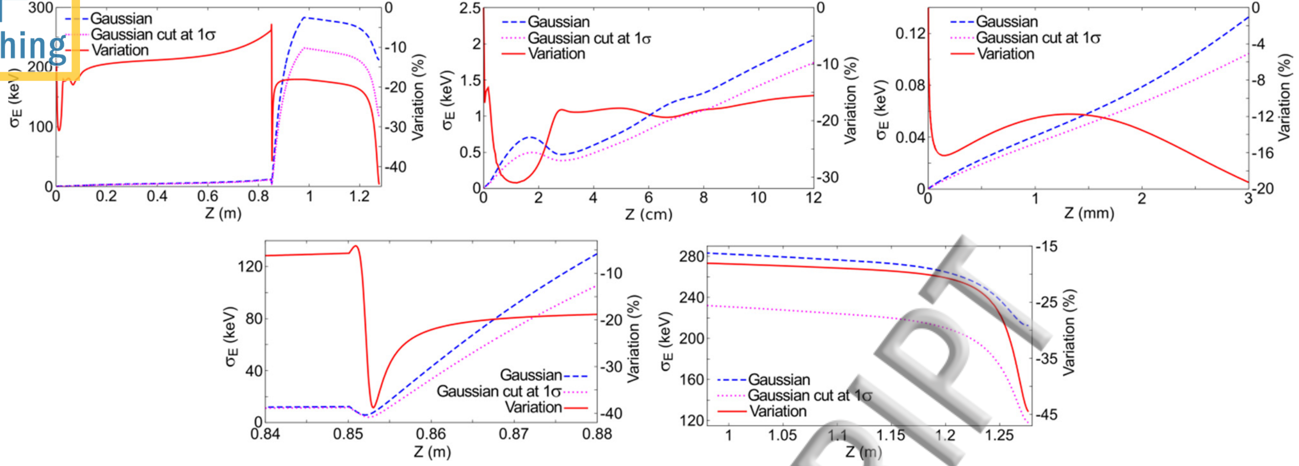

Fig. 12. Evolution of σ_E from the cathode to the ICS point (top left) for the cases presented in Table 1 with Gaussian and Gaussian cut at 1σ transverse profiles for the UV laser driving the gun. Top center: zoom on the gun region. Top right: zoom on the cathode region. Bottom left: zoom on the linac entrance region. Bottom right: zoom on the final focusing region. Variation refers to the relative difference between the value for the Gaussian profile cut at 1σ and the one for the Gaussian profile. Conditions: see caption of Table 1.

3.3. Fine-tuning of the phase velocity of the THz pulse driving the THz linac

In Ref. 1 and up to now in this paper, we considered that the phase velocity of the TM_{01} mode in the DLW is equal to c. However, it can be seen in Fig. 13 that this value is not optimal for $f < 300$ GHz. Indeed, for $f = 150$ GHz, it is visible that after the off-crest injection, necessary for bunch compression, the phase slippage is too slow and the bunch exits the THz linac still being far from the crest of the accelerating field (88.5 MV/m compared to 115 MV/m peak field). On the other hand, for $f = 300$ GHz, the phase slippage is faster and the bunch exits the THz linac close to the crest of the accelerating field (111.3 MV/m compared to 115 MV/m peak field).

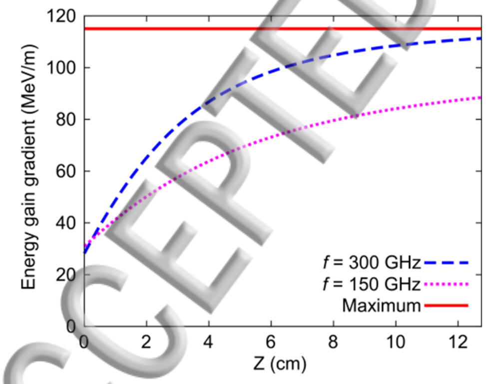

Fig. 13. Evolution of the bunch energy gain gradient along the THz linac for two different accelerating frequencies f. Conditions: Q = 1 pC; E_{mg} = 140 MV/m; E_{ml} = 115 MV/m; $v_{ph} = c$; L = 12.8 cm; B_0 = 0.258 T (f = 300 GHz) & 0.249 T (f = 150 GHz); $\sigma_{r,UV}$ = 0.5 mm; $\sigma_{t,UV}$ = 75 fs; Z_l = 85 cm.

In this sub-section, we will optimize v_{ph} for $f = 150$ GHz such that the bunch exits the THz linac very close from the crest of the accelerating field and look at the impact on the simulated bunch properties at the ICS point. We will not try to perform this optimization for $f = 300$ GHz, since the bunch already exits the linac very close from the crest of the accelerating field for $v_{ph} = c$ (see Fig. 13).

Fig. 14 shows the evolution of the bunch energy gain gradient along the THz linac for $f = 150$ GHz at $v_{ph} = c$ and $v_{ph} = 1.002c$. It clearly shows that $v_{ph} = 1.002c$, thanks to the faster phase slippage, allows the bunch exiting the linac very close to the crest of the accelerating field (113.5 MV/m compared to 115 MV/m peak field), thus optimizing the use of the accelerating field. The optimal value of v_{ph} is a function of f, E_{ml}, L and the energy of the electron bunch at the THz linac entrance. Note that the increase of v_{ph}, resulting in a faster phase slippage, requires to significantly change the injection phase into the THz linac, namely to go more off-crest as visible in Fig. 14.

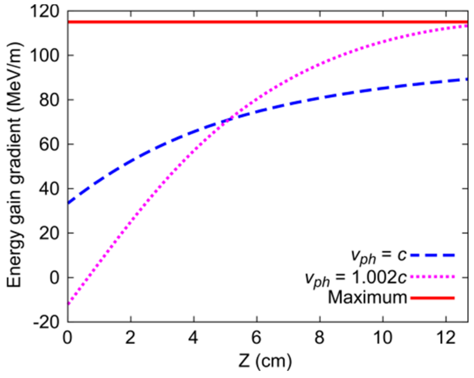

Fig. 14. Evolution of the bunch energy gain gradient along the THz linac for two different phase velocities v_{ph} of the accelerating field. Conditions: Q = 3.75 pC; E_{mg} = 140 MV/m; E_{ml} = 115 MV/m; f = 150 GHz; L = 12.8 cm; B_0 = 0.246 T ($v_{ph} = c$) & 0.238 T ($v_{ph} = 1.002c$); $\sigma_{r,UV}$ = 0.7 mm; $\sigma_{t,UV}$ = 75 fs; Z_l = 91 cm.

Table 2 presents the electron bunch properties at the ICS point for the two v_{ph} simulated in Fig. 14 in the THz linac. It is visible that σ_E is significantly affected by a change of v_{ph}, since it is decreased by a factor of 2 when increasing v_{ph} from c to $1.002c$. The other electron bunch properties are much less affected since they vary by 5% at maximum. To understand the explanation of this reduction of σ_E it is interesting to look at its evolution along the beamline for the two v_{ph} simulated in this section, which is shown in Fig. 15.

Table 2. Electron bunch properties at the ICS point for the two v_{ph} simulated in Fig. 14 in the THz linac. Conditions: see caption of Fig. 14; G_{Q1} = +7.1 T/m (v_{ph} = c) & +5.75 T/m (v_{ph} = 1.002c); G_{Q2} = -16 T/m (v_{ph} = c) & -14.25 T/m (v_{ph} = 1.002c); G_{Q3} = +16.25 T/m (v_{ph} = c) & +15.2 T/m (v_{ph} = 1.002c).

v_{ph} (c)	$<E>$ (MeV)	σ_E (keV)	σ_t (fs)	σ_x/σ_y (μm)	$\varepsilon_x/\varepsilon_y$ (π.mm.mrad)
1	15.24	200.6	3.31	11.3/11.9	0.393/0.293
1.002	15.33	100.7	3.38	10.7/11.4	0.375/0.300

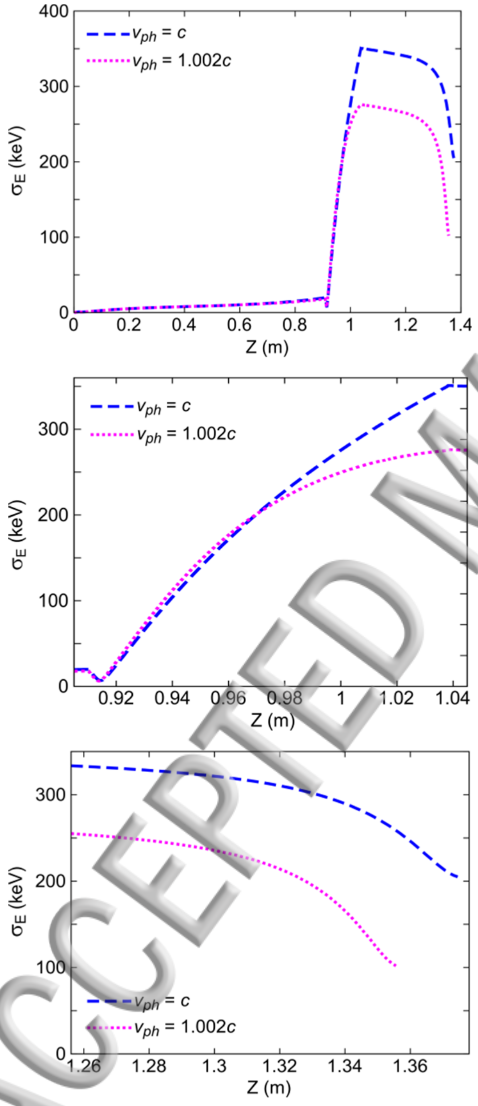

Fig. 15. Evolution of σ_E from the cathode up to the ICS point for the two v_{ph} simulated in Fig. 14 in the THz linac (top). Middle: Zoom on the THz linac region. Bottom: Zoom on the final focusing region. Conditions: see captions of Fig. 14 and Table 2.

Fig. 15 (top) shows that the difference on σ_E between the two v_{ph} happens mainly in the THz linac. Indeed, at the end of the THz linac the difference between v_{ph} = 1.002c and v_{ph} = c is around 85 keV (see Fig. 15 middle plot), which is close to the final difference of 100 keV (see Table 2). No significant difference is introduced by the space-charge induced reduction of the energy spread during the final transverse focusing (see Fig. 15 bottom). As visible in Fig. 15 (middle plot), the gain on σ_E for v_{ph} = 1.002c compared to v_{ph} = c happens in the second half of the THz linac. This is due to the fact that after around 5.5 cm in the THz linac, the bunch becomes closer to the crest of the accelerating field, where the induced energy spread is minimal, than in the case for v_{ph} = c and continues to slip faster towards the crest of the accelerating field than for v_{ph} = c (see Fig. 14). As a result, the increase rate of σ_E starts to slow down and becomes almost zero at the THz linac exit for v_{ph} = 1.002c, while it decreases only a little for v_{ph} = c (see Fig. 15 middle plot) implying a higher final value of σ_E.

We demonstrated in this sub-section that a fine-tuning of the phase velocity of the THz pulse driving the THz linac is of primary importance regarding the value of the energy spread achievable at the ICS point, since σ_E is a fast varying function of v_{ph}. According to Sec. 2, this fine-tuning of v_{ph} translates into a fine-tuning of the dielectric thickness $b - a$ in the DLW. This means that the margins for production errors of the DLW are very tight and that it must be produced with a high mechanical precision. As an example, in the vicinity of v_{ph} = c, the change of v_{ph} reaches 1% if the error of $b - a$ is 1.45 μm at f = 300 GHz and 2.91 μm at f = 150 GHz. In particular, this means that the two cases presented in this sub-section (v_{ph} = c and v_{ph} = 1.002c at f = 150 GHz) differ only by around 600 nm in the value of $b - a$ required for the DLW.

Fortunately, v_{ph} is also dependent on f. As a result, a production error for the value of $b - a$ could be compensated by adjusting the frequency of the THz pulse driving the linac as it has been reported in Refs. 16 and 17. Furthermore, thanks to their small dimensions (width in the millimeter range and length in the range of ten cm), the DLW are fast to be produced and much easier to be replaced in a beamline than a conventional RF accelerating structure. This allows the possibility to quickly exchange a DLW in case of a production error which cannot be overcome by an adjustment of the THz pulse frequency. Finally, the small dimensions of a DLW could also be used to place several DLW with different properties (f, L, v_{ph}, etc.) in the beamline with the possibility to switch between them. This will enable achieving different electron bunch properties ($<E>$ in particular) which could then be used for different applications (different X-ray energies for the case of the ICS source developed in this paper).

4. Simulated properties of the X-ray pulse generated via ICS

Following the steps and optimization schemes introduced in Ref. 1 and in Sec. 3 of this paper, we simulated several potential working points using the ASTRA code[12] for the beam dynamics up to the ICS point. More details on how the THz linac is modeled into ASTRA can be found in Ref. 18. The distribution obtained with ASTRA is then exported into the CAIN Monte-Carlo code[19], which is then used to simulate the interaction of the electron bunch with the laser, leading to the generation of the X-ray pulse via ICS.

4.1. Electron bunch properties simulated at the ICS point

We simulated the beam dynamics up to the ICS point for bunch charges varying from Q = 100 fC to Q = 5 pC and for two frequencies of the THz pulse driving the THz linac, namely f = 300 GHz and f = 150 GHz. The relevant electron bunch properties at the ICS point are gathered in Table 3 (f = 300 GHz) and Table 4 (f = 150 GHz).

Table 3. Electron bunch properties at the ICS point for the selected potential working points of the hybrid concept of ultrafast X-ray pulse source. Conditions: E_{mg} = 140 MV/m; E_{ml} = 115 MV/m; f = 300 GHz; v_{ph} = c; L = 12.8 cm; $\sigma_{t,UV}$ = 75 fs.

Q (pC)	$<E>$ (MeV)	σ_E (keV)	σ_t (fs)	σ_x/σ_y (µm)	$\varepsilon_x/\varepsilon_y$ (π.mm.mrad)
0.1	17.7	41.7	0.41	4.5/5.9	0.114/0.112
0.5	17.6	77.0	0.81	6.4/8.3	0.187/0.171
1.0	17.5	132.5	1.34	6.8/7.9	0.226/0.189
1.75	17.6	188.8	1.93	8.9/9.7	0.318/0.244
2.5	17.8	245.6	2.61	10.7/10.4	0.384/0.274
3.75	17.7	357.5	3.72	12.2/12.1	0.452/0.307
5.0	17.8	462.3	5.02	13.2/13.6	0.527/0.348

Table 4. Electron bunch properties at the ICS point for the selected potential working points of the hybrid concept of ultrafast X-ray pulse source. Conditions: E_{mg} = 140 MV/m; E_{ml} = 115 MV/m; f = 150 GHz; v_{ph} = 1.002c; L = 12.8 cm; $\sigma_{t,UV}$ = 75 fs.

Q (pC)	$<E>$ (MeV)	σ_E (keV)	σ_t (fs)	σ_x/σ_y (µm)	$\varepsilon_x/\varepsilon_y$ (π.mm.mrad)
0.1	15.6	19.9	0.65	5.8/4.5	0.113/0.112
0.5	15.0	32.3	1.23	5.7/6.7	0.177/0.170
1.0	15.0	45.1	1.81	6.0/6.2	0.206/0.191
1.75	15.0	55.1	2.18	7.4/7.7	0.272/0.238
2.5	15.1	69.1	2.49	8.5/9.4	0.317/0.267
3.75	15.0	129.6	3.12	8.7/8.6	0.376/0.287
5.0	15.1	197.0	3.81	8.6/8.4	0.430/0.340

One can observe that $<E>$ is significantly higher at f = 300 GHz than at f = 150 GHz (around 17% increase). As explained in Ref. 1 and visible in Fig. 13 in the present paper, this is due to the fact that after the off-crest injection in the THz linac, the bunch experiences a higher phase slippage at f = 300 GHz and therefore moves faster towards the crest of the accelerating field, implying a higher energy gain.

The behaviors of the electron bunch longitudinal properties (σ_E and σ_t) are the same for both f = 300 GHz and f = 150 GHz, namely they increase with Q. The increase of σ_E and σ_t with Q are correlated together and explained by the increase of the space-charge forces. First, the increase of Q leads to a higher σ_t at the THz linac entrance which, due to the off-crest injection, implies a higher σ_E at the ICS point. Then, the higher σ_t at the THz linac entrance results in the generation of stronger non-linearities in the bunch longitudinal phase-space during its compression in the THz linac, which limit the achievable σ_t at the ICS point. Besides, the increase with Q of the space-charge forces close to the ICS point also limits the achievable σ_t.

Not only the statistical bunch properties, as shown in Tables 3 and 4, are of interest. The transverse profile of the electron bunch and its longitudinal phase-space at the ICS point also have to be investigated. They are shown in Fig. 16 for one representative case, the case with Q = 1 pC in Table 3.

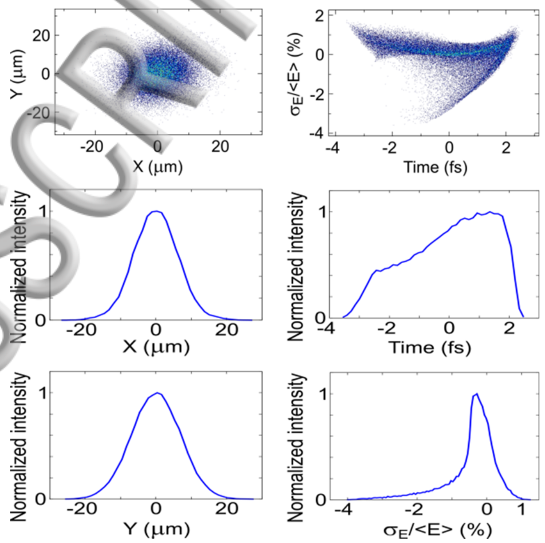

Fig. 16. Transverse profile and projections (left plots) and longitudinal phase-space and projections (right plots) of the electron bunch at the ICS point for the case with Q = 1 pC in Table 3.

Fig. 16 shows that the electron bunch transverse profile is close from being Gaussian. This is a desired property, since the best overlap possible with the transverse profile of the laser pulse driving the ICS, which will typically be Gaussian, has to be achieved. It is also visible in Fig. 16 that the time profile of the electron bunch exhibits no spikes and that all the electrons are contained in a few fs and not only a fraction of them. Finally, Fig. 16 highlights that a significant part of the bunch energy spread is due to a long tail of low energy electrons, meaning that the bunch core has a much lower σ_E than what is shown in Tables 3 and 4.

One last important point is that the working points presented in Tables 3 and 4 are not fixed but offer a certain amount of tunability concerning σ_E, σ_t and $\sigma_{x,y}$ by modifying the parameters of the quadrupole triplet and the phase of the THz linac used for the final focusing of the bunch, respectively in the transverse and longitudinal planes. This tunability is illustrated by Table 5.

However, the tunability illustrated by Table 5 is not independent for σ_E, σ_t and $\sigma_{x,y}$. Typically, the strength of the final focusing can be varied in order to put the ICS point closer (stronger focusing) or farther (weaker focusing) from the THz linac exit. A stronger focusing will result in smaller values of $\sigma_{x,y}$ and σ_t, but in a larger value of σ_E since the mechanism used to reduce σ_E (see Sec. 3.1) becomes less efficient because the distance between the linac exit and the ICS point, therefore the integrated effect of the space-charge forces along this path, decreases. On the other hand, a weaker focusing will result on a smaller value of σ_E, but larger values of $\sigma_{x,y}$ and σ_t. A trade-off has therefore to be found on the strength of the final focusing of the bunch. This is illustrated by Table 5, where the strength of the final focusing has been varied for the case at Q = 1 pC presented in Table 4, going from the stronger to the weaker focusing if one reads the rows from top to bottom. The injection phase φ_0 in the THz linac implies a change in the strength of the bunch compression (≡ longitudinal focusing), a lower φ_0 meaning a stronger longitudinal focusing. The quadrupole gradients G_{Q1}, G_{Q2} and G_{Q3} imply a change in the strength of the transverse focusing. In addition to the aforementioned evolution of σ_E, σ_t and $\sigma_{x,y}$ with the strength of the final focusing, one can note that $<E>$ slightly increases when this strength decreases. This is simply explained by the fact that the bunch is injected closer to the crest of the accelerating field when φ_0 increases. One can also note that ε_x and ε_y remain almost unchanged for the different strengths of the final focusing tested in Table 5.

Table 5. Electron bunch properties at the ICS point for different strengths of the final focusing of the bunch (this strength decreases from the top to the bottom row). Conditions: E_{mg} = 140 MV/m; $\sigma_{r,UV}$ = 0.5 mm; $\sigma_{t,UV}$ = 75 fs; Q = 1 pC; B_0 = 0.24 T; Z_l = 85.1 cm; E_{ml} = 115 MV/m; f = 150 GHz; L = 12.8 cm; v_{ph} = 1.002c. Note that the ICS point is not at the same Z for each case. The underlined case is the same as for Q = 1 pC in Table 4.

φ_0 (°)	G_{Q1} /G_{Q2} (T/m) /G_{Q3}	$<E>$ (MeV)	σ_E (keV)	σ_t (fs)	σ_x /σ_y (µm)	ε_x /ε_y (π.mm.mrad)
-1.3	+7.25 /-17.58 /+27.65	14.83	56.7	1.79	5.3 /5.6	0.205 /0.193
0	+6.75 /-16.25 /+20.85	15.00	45.1	1.81	6.0 /6.2	0.206 /0.191
+1.3	+6.25 /-14.93 /+16.2	15.15	36.3	1.93	6.9 /7.2	0.206 /191
+2.6	+5.75 /-13.6 +12.8	15.31	32.7	1.98	8.3 /8.5	0.206 /0.194
+3.9	+5.4 /-12.9 /+11.6	15.47	30.5	2.20	8.8 /9.2	0.206 /0.195

4.2. Simulated properties of the X-ray pulse generated via ICS

We simulated the generation of the X-ray pulse via the ICS process[20] occurring during the interaction of the electron bunch simulated in Sec. 4.1 for various potential working points (see Tables 3 and 4) with a laser with the Monte-Carlo code CAIN, which is already validated against experimental measurements[21] and used to validate analytical model[22]. We also compared the simulation results with the prediction of the analytical model generally used to describe the photon generation by Compton Scattering.

In this analytical model, the energy of the photons scattered by interaction with the electron bunch, in the case where the recoil of the involved electron is negligible, is given by:

$$h\nu_\gamma = h\nu_L \frac{2\gamma^2(1-\cos(\alpha))}{1+\gamma^2\theta^2+a_0^2/2}; a_0 = 4.3\frac{c}{\nu_L w_0}\sqrt{\frac{U_L[J]}{\sigma_{t,L}[ps]}}, \quad (8)$$

with h being the Planck constant, ν_γ the frequency of the photons after scattering, ν_L the frequency of the laser photons, γ the relativistic factor of the electrons, α the collision angle (α = 180° denoting a head-on collision), θ the observation angle respective to the electron bunch trajectory (0° denotes a photon having the same trajectory as the electron bunch), w_0 the waist of the laser pulse at the interaction point (equal to 2 times its rms transverse size), U_L the laser pulse energy and $\sigma_{t,L}$ its rms length. Under the assumption of a transversely round electron bunch, the number of photons generated per pulse N_γ is derived using the Thomson cross-section σ_{th} = $0.67*10^{-28}$ m^2 as[23]:

$$N_\gamma = \frac{N_L N_e \sigma_{th}}{2\pi(\sigma_x^2+w_0^2/4)}, \quad (9)$$

where N_L is the number of photons in the laser pulse driving the ICS process, N_e the number of electrons in the bunch and σ_x the rms transverse size of the electron bunch at the interaction point. This quantity alone is however insufficient to characterize the generated radiation, since as visible from Eq. (8) the photon energy depends on the observation angle θ. As a consequence, the bandwidth of the entire pulse is very large and it is usually collimated to an angle θ_{coll} in order to reduce it, such that it becomes only dominated by the electron bunch and the laser properties. The relevant quantities are therefore the number of photons into θ_{coll} given by[23,24]:

$$N_{\gamma,\theta_{coll}} = \frac{4.1*10^8 U_L[J]Q[pC]\gamma^2\theta_{coll}^2}{h\nu_L[eV](\sigma_x^2+w_0^2/4)[\mu m^2]}, \quad (10)$$

and the rms relative bandwidth of the generated photon pulse within θ_{coll} given by[22]:

$$\sigma_{\nu_\gamma}/\nu_\gamma = \sqrt{(\gamma\theta_{coll})^4 + \left(2\frac{\sigma_\gamma}{\gamma}\right)^2 + \left(\frac{\varepsilon_x}{\sigma_x}\right)^4 + \left(\frac{\sigma_{\nu_L}}{\nu_L}\right)^2 + \left(\frac{M^2 c}{2\pi\nu_L w_0}\right)^4 + \left(\frac{a_0^2/3}{1+a_0^2/2}\right)^2}. \quad (11)$$

The six contributions to the bandwidth of the pulse are respectively: the collimation angle, the electron bunch energy spread, the electron bunch transverse emittance, the laser bandwidth, the diffraction term and the temporal profile broadening contribution. Note that Eqs. (9), (10) and (11) are established for a head-on collision (α = 180°) and under the assumption of an optimal space-time overlap of the electron bunch and laser pulse, which is met if the three following conditions are fulfilled[23]:

$$w_0 \approx 2\sigma_x; \sigma_z < \gamma\sigma_x^2/\varepsilon_x\, ; c\sigma_{t,L} < 2\pi w_0^2 \nu_L/c. \qquad (12)$$

A large number of applications of the X-ray sources require maximizing the number of photons in the pulse while minimizing the bandwidth of this pulse. As visible from Eqs. (10) and (11) these are two conflicting objectives and a trade-off has therefore to be found between both. Starting from Eqs. (10) and (11), and giving the same importance to the number of photons and the bandwidth, Ref. 23 defines the following figure of merit for the electron bunch, which has to be maximized in order to optimize the X-ray source:

$$\hat{\rho} = \frac{Q}{\sigma_x^2\sqrt{\left(2\frac{\sigma_\gamma}{\gamma}\right)^2+\left(\frac{\varepsilon_x}{\sigma_x}\right)^4}}. \qquad (13)$$

Maximizing $\hat{\rho}$ results in maximizing the spectral density *SPD* of the X-ray source (in photons/eV) given by:

$$SPD = \frac{N_{\gamma,\theta coll}}{\sqrt{2\pi}h\Delta\nu_\gamma}.$$

We used the figure of merit given by Eq. (13) to select the working points from Tables 3 and 4 for which we simulated the ICS process with CAIN[c]. For f = 300 GHz this is the case for Q = 1 pC, and for f = 150 GHz the case for Q = 1 pC. However $\hat{\rho}$ does not include σ_t, which we also aim to minimize for the proposed concept. We therefore also simulate the ICS process for the cases with the shortest electron bunch, namely Q = 100 fC for f = 300 GHz and f = 150 GHz. Finally, we also simulated one case at higher charge for each frequency, namely Q = 2.5 pC for f = 300 GHz and Q = 5 pC for f = 150 GHz.

For the abovementioned cases, we choose to fix the collimation angle θ_{coll} to a value of 4 mrad. The observation angle has been fixed to $\theta = 0°$, meaning that the collimator is centered on the electron bunch trajectory. We then compared the simulation results with the analytical estimations given by Eqs. (8), (9), (10) and (11). For that, we assumed a head-on collision (α = 180°) and that the laser driving the ICS process is at the diffraction limit (M^2 = 1), transversely round with an rms transverse size equal to the average of σ_x and σ_y for the electron bunch at the transverse focal point (see Tables 3 and 4), with a wavelength λ_L = 1.048 µm, an energy U_L = 0.1 J and an rms length σ_{tL} = 1 ps. For the simulations with CAIN we assume that the focal point of the laser and the electron bunch are coincident in space and time, and for the analytical estimations we in addition assume an optimal space-time overlap (see Eq. (12)). The results are presented in Table 6, where E_X denotes the average photon energies for the collimated pulse (CAIN) or the on-axis X-ray energy for <E> (analytical model). σ_{tX} is the rms duration predicted by CAIN for the collimated X-ray pulse. Fig. 17 presents the normalized energy spectra of the collimated photon pulses simulated with CAIN for the 6 cases displayed in Table 6. Note that in Fig. 17 the different peak X-ray energies for the different values of Q simply come from the fact that <E> is different for these different cases (see Tables 3 and 4).

Table 6. Comparison of the X-ray pulse properties predicted by the CAIN simulations (first value in each cells) with the ones predicted by the analytical formulas presented in Sec. 4.2 (second value in each cells). E_X denotes the average photon energies for the collimated pulse (CAIN) or the on-axis X-ray energy for <E> (analytical model). σ_{tX} is the rms duration predicted by CAIN for the collimated X-ray pulse.

f (GHz)	Q (pC)	E_X (keV)	N_γ (10^5)	$N_{\gamma,\theta coll}$ (10^3)	$\sigma_{\nu\gamma}/\nu_\gamma$ (%)	σ_{tX} (fs)
300	0.1	5.90/ 5.96	0.58/ 0.65	1.6/ 1.3	0.90/ 2.17	0.46
150	0.1	4.61/ 4.66	0.59/ 0.66	1.3/ 1.0	0.70/ 1.73	0.71
300	1	5.76/ 5.85	3.2/ 3.2	8.9/ 6.4	1.64/ 2.47	1.30
150	1	4.30/ 4.33	4.3/ 4.7	9.1/ 6.9	0.93/ 1.65	1.81
300	2.5	5.97/ 6.07	3.8/ 3.9	11/ 8.0	2.54/ 3.32	2.35
150	5	4.34/ 4.40	12/ 12	24/ 18	2.44/ 2.89	3.62

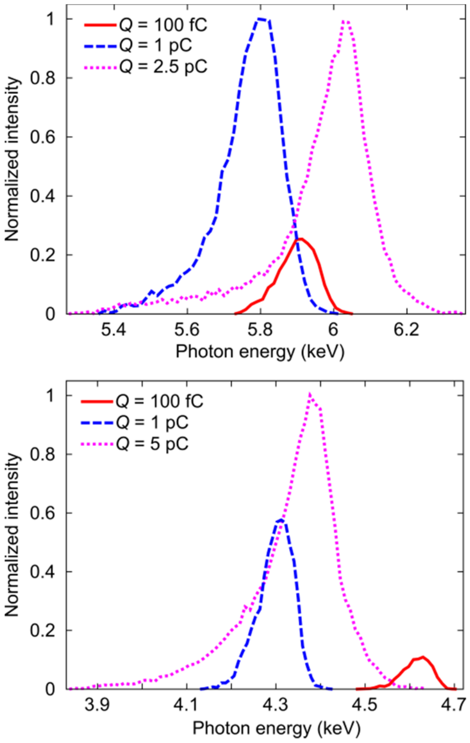

Fig. 17. Normalized energy spectra of the collimated photon pulses simulated with CAIN for the 6 cases displayed in Table 6. f = 300 GHz (top plot) and f = 150 GHz (bottom plot).

---

[c] In our cases the electron bunch is never totally transversely symmetric. We therefore use the average of σ_x and σ_y and the average of ε_x and ε_y to compute $\hat{\rho}$ with Eq. (13).

Table 6 shows that E_X is consistent between CAIN and the analytical model, since the difference is at maximum 1.7% and can be attributed to the difference in the definition of E_X. N_γ is also in a good agreement with a difference varying between 0% and 12% according to the case, but it is to note that CAIN always predicts a smaller number of photons than the analytical model. The most likely explanation for this is that the space-time overlap between the electron bunch and the laser pulse driving the ICS process is not perfect, which is taken into account with CAIN but not by the analytical model. $N_{\gamma,\theta coll}$ shows higher differences ranging from 18.8% to 28%. The agreement is however still fair enough so that the analytical model can be used to obtain a good first estimation of $N_{\gamma,\theta coll}$. It is noteworthy that in this case CAIN always predicts a higher number of collimated photons than the analytical model. The rms relative bandwidth $\sigma_{v\gamma}/v_\gamma$ shows much stronger differences, with CAIN always predicting a smaller value than the analytical model, and a clear evolution with the value of the bandwidth. For the cases with Q = 5 pC and Q = 2.5 pC (higher bandwidth), the agreement is still acceptable since the difference is of the order of 20% to 30%. But for the cases with $Q \leq 1$ pC, the analytical model does not give an estimation of $\sigma_{v\gamma}/v_\gamma$ close to be in agreement with CAIN. Indeed, the difference reaches 50% to 80% at Q = 1 pC (intermediate bandwidth) and around 140% at Q = 100 fC (lower bandwidth).

Table 6 also shows an important feature in the evolution of $N_{\gamma,\theta coll}$ when Q increases. Namely between the cases at Q = 100 fC and Q = 1 pC, it increases by a factor close to the increase of Q (6 for f = 300 GHz and 7 for f = 150 GHz), while between the cases at Q = 1 pC and the ones at higher Q it increases by a smaller factor (1.2 for f = 300 GHz and 2.5 for f = 150 GHz). This is due to the fact that the level of transverse focusing cannot be maintained when Q increases too much (see Tables 3 and 4) leading to a slower increase of the factor Q/σ_x^2 involved in Eq. (10). On the other hand, Table 6 shows that $\sigma_{v\gamma}/v_\gamma$ increases more than linearly with Q. This is due to the fact that σ_E and ε_x present this behavior (see Tables 3 and 4) leading to such an increase of the corresponding terms involved in Eq. (11). Table 6 therefore demonstrates that the parameter $\hat{\rho}$ defined in Eq. (13) is an excellent indicator to determine which working point is the best compromise between the number of photons and the relative bandwidth of these photons.

Fig. 17 clearly shows that when Q increases, a tail of low energy photons is developing itself in the energy spectrum, which greatly penalizes the achievable rms bandwidth. This is especially visible for the higher charges in the two plots. This tail is directly coming from a similar tail in the electron bunch energy spectrum (see Fig. 16), developing when Q increases. As a result, the achievable $\sigma_{v\gamma}/v_\gamma$ could greatly be improved if a system to filter the emitted X-rays would be used after the ICS point and collimation. To illustrate this fact, Fig. 18 displays the evolution of $N_{\gamma,\theta coll}$ and $\sigma_{v\gamma}/v_\gamma$ as a function of a lower energy cut (meaning that all the photons below this energy are removed from the spectrum) for the cases at f = 300 GHz/Q = 2.5 pC and f = 150 GHz/Q = 5 pC shown in Table 6 and Fig. 17. As a numerical example, if all the photons with an energy lower than 5.8 keV are removed for the case with Q = 2.5 pC and f = 300 GHz (Fig. 17 top plot), $N_{\gamma,\theta coll}$ = 9.8*10^3 (reduction of only 11%) and $\sigma_{v\gamma}/v_\gamma$ = 1.43% (reduction of 44%). For the case with Q = 5 pC and f = 150 GHz (Fig. 17 bottom plot), if all the photons with an energy lower than 4.25 keV are removed $N_{\gamma,\theta coll}$ = 2.0*10^4 (reduction of only 17%) and $\sigma_{v\gamma}/v_\gamma$ = 1.43% (reduction of 42%).

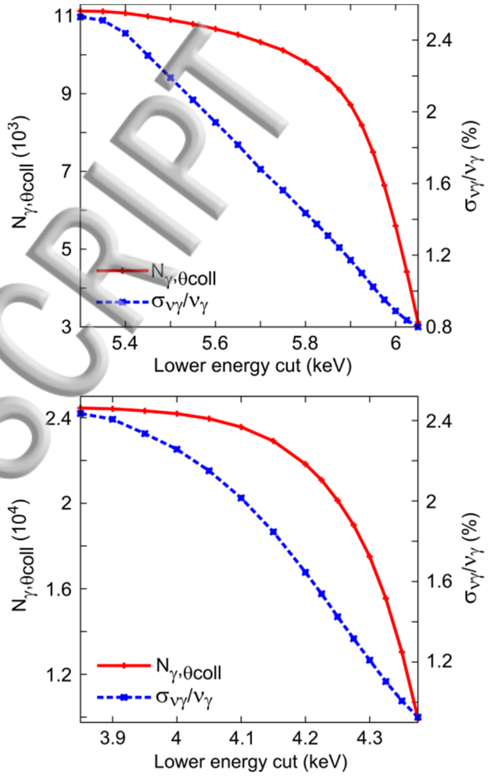

Fig. 18. Evolution of $N_{\gamma,\theta coll}$ and $\sigma_{v\gamma}/v_\gamma$ as a function of a lower energy cut for the cases at f = 300 GHz/Q = 2.5 pC (top) and f = 150 GHz/Q = 5 pC (bottom) shown in Table 6 (properties) and Fig. 17 (spectra). Lower energy cut means here that all the photons below this energy are removed from the spectrum.

For the results presented in Table 6 we fixed U_L to 0.1 J. A way to increase the number of photons per pulse would be to increase U_L. However, one has to be careful that this will result in an increase of the laser parameter a_0 and therefore of the bandwidth of the X-ray pulse (see Eq. (11)). A trade-off has therefore to be found to fix the value of U_L. Fig. 19 shows, for the case with Q = 1 pC and f = 150 GHz in Table 6, the evolution of $N_{\gamma,\theta coll}$ and $\sigma_{v\gamma}/v_\gamma$ with U_L and illustrates this fact. It shows an expected almost linear increase of $N_{\gamma,\theta coll}$ with U_L (see Eq. (10)) and an approximately quadratic increase of $\sigma_{v\gamma}/v_\gamma$ with U_L, expected from Eq. (11) since a_0^2 is at maximum around 0.14 in this case. Fig. 19 shows that $N_{\gamma,\theta coll}$ can be increased from 9.1*10^3 to 8.7*10^4 when U_L increases from 0.1 J to 1 J, but at the cost of an increase of $\sigma_{v\gamma}/v_\gamma$ from 0.93% to 1.87%. A good trade-off is for example U_L = 0.4 J where $N_{\gamma,\theta coll}$ = 3.6*10^4 and $\sigma_{v\gamma}/v_\gamma$ = 1.12%, and we will use this value of U_L for the following subsection. It is noteworthy that this increase of the bandwidth with U_L, contrary to the increase of the bandwidth with Q aforementioned, is not driven by the appearance of tails in the photon energy spectrum.

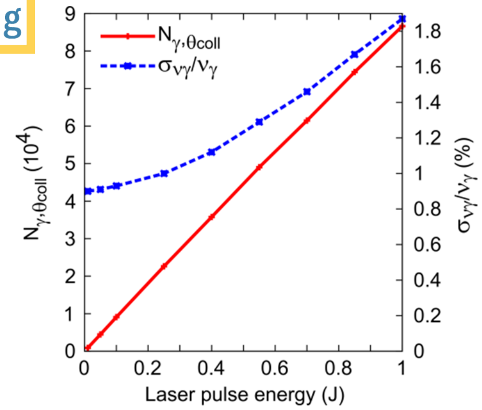

Fig. 19. Evolution of $N_{\gamma,\theta coll}$ and $\sigma_{\nu\gamma}/\nu_\gamma$ as a function of U_L for the case with Q = 1 pC and f = 150 GHz in Table 6.

4.3. Tunability potential of the X-ray pulse

In this sub-section, we will describe how E_X could be tuned and in which range it could be tuned for the concept proposed in this paper.

First, as explained in Sec. 4.1, one has to remember that changing the accelerating frequency from f = 150 GHz to f = 300 GHz comes with a significant change of $<E>$ at the ICS point (see Tables 3 and 4). This naturally translates into significantly different values of E_X for the simulated X-ray pulses (see Table 6). One can therefore think to tune E_X by switching between different DLW operating at different frequencies for the TM_{01} mode. This would be possible with DLW since, thanks to their small dimensions (diameter in the millimeter range and length in the range of ten cm), they are fast to be produced and easy to be exchanged in a beamline contrary to the conventional RF accelerating structures. Note that the THz source powering the DLW will have to be tunable in this case.

Then, it is straightforward from Eq. (8) that using the second harmonic of an IR laser, therefore at λ_L = 524 nm in our case, will double E_X. Therefore, using an IR laser able to produce hundreds of mJ when converted to its second harmonic, which is possible with a Joule-class IR laser according to the already demonstrated conversion efficiency (see for example Ref. 25), would double the achievable range for the X-ray source proposed in this paper.

Combining the two aforementioned tuning options, for the cases with Q = 1 pC shown in Tables 3 and 4, would result in the possibility to generate 4 different values of E_X: $E_X \approx 4.3$ keV (f = 150 GHz with λ_L = 1048 nm), $E_X \approx 5.7$ keV (f = 300 GHz with λ_L = 1048 nm), $E_X \approx 8.6$ keV (f = 150 GHz with λ_L = 524 nm) and $E_X \approx 11.5$ keV (f = 300 GHz with λ_L = 524 nm).

We then investigate the possibilities to establish a continuum between these 4 energies. Looking at Eq. (8), it appears that three ways remain to vary E_X. The first one would be to vary the observation angle θ, which was equal to 0° in Sec. 4.2, namely to collimate the photon pulse with a collimator movable in the plane perpendicular to the electron bunch trajectory. However, with an increase of θ, $\sigma_{\nu\gamma}/\nu_\gamma$ has been found to strongly increase compared to the case $\theta = 0°$ and this option was therefore not retained. The second option would be to vary the collision angle α between the electron bunch and the laser. In this case, $N_{\gamma,\theta coll}$ has been found to decrease too fast compared to $\alpha \approx 180°$ (head-on collision) before the desired variation of E_X can be achieved and the option was also not retained. The third and last option, which has been retained, is to vary γ^2 (namely $<E>$). We choose to do that by starting from the four cases aforementioned and then reducing the field amplitude E_{ml} in the THz linac. For each simulated value of E_{ml}, the injection phase into the THz linac and the quadrupole triplet settings have been optimized again. Fig. 20 shows $N_{\gamma,\theta coll}$ and $\sigma_{\nu\gamma}/\nu_\gamma$ as a function of E_X for θ_{coll} = 4 mrad and U_L = 400 mJ (top plot). It also shows (bottom plot) $N_{\gamma,\theta coll}$ and θ_{coll} as a function of E_X for U_L = 400 mJ and $\sigma_{\nu\gamma}/\nu_\gamma$ fixed to 1.5% (except for the two cases pointed by black arrows where $\sigma_{\nu\gamma}/\nu_\gamma$ exceeds 1.5% and θ_{coll} remains 4 mrad).

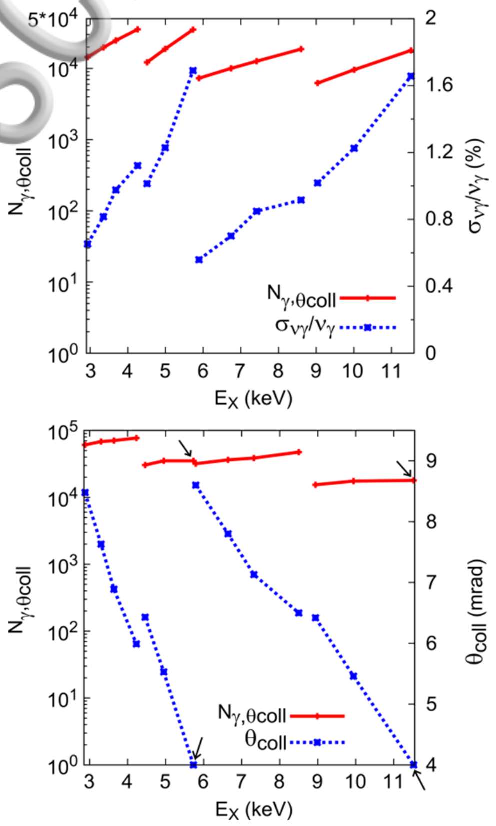

Fig. 20. Top: $N_{\gamma,\theta coll}$ and $\sigma_{\nu\gamma}/\nu_\gamma$ as a function of E_X for θ_{coll} = 4 mrad. Bottom: $N_{\gamma,\theta coll}$ and θ_{coll} as a function of E_X for $\sigma_{\nu\gamma}/\nu_\gamma$ = 1.5% (except for the two cases pointed by black arrows, where $\sigma_{\nu\gamma}/\nu_\gamma$ > 1.5% for θ_{coll} = 4 mrad, which are left identical to the top plot). U_L = 400 mJ; Q = 1 pC. For f = 150 GHz, E_{ml} = 77 MV/m, 90 MV/m, 100 MV/m and 115 MV/m (case with Q = 1 pC in Table 4) have been simulated. For f = 300 GHz, E_{ml} = 92 MV/m, 101 MV/m and 115 MV/m (case with Q = 1 pC in Table 3) have been simulated.

Fig. 20 (top) shows that a decrease of E_{ml} is well suited to tune E_X in a continuous way from around 3 keV up to around 11.5 keV. In fact, despite it shows that $N_{\gamma,\theta coll}$ decreases when E_{ml} decreases, due to an increase of σ_x and σ_y at the ICS point, this decrease is much smaller than for a change of the collision angle α (where it exceeds a factor 30) since it is of a factor 5.7 at maximum: from $3.5*10^4$ at $E_X = 4.3$ keV ($f = 150$ GHz, $E_{ml} = 115$ MV/m and $\lambda_L = 1.048$ μm) and $E_X = 5.7$ keV ($f = 300$ GHz, $E_{ml} = 115$ MV/m and $\lambda_L = 1.048$ μm) to $6.2*10^3$ at $E_X = 9$ keV ($f = 300$ GHz, $E_{ml} = 92$ MV/m and $\lambda_L = 524$ nm). It also shows that $\sigma_{v\gamma}/v_\gamma$ does not increase with a decrease of E_{ml}, and is actually even strongly decreasing: for example from 1.12% at $E_X = 4.3$ keV ($f = 150$ GHz, $E_{ml} = 115$ MV/m and $\lambda_L = 1.048$ μm) to 0.65% at $E_X = 2.9$ keV ($f = 150$ GHz, $E_{ml} = 77$ MV/m and $\lambda_L = 1.048$ μm). This is due to the fact that the lower value of $<E>$ comes with stronger space-charge forces, despite the increase of σ_x and σ_y at the ICS point, which makes the scheme of reduction of σ_E presented in Sec. 3.1 more efficient and therefore reduce it. As explained in Sec. 3.1.1, this reduction of σ_E, and subsequently of $\sigma_{v\gamma}/v_\gamma$, comes with the drawback that σ_t, and subsequently σ_{tX}, increases: from 1.5 fs to 1.8 fs for $f = 300$ GHz between $E_{ml} = 115$ MV/m and $E_{ml} = 92$ MV/m, and from 1.8 fs to 3.3 fs for $f = 150$ GHz between $E_{ml} = 115$ MV/m and $E_{ml} = 77$ MV/m.

The decrease of $\sigma_{v\gamma}/v_\gamma$ with E_{ml} allows significantly increasing $N_{\gamma,\theta coll}$, by increasing θ_{coll}, for the cases with $E_{ml} <$ 115 MV/m without that $\sigma_{v\gamma}/v_\gamma$ exceeds the ones obtained for the cases with $E_{ml} = 115$ MV/m. Fig. 20 (bottom) shows as an example that increasing θ_{coll} such that $\sigma_{v\gamma}/v_\gamma$ becomes equal to 1.5% for all the cases (except the two cases pointed by black arrows where it exceeds 1.5% at $\theta_{coll} = 4$ mrad and which are left identical to the top plot) would allow obtaining $N_{\gamma,\theta coll}$ ranging from $1.5*10^4$ at $E_X = 8.9$ keV ($f = 300$ GHz, $E_{ml} = 92$ MV/m, $\lambda_L = 524$ nm and $\theta_{coll} = 6.4$ mrad) up to $7.7*10^4$ at $E_X = 4.2$ keV ($f = 150$ GHz, $E_{ml} = 115$ MV/m, $\lambda_L = 1.048$ μm and $\theta_{coll} = 6.0$ mrad). However, this increase of θ_{coll} comes with the drawback that the length of the X-ray pulse also increases. This is due to the simple geometrical effect that photons with a higher divergence take a longer time to reach a given Z position along the beamline than photons with lower divergence. This effect superimposes with the increase of σ_t when E_{ml} decreases previously described and leads to a significant increase of σ_{tX}: from 1.5 fs to 2.6 fs for $f = 300$ GHz between $E_{ml} = 115$ MV/m ($\theta_{coll} = 4$ mrad) and $E_{ml} = 92$ MV/m ($\theta_{coll} = 6.4$ mrad), and from 1.8 fs to 4.7 fs for $f = 150$ GHz between $E_{ml} = 115$ MV/m ($\theta_{coll} = 4$ mrad) and $E_{ml} = 77$ MV/m ($\theta_{coll} = 8.5$ mrad).

5. Some technical requirements for the proposed concept

5.1. Properties of the DLW and of the THz pulse driving it

The procedure and the formulas used to determine the properties of the DLW used as accelerating structure and of the THz pulse driving it have been exposed in Sec. 2. In this section, we will introduce the requirements for the DLW and the THz pulse needed to achieve the potential working points presented in Sec. 4. We consider two cases for this purpose. The first one is the standard case, where we assume $2a$ equal to the THz pulse wavelength. The second one is an aggressive option where we reduce a by 20%. Table 7 shows that the aggressive option brings the benefit to reduce E_{THz} by around 24% whatever f. This is explained by the fact that the decrease of $<P>_{THz}$ (due to the decrease of the DLW cross-section) overcomes the increase of T (due to the decrease of v_g). One can also see that the decrease of a leads to an increase of the dielectric thickness $b - a$ required to have the desired v_{ph}. This means that the tolerances for the DLW production are slightly relaxed. However, one must not forget that this aggressive option comes with two major drawbacks. First, the margins for beam dynamics, concerning the bunch injection and the charge transmission throughout the linac, are reduced. Then, the coupling efficiency of the THz pulse into the linac is also reduced. A compromise has therefore to be found between all the aforementioned aspects in order to set the value of a.

Table 7. Properties of the DLW and of the THz pulse driving it required to generate the electron bunch properties at the ICS point presented in Tables 3 and 4. Quartz ($\varepsilon_r = 4.41$) is considered as a dielectric-loading. The cases in normal font are the standard cases with 2*a* equal to the THz wavelength. The cases in italic are aggressive options with 2*a* 20% smaller than the THz wavelength. The underlined case is an intermediate frequency, not yet tested in beam dynamics simulations.

f (GHz)	a (μm)	$b - a$ (μm)	v_{ph} (c)	v_g (c)	T (ps)	$<P>_{THz}$ (MW)	E_{THz} (mJ)
300	500	90.35	1	0.513	407	23.3	9.5
300	*400*	*100.77*	*1*	*0.414*	*607*	*11.8*	*7.2*
150	1000	180.13	1.002	0.514	407	92.7	37.7
150	*800*	*201.12*	*1.002*	*0.415*	*607*	*47.0*	*28.5*
230	650	118.06	1	0.511	409	39.4	16.1

Table 7 also shows that E_{THz} required at $f = 150$ GHz is around four times higher than the one required at $f = 300$ GHz. It directly follows from the fact that a has to typically be two times bigger, implying that the DLW cross-section and therefore $<P>_{THz}$ required to have the same E_{ml} is multiplied by a factor around 4. Regarding the current performances in THz generation (see Sec. 5.2), the level of $<P>_{THz}$ required at $f = 150$ GHz is too high to be reached in a predictable future. However, it is visible by comparing Table 4 to Table 3 that it would lead to a significant improvement of the achievable electron bunch properties at the ICS point, which should be a motivation to develop powerful THz sources at $f \approx 150$ GHz. Finally, the last line of Table 7 indicates that an intermediate frequency ($f = 230$ GHz), not yet tested in ASTRA beam dynamics simulations, could be an interesting trade-off between the lower THz power required at $f = 300$ GHz and the better bunch quality achievable at $f = 150$ GHz.

5.2. THz generation

As shown in Sec. 5.1 the amount of energy required in the THz pulse driving the THz linac is quite large since it is still close to 10 mJ for $f = 300$ GHz (power between 10 and 20 MW) and to 30-40 mJ at $f = 150$ GHz (power between 50 and 100 MW). It is therefore essential to compare the different methods currently used to generate multi-cycle THz pulses in order to have a first insight in their present and future capabilities to deliver a multi-cycle THz pulse with the properties given in Sec. 5.1 to drive the THz linac.

A first type of THz pulse generation technique is based on optical rectification of an infrared laser pulse in non-linear optical crystals, like lithium-niobate for example. This kind of approach has already been used to perform the first demonstration experiment of electron acceleration in a THz-driven DLW[26]. However, this kind of technique is currently limited by a low IR/THz conversion efficiency, due to the fact that it is quite young and still in a phase of development. The current record of energy in a single multicycle THz pulse generated via this type of technique is slightly above 0.4 mJ at f = 361 GHz with a maximal conversion efficiency of 0.15%[27]. Several schemes have been proposed and simulated to increase the IR/THz conversion efficiency up to 5% and even 10%, but they have not been experimentally demonstrated by now[28-30]. This option of THz generation is the one chosen for the AXSIS project[4,27].

A second type of THz pulse generation technique is the one used in the gyrotron devices, based on electron cyclotron resonance in a circular cavity[31]. The current state-of-the-art gyrotrons are able to deliver $<P>_{THz}$ of 1 to 2 MW in the vicinity of f = 150 GHz[32-35] and a strong research is ongoing to reach the 1 MW level in the vicinity of f = 300 GHz[35,36]. This is significantly below the requirements shown in Table 7. However, it is noteworthy that the pulse lengths deliver by the gyrotrons are much longer than the requirements in Table 7, the shortest we found in the literature being of 3 µs in Ref. 32. Consequently, E_{THz} delivered by the gyrotrons is much higher than the requirements shown in Table 7. It means that if a way is found to compress the THz pulse coming from a gyrotron, the requirements on $<P>_{THz}$ in Table 7 could be met. This has to our knowledge however not yet been studied. Furthermore, other aspects than the pulse power are relevant and would have to be studied before considering using a gyrotron as power source for the THz linac in our concept. For example, the shot-to-shot phase stability which is of primary importance for our concept (see Sec. 5.3.3) would have to be taken into account.

A third type of THz pulse generation technique is the accelerator-based emission of radiation in dipole or undulator magnets (coherent synchrotron radiation[37] and free electron laser (FEL)[38]), like this is for example done in a tunable way at the TELBE facility[39]. Calculations for a THz-FEL based on the PITZ facility at DESY/Zeuthen are currently ongoing, and suggest that around 2 mJ THz pulses with $<P>_{THz}$ significantly in excess of the requirements shown in Table 7 (for f = 300 GHz) could be generated in this way[40]. However, these pulses would remain significantly shorter than the requirements for T shown in Table 7[40].

A fourth and last type of generation of accelerating field with a frequency in the THz range is to generate wakefields in a structure (a DLW for example) and with a driver electron bunch having properties such that the generated wakefields are in the THz range of frequency[41,42]. A demonstration experiment has recently been performed with 20 GeV driver and witness bunches at SLAC, with a 10 cm long quartz DLW having a 400 µm vacuum diameter. In this experiment, the TM_{01} mode was excited at 422 GHz by the 1.6 nC drive beam and a 320 MV/m accelerating field has been experienced by the 1 nC witness bunch with 80% energy extraction efficiency[43]. A scheme has been proposed to optimize the intensity and tune the frequency of the wakefield generated on a moderate energy (50-100 MeV) conventional accelerator[44], and also to efficiently extract this power from the structure in which it has been generated[45]. These kinds of THz accelerating field generation techniques via wakefields, based on conventional RF accelerators, are at the time of writing the most promising candidates to fulfil the THz pulse requirements shown in Table 7. Despite the fact that they are to date not compatible with the goal of a compact layout as intended for the concept presented in our paper, they could be of great interest to produce enough THz power for performing demonstration experiments.

Finally, it has to be mentioned that a scheme based on Inverse Free Electron Laser (IFEL) has been recently experimentally demonstrated to significantly increase the interaction length between an electron bunch and a THz pulse[46], which is normally limited in a DLW by the significantly lower than c group velocity of the THz pulse (see Table 7). This scheme could be of great interest to reduce T and subsequently E_{THz} required in Table 7, allowing even using single-cycle THz pulses instead of multi-cycle ones. Indeed, as previously mentioned, the required value of T is a limiting factor for the technique of THz pulse generation based on FEL radiation. Furthermore, by bringing down the requirements on E_{THz} in Table 7 below 100 µJ at f = 300 GHz, this possibility to use single-cycle THz pulses would make the use of laser-based THz sources possible since this level is achievable mainly by only scaling up the current setups used for single-cycle THz pulse generation according to Ref. 47.

5.3. Influence of various jitters

In this subsection, we will give a first evaluation of the influence of various jitters on the electron bunch properties simulated at the ICS point and on the arrival time of the electron bunch at the ICS point, which is important because the electron bunch has to be synchronized with the laser driving the ICS process to maximize its efficiency. We will consider only the case f = 300 GHz, since it is the most demanding on the jitter point of view. For the case f = 150 GHz, all the fluctuations of the electron bunch properties at the ICS point presented in this section would be less important.

To evaluate the influence on the electron bunch properties at the ICS point of a single jitter, we choose to use ASTRA[12] in combination with a simple self-written Matlab code. We start from a bunch distribution simulated at the THz linac entrance, corresponding to the case described in details in Sec. 3.1, and we use it to run jitter simulations up to the ICS point. We first run a scan with ASTRA where the parameter involved for the considered jitter is varied step-by-step in a certain range (for example E_{ml} is varied between 100 MV/m and 130 MV/m by step of 1 MV/m). Then, the obtained points are fitted with Matlab to obtain continuous curves over the desired range. Finally, a jitter following a Gaussian distribution with a standard deviation σ_{jit} respective to the

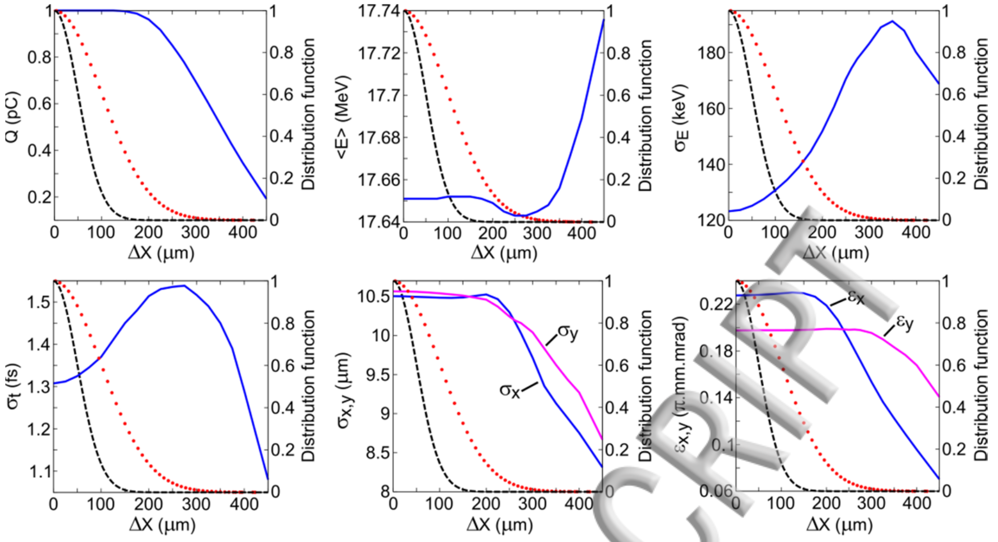

Fig. 21. Electron bunch properties at the ICS point as a function of the transverse offset Δ*X* at the THz linac entrance (solid curves). Dotted curves: Distribution function of Δ*X* for σ_{jit} = 100 µm. Dashed curves: Distribution function of Δ*X* for σ_{jit} = 50 µm.

nominal value is simulated with Matlab. Namely, a large number of N_{err} values of the jittering parameter is randomly generated according to the aforementioned distribution (with a cutoff at +/- 3 σ_{jit}) and for each of these values the electron bunch properties at the ICS point are determined using the curves previously obtained with Matlab.

Such a simulation delivers histograms of the electron bunch properties at the ICS point. Normalizing these histograms, such that their integrals become equal to 1, give access to the distribution functions of the electron bunch properties at the ICS point. A local value of these distribution functions represents the probability density to have the associated electron bunch properties at the ICS point under the assumed jitter. More information are then given by the partition functions, which are the integrals of the distribution functions, since the probability to obtain electron bunch properties in a certain range can be deduced from them[d].

5.3.1. Pointing jitter

The first studied jitter is the pointing jitter of the electron bunch at the entrance of the THz linac, which typically comes from an initial pointing jitter of the UV laser pulse driving the RF-gun. This jitter affects the electron bunch properties and arrival time at the ICS point because the transverse component of the field experienced by the bunch is varying, it is zero for an on-axis bunch, leading to a varying path and travel time of the bunch in the THz linac.

The varying parameter in ASTRA for this jitter is the bunch transverse offset at the THz linac entrance, along the horizontal direction *x* in our case, later referred to as Δ*X*. Fig. 21 shows the results of the parameter scan performed with ASTRA for Δ*X* = 0 to 450 µm. The two Gaussian distributions later considered for the jitter in the present subsection are superimposed on Fig. 21.

Fig. 22 displays the distribution and partition functions of the electron bunch properties at the ICS point for σ_{jit} = 100 µm around the on-axis injection (N_{err} = 1220000).

Fig. 22 first shows that 87% of the cases simulated present no charge losses despite the assumed vacuum radius for the THz linac is of only 500 µm. This is explained by the fact that in our concept the electron bunch is still focusing itself when injected into the THz linac (see for example Fig. 10 (left plots)), practically meaning that the charge losses only happens right at the THz linac entrance which then acts as a collimator. As a consequence charge losses happen only when the initial transverse offset becomes significantly larger than 100 µm, which is a low probability event in our simulation. This results in the long tail of low probability events observed in Fig. 22 for *Q*.

Fig. 22 also demonstrates that <*E*> and the transverse electron bunch properties (σ_x, σ_y, ε_x and ε_y) at the ICS point are almost not affected by a pointing jitter of 100 µm rms at the THz linac entrance. Indeed, the distribution functions of these properties present sharp peaks around the nominal values (obtained with a zero jitter), and long tails of low probability events directly resulting from the low probability events where some charge is lost.

Fig. 22 finally shows that the longitudinal electron bunch properties (σ_E and σ_t) are more affected by the simulated jitter. While this is anecdotic for σ_t, which remains in the single femtosecond order for all the simulated events, this is relevant for σ_E (which can increase by up to 45%) since the bandwidth of a photon pulse generated through ICS is strongly dependent on it (see Eq. (11)). This strong increase of σ_E concerns only a minority of cases, since 90% of the simulated events present a value of σ_E less than 10% greater than the nominal value. However, a smaller pointing jitter than 100 µm rms at the THz linac entrance would be preferable for the stability of the source bandwidth.

---

[d] Given a distribution function f(*x*) ≠ 0 for *x* in a finite real interval [A,B] with B > A, the partition function F(*x*) is defined for *x* > A as $F(x) = \int_A^x f(u)du$. Considering x_1 and x_2 included in [A,B] with $x_2 > x_1$, then F(x_2) – F(x_1) is the probability to obtain *x* in the interval [x_1,x_2].

Fig. 23 displays simulation results for σ_E and σ_t at the ICS point for σ_{jit} = 50 µm (N_{err} = 1220000) around the on-axis injection. It shows that σ_{jit} = 50 µm would be much better since the increase of σ_E would be only of 10% at maximum, and 90% of the cases will present σ_E less than 3% greater than the nominal value.

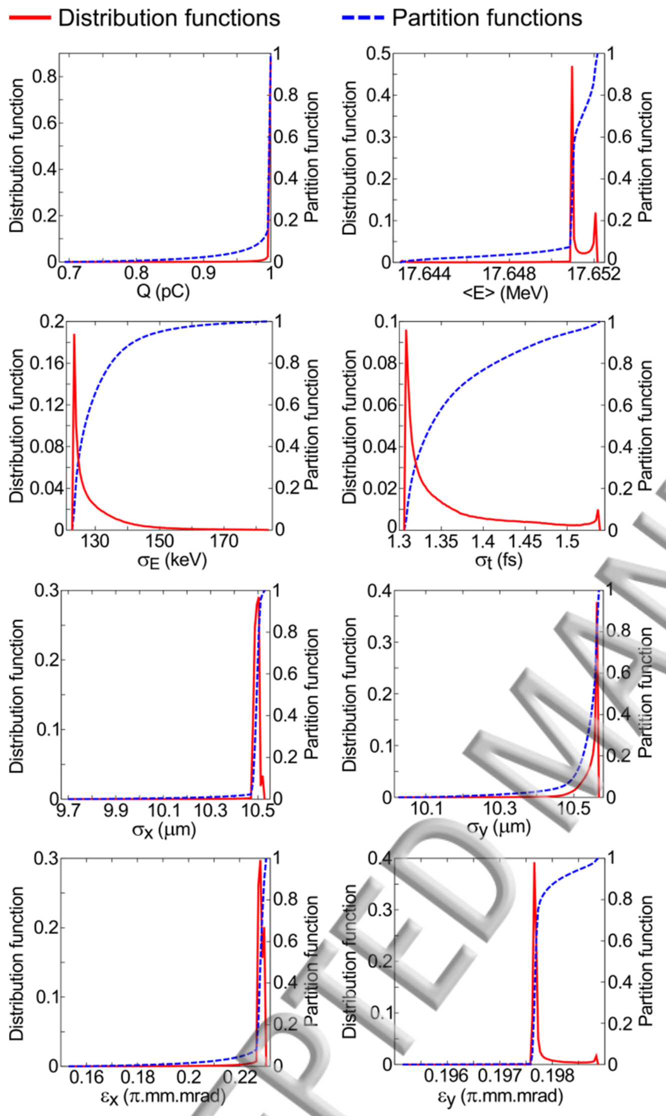

Fig. 22. Distribution and partition functions of the electron bunch properties at the ICS point under the influence of a jitter of ΔX at the THz linac entrance with σ_{jit} = 100 µm around ΔX = 0.

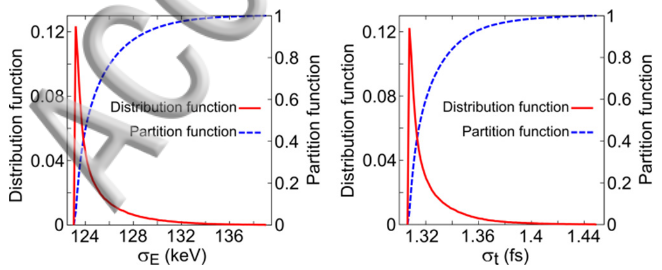

Fig. 23. Distribution and partition functions of the electron bunch rms energy spread and bunch length at the ICS point under the influence of a jitter of ΔX at the THz linac entrance with σ_{jit} = 50 µm around ΔX = 0.

5.3.2. Jitter of the THz linac field amplitude

The second studied jitter is the jitter of the amplitude of the accelerating field in the THz linac E_{ml}, which typically comes from a jitter of the power delivered by the THz source. For example, for a THz pulse generated by optical rectification of an infrared laser (see Sec. 5.2) it will come from a jitter of the amplitude of this laser. This jitter affects the electron bunch properties at the ICS point because the injection phase φ_0 of the bunch into the THz linac becomes not optimal, since the optimal injection phase varies with the amplitude of the accelerating field.

The varying parameter in ASTRA for this jitter is the amplitude of the accelerating field in the THz linac. Fig. 24 shows the results of the parameter scan performed with ASTRA for E_{ml} = 100 to 130 MV/m. The two Gaussian distributions later considered for the jitter in the present subsection are superimposed on Fig. 24. The bunch charge is not displayed since no charge losses happened in any cases.

Fig. 25 displays the distribution and partition functions of the electron bunch properties at the ICS point for σ_{jit} = 3% (3.45 MV/m) around E_{ml} = 115 MV/m (N_{err} = 2000000). The bunch charge is here also not displayed since no charge losses happened in any cases.

Fig. 25 demonstrates that all the electron bunch properties at the ICS point are affected by a jitter of the accelerating field amplitude in the THz linac, but not all with the same importance.

First, the jitter of the accelerating field amplitude in the THz linac trivially comes with significant variations of <*E*> at the ICS point, since the injection phase into the THz linac remains the same for all the simulated events. This results in a variation of the energy E_X of the generated X-ray and would therefore be penalizing for the applications requiring a specific X-ray energy. On the other hand, this would not have any effect on the applications only requiring having E_X above a certain threshold, and also the applications only requiring knowing E_X if it (or <*E*>) can be measured on a shot-to-shot basis.

Second, the variations of the transverse emittances at the ICS point are acceptable. Indeed, ε_x remains within +/- 2% of the nominal value and ε_y is at maximum 4% higher than the nominal value. Note that about 50% of the simulated events have lower transverse emittances than the nominal value.

Then the variations of the bunch length at the ICS point, while being up to +35%, are not the main concern since σ_t remains in the single femtosecond order which is one of the main goals of our concept.

On the other hand, the variations of the transverse sizes at the ICS point are much more significant. In fact, σ_x can increase by 50% and σ_y by 120%. This would decrease drastically the number of photons in the generated X-ray pulse, since it depends quadratically on the transverse size (see Eq. (10)). These variations of σ_x and σ_y are due to the fact that when <*E*> is changing the nominal quadrupole triplet settings are not appropriate anymore to symmetrically focus the electron bunch and right at the intended position of the ICS point. Namely, the positions of the focal points for σ_x and

This manuscript was accepted by J. Appl. Phys. Click here to see the version of record.

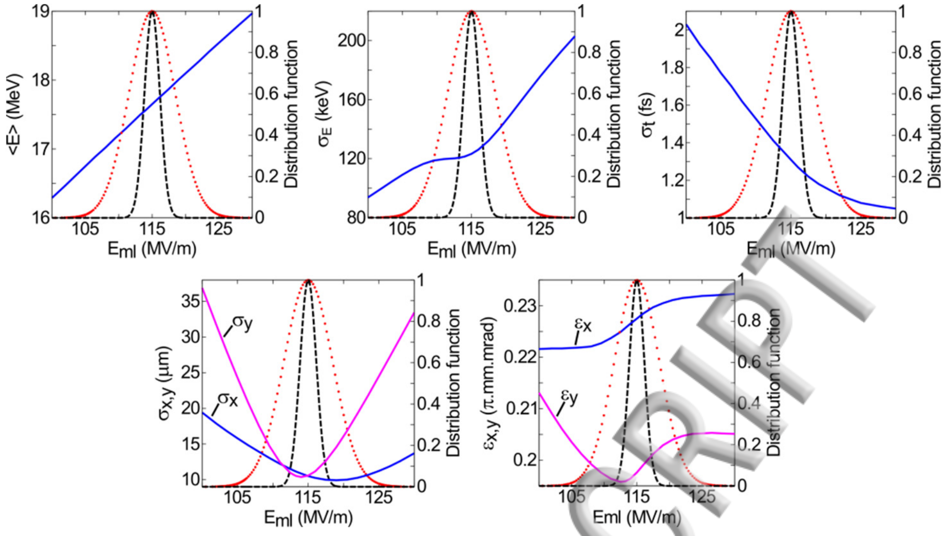

Fig. 24. Electron bunch properties at the ICS point as a function of the THz linac field amplitude E_{ml} (solid curves). Dotted curves: Distribution function of E_{ml} for σ_{jit} = 3%. Dashed curves: Distribution function of E_{ml} for σ_{jit} = 1%.

σ_y become at different Z positions along the beamline and are located before or after the intended position of the ICS point. Note that σ_y is more affected than σ_x because this is the plane where the focusing is the sharpest (since it is first defocused) as shown in Fig. 3.

These variations of the positions of the focal points, by up to a few cm, are responsible for a shift from its optimal value of the parameter ΔZ_{lt} defined in Sec. 3.1.2, and therefore for the variations observed for σ_E at the ICS point. Indeed, as explained in Secs. 3.1.1 and 3.1.2 the scheme of space-charge induced reduction of the correlated energy spread used in our concept is very sensitive to the position of the transverse focal point of the electron bunch. The variations of σ_E are almost equally shared between both sides of the nominal value, since 45% of the simulated events exhibit a lower value of σ_E. However, the tail is much longer on the side of the higher values of σ_E and extends up to +40% of the nominal value. As previously explained this is highly penalizing for the bandwidth of the generated X-ray pulse (see Eq. (11)).

The strong negative effects of the variations of $<E>$, σ_x, σ_y and σ_E observed in Fig. 25 indicates that a jitter of E_{ml} with σ_{jit} = 3% around E_{ml} = 115 MV/m is too strong to allow for reasonably stable properties of the electron bunch at the ICS point, and therefore of the generated X-ray pulse.

Fig. 26 shows simulation results for σ_x, σ_y, σ_E and $<E>$ at the ICS point for the smaller jitter σ_{jit} = 1% (N_{err} = 2000000) around E_{ml} = 115 MV/m. It shows that this smaller jitter would provide much more stable electron bunch properties at the ICS point and would start to be reasonable for operation. In fact, the variations of σ_x (σ_y) drop to +/-10% (+30%) from the nominal value at maximum and the ones of σ_E ($<E>$) to +15% (+/-2%) from the nominal value at maximum.

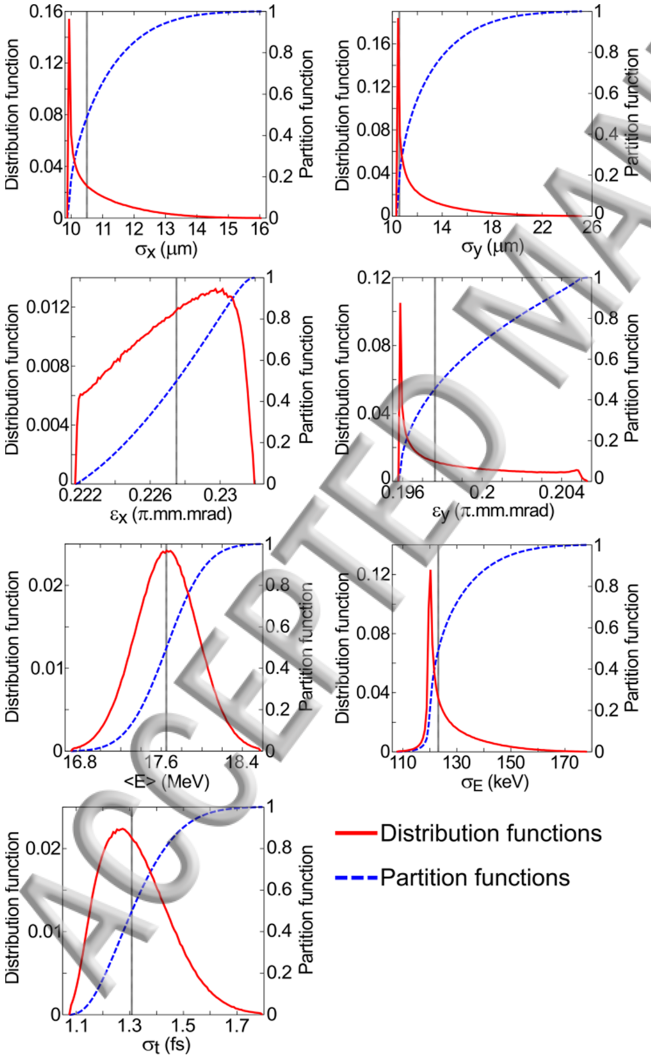

Fig. 25. Distribution and partition functions of the electron bunch properties at the ICS point under the influence of a jitter of E_{ml} with σ_{jit} = 3% around 115 MV/m. The vertical black lines denote the nominal properties obtained with no jitter.

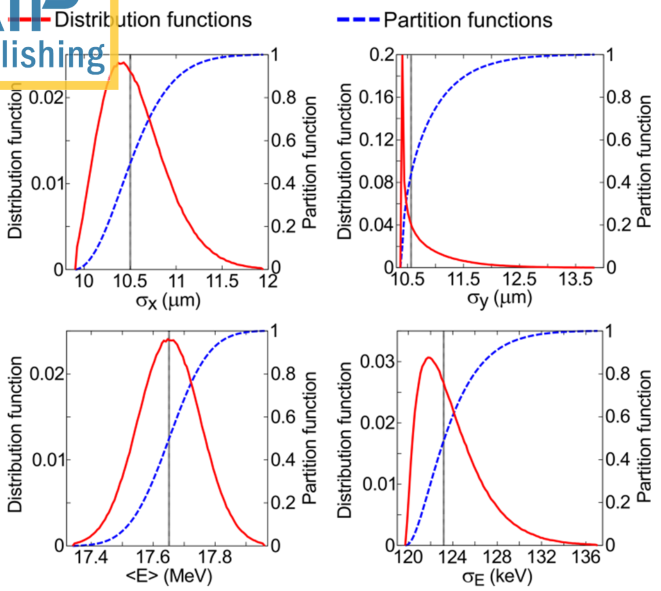

Fig. 26. Distribution and partition functions of σ_x, σ_y, σ_E and <*E*> at the ICS point under the influence of a jitter of E_{ml} with σ_{jit} = 1% around E_{ml} = 115 MV/m. The vertical black lines denote the nominal properties obtained with no jitter.

5.3.3. Jitter of the electron bunch injection phase into the THz linac

The third studied jitter is a jitter of the injection phase φ_0 of the electron bunch into the THz linac. This jitter arises from two main sources. The first one is the internal phase jitter of the source of the THz pulse driving the THz linac. The second one is the jitter of the electron bunch arrival time at the THz linac entrance, which will translate into a jitter of φ_0. In this subsection, we will only consider the jitter of φ_0 due to the source of the THz pulse.

The varying parameter in ASTRA for this jitter is the phase of the accelerating field in the THz linac, also referred to as φ_0, with φ_0 = 0° denoting the optimal value. Fig. 27 shows the results of the parameter scan performed with ASTRA for φ_0 = -15° to +15°. The two Gaussian distributions later considered for the jitter in the present subsection are superimposed on Fig. 27. The bunch charge is not displayed since no charge losses happened in any cases.

Fig. 28 displays the distribution and partition functions of the electron bunch properties at the ICS point for σ_{jit} = 1.08° around the nominal value, corresponding to a timing jitter of 10 fs at *f* = 300 GHz (N_{err} = 2000000). The bunch charge is not displayed since no charge losses happened in any cases. Fig. 28 demonstrates that all the electron bunch properties at the ICS point are affected by a jitter of φ_0, but not all with the same importance.

First, this jitter trivially comes with variations of <*E*> at the ICS point, since E_{ml} remains the same for all the simulated events. The consequences of these variations are the same as the ones explained in Sec. 5.3.2 for a jitter on E_{ml}.

As for the jitter on E_{ml}, the variations of the transverse emittances remain very limited, since ε_x is at maximum 2% higher than the nominal value and ε_y remains within ± 2% of the nominal value. Then, contrary to the case of the jitter on E_{ml}, σ_x and σ_y are only slightly affected by the fact that the nominal settings of the quadrupole triplet become inappropriate, since they are never more than 7% away from the nominal values.

These small variations of σ_x and σ_y at the ICS point unfortunately do not prevent from having strong variations of σ_E, which are even much stronger than for a jitter of E_{ml} since it can increase up to +120% of the nominal value for the most extreme cases, greatly deteriorating the bandwidth of the generated X-ray pulse. These variations of σ_E come from the fact that, as for the case of a jitter on E_{ml}, the parameter ΔZ_{lt}

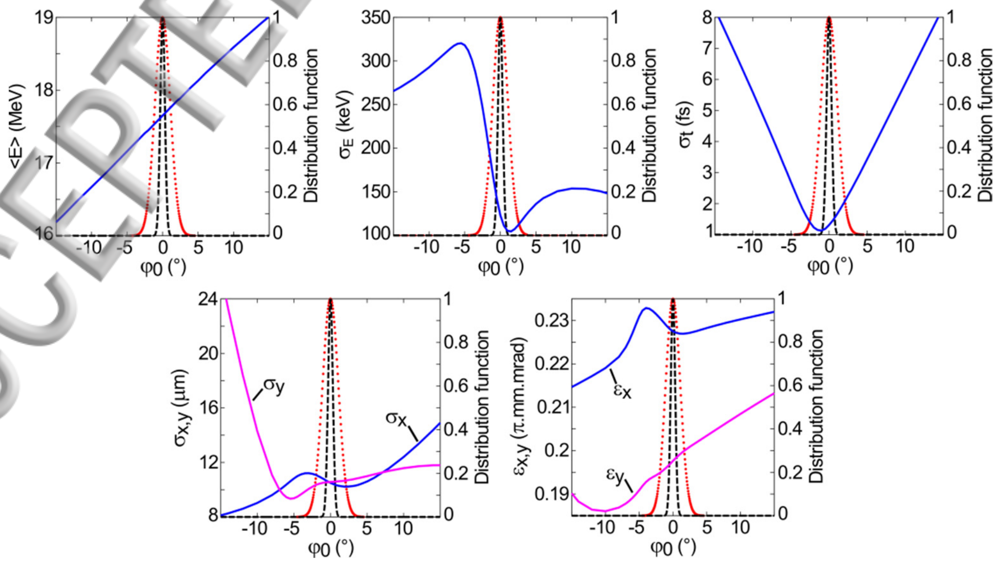

Fig. 27. Electron bunch properties at the ICS point as a function of φ_0 (solid curves). φ_0 = 0° denotes the optimal value. Dotted curves: Distribution function of φ_0 for σ_{jit} = 1.08° (≡ 10 fs timing jitter at *f* = 300 GHz). Dashed curves: Distribution function of φ_0 for σ_{jit} = 0.324° (≡ 3 fs timing jitter at *f* = 300 GHz).

defined in Sec. 3.1.2 shifts from its optimal value when the injection phase in the THz linac changes. This affects the space-charge induced reduction of the correlated energy spread as explained in Secs. 3.1.1 and 3.1.2. However, contrary to the case of a jitter on E_{ml}, this shift of ΔZ_{lt} does not come from a shift of the position of the transverse focal point, which is almost unchanged (≈ 1 mm shift) with the simulated jitter of φ_0. It rather comes from a strong shift (up to several cm) of the position of the longitudinal focal point represented by the parameter Z_{long} defined in Sec. 3.1.2. Note that Z_{long} was almost invariant (≈ 1 mm shift) for the case of a jitter on E_{ml}. The fact that the variations of σ_E are greater than for the case of a jitter on E_{ml} simply comes from the fact that for the assumed values of σ_{jit} the shift of ΔZ_{lt} is bigger for a jitter of φ_0.

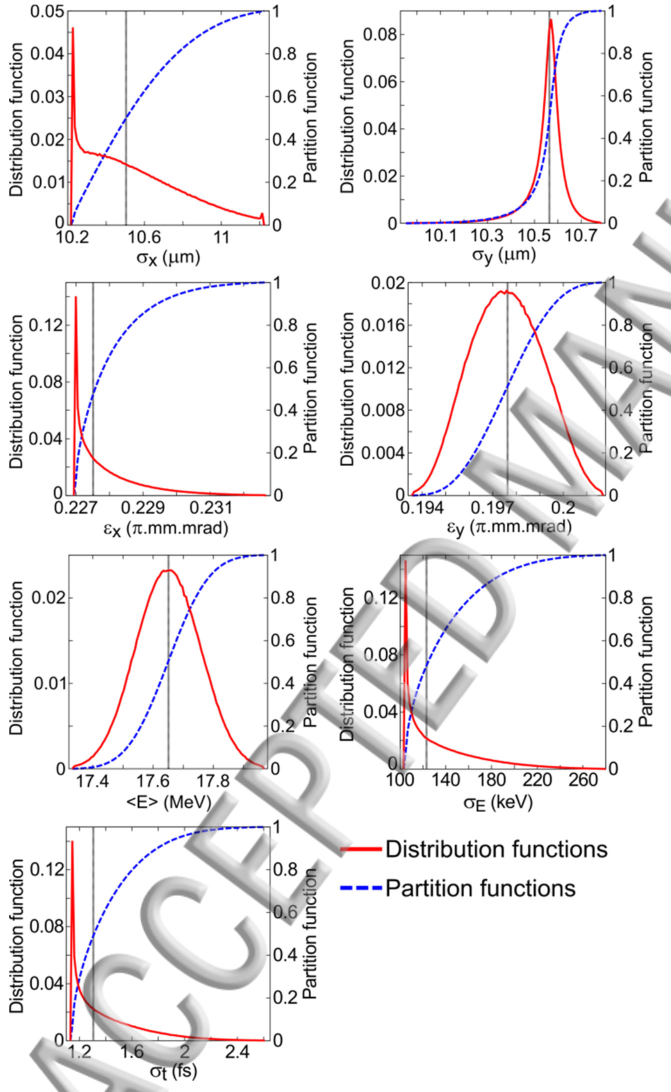

Fig. 28. Distribution and partition functions of the electron bunch properties at the ICS point under the influence of a jitter of φ_0 with σ_{jit} = 1.08° (≡ 10 fs timing jitter at f = 300 GHz) around the nominal value. Vertical black lines: nominal properties obtained with no jitter.

As explained in Sec. 3.1.2 this shift of ΔZ_{lt} also comes with variations of the bunch length at the ICS point, which are visible in Fig. 28. These variations of σ_t are bigger than for the two other studied jitters, since it can be doubled by the assumed jitter of φ_0. However, they are always of the single femtosecond order.

Secs. 5.3.1 and 5.3.2 have demonstrated that the electron bunch properties can be kept under control under the influence of a pointing jitter or of a jitter of E_{ml}, providing that they are not too strong (σ_{jit} < 100 µm for the pointing jitter and $\sigma_{jit} \approx 1\%$ for the jitter of E_{ml}). On the opposite, the present subsection show that this is not the case for σ_t and especially σ_E under the influence of a jitter of φ_0 with the assumed σ_{jit} = 1.08°. It would therefore be of great importance to reduce the achievable value of σ_{jit} to a few tenths of degrees, thus improving the shot-to-shot stability of the bunch longitudinal properties. Fig. 29 shows simulation results for σ_E and σ_t at the ICS point for the smaller jitter σ_{jit} = 0.324° around the nominal value, corresponding to a timing jitter of 3 fs (N_{err} = 2000000). It shows that the variations of σ_E (σ_t) could thus be kept below +30% (+25%) of the nominal value and would start to be reasonable for operation.

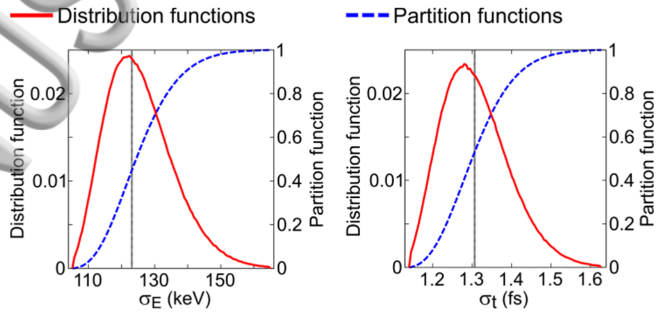

Fig. 29. Distribution and partition functions of σ_E and σ_t at the ICS point under the influence of a jitter of φ_0 with σ_{jit} = 0.324° (≡ 3 fs timing jitter at f = 300 GHz) around the nominal value. The vertical black lines denote the nominal properties obtained with no jitter.

One should not forget that the results presented in this subsection concern only the jitter of φ_0 induced by the internal phase jitter of the source of the THz pulse driving the THz linac. The arrival timing jitter of the electron bunch at the THz linac entrance will also contribute to it and has to be studied in details in future studies. It can arise from several sources. First, a jitter of the amplitude of the accelerating field in the S-band gun implies a change in the bunch energy at the gun exit, which results in a change of the travel time to reach the entrance of the THz linac. Then, a jitter in the transverse position on the cathode of the UV laser pulse driving the gun results, as explained in Ref. 1 and in Sec. 3.2, in a jitter of the bunch travel time from the cathode to the gun exit. Besides, a transverse offset of the bunch implies that the focusing solenoid (see Fig. 2) also has an impact, increasing quadratically with the offset, on the travel time of the bunch up to the THz linac entrance. Eventual jitters of the solenoid magnetic field will in this case also have an impact. Finally a change in the starting time of the bunch, namely a phase jitter between the UV laser pulse driving the gun and the accelerating field in the gun, also generates a bunch arrival time jitter at the THz linac entrance. It is therefore crucial to note that an arrival timing jitter of the electron bunch at the

THz linac entrance will also come with a jitter of all the electron bunch properties at the THz linac entrance. As a result, it cannot be simulated following the simple method exposed at the beginning of Sec. 5.3, but rather with a numerical simulation starting at the photocathode and including simultaneous jitters for the multiple parameters generating the bunch arrival timing jitter at the THz linac entrance. This could for example be done with the ERROR namelist of ASTRA[12].

This arrival timing jitter of the electron bunch at the THz linac entrance is one of the key and challenging technical requirements for the hybrid concept developed in the present paper, because the frequency of the accelerating field being very high even a small jitter of the bunch arrival time could result in a significant dephasing with respect to the THz accelerating field, and therefore a change of the bunch properties at the ICS point. As an example, at f = 300 GHz (f = 150 GHz) a 9.3 fs (18.6 fs) bunch arrival time jitter corresponds to a dephasing of 1° with respect to the accelerating field in the THz linac. An arrival timing jitter around 10 fs is already very low but not impossible to achieve. For example this is the one aimed at the end of the beamline of the ARES linac (after two traveling wave accelerating structures and a magnetic chicane), which is intended to be a test bench for external injection in several types of high-frequency accelerating structures (plasma wakefield, THz and laser-driven dielectric structures)[48,49]. However Figs. 28 and 29, while not applicable for a jitter of φ_0 due to a bunch arrival timing jitter at the THz linac entrance, give the hint that this may not be sufficient for the shot-to-shot stability of the electron bunch properties at the ICS point, especially for σ_E, and that future technical improvements will be of great importance to reduce the achievable arrival timing jitter to a few fs. Considering their inferred importance, the variations of the electron bunch properties at the ICS point under the influence of an arrival timing jitter at the THz linac entrance will be the object of a future detailed study.

5.3.4. Arrival time jitter at the ICS point

The three studied jitters in Sec. 5.3, in addition to the presented variations of the electron bunch properties at the ICS point, also induce a jitter of the electron bunch arrival time at the ICS point. This is explained by the fact that <E> and in some case the electron bunch trajectory changes, resulting in a change of the electron bunch travel time up to the ICS point. This results in a not optimal time overlap with the laser driving the ICS, which leads to a decrease of the laser energy effectively interacting with the electron bunch and therefore a decrease of the number of generated X-ray photons. The purpose of this subsection is to give a first estimate of this effect.

To do that, we simulate only the reference particle in ASTRA over the parameter ranges assumed for the three jitters, and we each time record its travel time up to the intended ICS point. Fig. 30 shows the results of these simulations, as the difference compared to the travel time for the nominal cases, and also displays the distribution function assumed for the studied jitters.

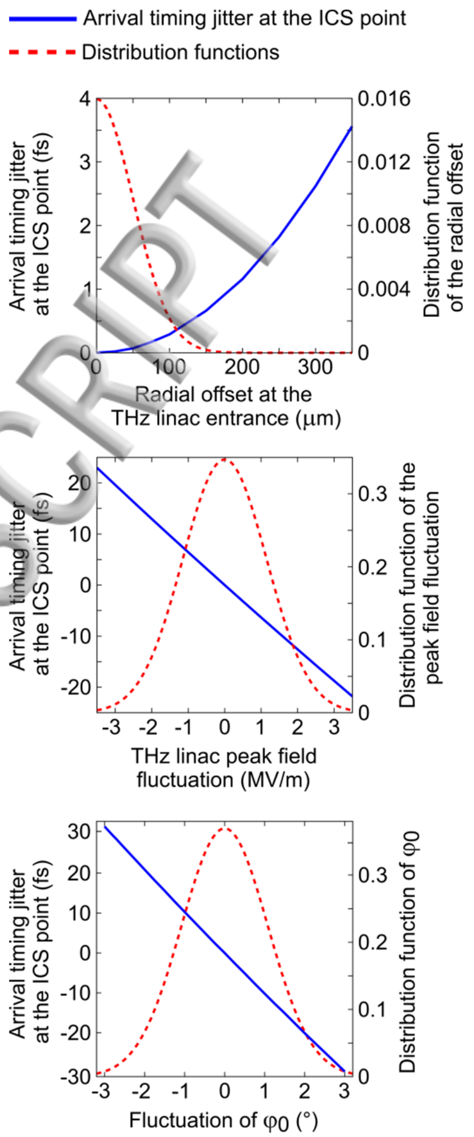

Fig. 30. Arrival time jitter of the electron bunch at the ICS point for the three jitters studied in Sec. 5.3. Pointing jitter at the THz linac entrance (top): σ_{jit} = 50 µm; Jitter of E_{ml} (middle): σ_{jit} = 1%; Jitter of φ_0 (bottom): σ_{jit} = 1.08°.

The first observation one can made on Fig. 30 (top) is that the contribution of the pointing jitter at the THz linac entrance to the bunch arrival timing jitter at the ICS point is of the order of a few fs at maximum, making it therefore negligible.

The two significant and comparable contributions to the bunch arrival timing jitter at the ICS point shown in Fig. 30 are therefore the ones of a jitter on E_{ml} (up to $\pm$ 20 fs if σ_{jit} = 1%) and of a jitter on φ_0 (up to $\pm$ 30 fs if σ_{jit} = 1.08°). However, even if the maximal arrival time jitters of 20 and 30 fs are quadratically added, resulting in an arrival time jitter of 36 fs, this corresponds to only 3.6% of the rms length of 1 ps we assumed for the laser pulse driving the ICS. As a result, the impact on the time overlap of the electron bunch with the laser pulse, and therefore on the number of generated photons, will remain limited.

In conclusion, it can be said that none of the jitters we studied up to now will have a significant impact on the time overlap between the electron bunch and the laser pulse driving the ICS.

6. Conclusions and prospects

In this paper, we have presented the optimization of a concept of hybrid and compact ultrafast (single fs to sub-fs) X-ray pulse source based on RF and THz technologies (see Figs. 1 and 2).

We first demonstrated through ASTRA beam dynamics simulations that the electron bunch energy spread at the ICS point σ_E, and subsequently the bandwidth of the generated X-ray pulse, can be greatly reduced by the strong space-charge forces experienced by the bunch in the vicinity of the ICS point (see Fig. 3). We determined how this reduction of σ_E can be optimized through proper choices of the position of the electron bunch transverse focal point (see Figs. 4 and 5) and of the electron bunch transverse size at the THz linac entrance (see Fig. 6).

We then study the influence of the transverse shape of the UV laser pulse driving the gun, using various profiles (see Figs. 7 and 8). We demonstrated that for the low bunch charge regime we are considering, a Gaussian cut at 1σ transverse profile delivers much better electron bunch properties than a pure Gaussian (see Figs 9 to 12) and equivalent properties compared to the radial and uniformly filled ellipsoid transverse profiles (see Table 1). We retained the Gaussian cut at 1σ due to its technical simplicity.

Finally, the importance of a fine-tuning of the phase velocity of the THz pulse driving the linac has been highlighted. We demonstrated that at f = 150 GHz a value slightly higher than c comes with a significant reduction of σ_E (see Table 2 and Fig. 15), due to the optimization of the electron bunch phase slippage in the THz linac (see Fig. 14).

Following these optimization schemes, we derived several working points for the electron bunch properties at the ICS point for the two THz linac frequencies f = 150 GHz (see Table 4) and f = 300 GHz (see Table 3), with final kinetic energies close to respectively 15 MeV and 18 MeV. From the lowest simulated charge (Q = 100 fC) to the highest one (Q = 5 pC), the simulated electron bunch properties at the ICS point are in the following ranges: $\sigma_E = 0.1 – 2.6\%$, $\sigma_t = 0.4 – 5$ fs, $\sigma_{x,y} = 5 – 13$ µm, $\varepsilon_x = 0.11 – 0.53$ π.mm.mrad and $\varepsilon_y = 0.11 – 0.35$ π.mm.mrad. We also demonstrated that each individual working point is tunable through the strength of the final transverse and longitudinal focusing experienced by the electron bunch (see Table 5). Namely, a stronger (weaker) focusing will decrease $\sigma_{x,y}$ and σ_t (σ_E) but increase σ_E ($\sigma_{x,y}$ and σ_t).

The properties of the X-ray pulse generated via ICS have also been investigated with CAIN simulations (see Table 6). We showed that a tunability of the ultrafast X-ray source could be achieved thanks to the possibility to switch between two different DLW corresponding to f = 150 GHz and f = 300 GHz, and by the possibility to switch between the first and second harmonics of an IR laser with a wavelength around 1 µm to drive the ICS. The simulations we conducted (see Fig. 20) predict in the range between 2.9 keV and 11.5 keV, for a laser pulse energy of 400 mJ, a number of photons per pulse between $1.5*10^4$ and $7.7*10^4$ in 1.5% rms bandwidth or between $6.2*10^3$ and $3.5*10^4$ with lower bandwidths (between 0.56% and 1.5% rms along the energy range). They also showed that the X-ray photon energy spectra present a long low energy tail (see Fig. 17), meaning that a filtering of the X-ray would allow to significantly reduce the bandwidth of the pulse without reducing too much the number of photons (see Fig. 18).

Finally, several technical requirements for the concept have been investigated, determined and discussed. The properties of the DLW and of the THz pulse driving it required for the cases presented in this paper are given (see Table 7), resulting in the conclusions that further developments and studies are needed to have a source compatible with a compact layout (namely laser or gyrotron based) but that beam-driven wakefields generated in DLW by electron bunches provided by conventional RF accelerators could be of great interest to produce enough THz power for performing demonstration experiments. The influence of several jitters on the stability of the achievable electron bunch properties at the ICS point was also studied. A pointing jitter of the bunch at the entrance of the THz linac has been shown to only strongly affect σ_E (see Fig. 22) and a value of 50 µm rms for this jitter (≡ 10% of the vacuum radius of the DLW at f = 300 GHz) has been demonstrated as acceptable (see Fig. 23). A jitter of the amplitude of the accelerating field in the THz linac has been found to be more problematic, since it can strongly affect $<E>$, σ_E, σ_x and especially σ_y (see Fig. 25). A value of 1% rms for this jitter starts to be reasonable for the shot-to-shot stability of the electron bunch properties, but still not totally satisfactory for σ_y (see Fig. 26). The most demanding of the studied jitters is the jitter of the injection phase of the bunch into the THz linac. In fact, it has been demonstrated that a contribution of 1° to this jitter coming from the internal phase jitter of the source of the THz pulse driving the linac already leads to strong shot-to-shot variations of σ_t and especially σ_E at the ICS point (see Fig. 28). We showed that a reduction of this contribution to a few tenths of degrees starts to be reasonable for the shot-to-shot stability of σ_E at the ICS point (see Fig. 29). In addition to that, a second contribution to the jitter of the bunch injection phase into the THz linac has been approached but not studied into details in this paper, namely the bunch arrival timing jitter at the THz linac entrance. This contribution is expected to be of major importance because at f = 300 GHz a 10 fs arrival timing jitter at the THz linac entrance, which is the value aimed on the SINBAD facility at DESY[49], already translates into a 1° jitter of the bunch injection phase into the THz linac. Improvements reducing this arrival timing jitter at the THz linac entrance to a few femtoseconds would therefore greatly help stabilizing the operation of a potential future machine based on the concept presented in this paper. Finally, it has been verified that none of the jitters studied up to now will have a significant impact on the time overlap between the electron bunch and the laser at the ICS point (see Fig. 30).

In addition to the further optimization of the working points presented in this paper, especially on the ICS point of view, the work will continue on several aspects. The compactness of the hybrid concept presented in this paper (see Fig. 2) represents a challenge for the implementation of the electron beam diagnostics in the beamline, for which the study is just in the preliminary phase and not discussed in this paper. This will therefore be studied in more details and the distances in the layout presented in Fig. 2 might have to be adjusted according to the number and sizes of the required diagnostics. The study on the influence of the jitters susceptible to appear in experiments will be pursued with the aim to more clearly define what the acceptable values are. Especially, the influence of a bunch arrival timing jitter at the THz linac entrance, expected to be significant and just introduced in this paper, will make the object of a future detailed study. The different types of THz sources mentioned in Sec. 5.2 will also be investigated in more details and not only on the aspect of the power delivered, especially the shot-to-shot phase stability will be closely looked at, to determine which one would be the most suited. An experiment is currently in preparation by the authors in order to demonstrate the acceleration around the 1 MeV level of an electron bunch delivered by an S-band gun in a DLW driven by a laser-generated THz pulse. Another experiment is also in preparation to develop a longitudinal diagnostics with sub-fs resolution, which is necessary for the concept presented in this paper, based on a THz-driven DLW used as transverse deflecting structure[17]. Also, the possibilities of applications, other than an ICS source, based on the hybrid layout proposed in this paper will also be investigated, especially: direct ultrafast imaging with the electron bunch, use as injector for other advanced acceleration schemes (plasma, Dielectric-laser acceleration, etc.).

Finally, one should note that the study presented in this paper considers only single electron bunches (X-ray pulses) and do not tackle the important point of the repetition rate of the source. This one is of particular importance for an X-ray source based on ICS because the number of photons per shot remains limited due to the low cross-section of the ICS process, in our concept between 10^4 and 10^5 photons/pulse. An important future study will therefore be to determine what could be the repetition rate, and therefore the X-ray flux, of the concept we are proposing. This repetition rate will be mainly determined by the one that the S-band gun could deliver and by the one achievable by the THz pulse source.

Funding

This work has been supported by the European Research Council under the European Union's Seventh Framework Programme (FP/2007-2013)/ERC Grant Agreement n. 609920.

Acknowledgments

The authors would like to thank K. Flöttmann and all the colleagues of the AXSIS collaboration for fruitful discussions.

References

[1] T. Vinatier, R. W. Assmann, U. Dorda, F. Lemery and B. Marchetti, Nucl. Instrum. Methods Phys. Res. A **909**, 185 (2018).

[2] D. T. Palmer, "The Next Generation Photoinjector", Ph.D. dissertation (Stanford University, California, USA, 1998).

[3] D. H. Dowell, E. Jongewaard, C. Limborg-Deprey, J. Schmerge, Z. Li, L. Xiao, J. Wang, J. Lewandowski and A. Vlieks, "Results of the SLAC LCLS gun high-power RF tests", *in Proceedings Part. Accel. Conf. 2007 (PAC'07), Albuquerque, New Mexico, USA,* TUPMS047, 1296 (2007).

[4] F. X. Kärtner, F. Ahr, A. -L. Calendron, H. Çankaya, S. Carbajo, G. Chang, G. Cirmi, K. Dörner, U. Dorda, A. Fallahi, A. Hartin, M. Hemmer, R. Hobbs, Y. Hua, W. R. Huang, R. Letrun, N. Matlis, V. Mazalova, O. D. Mücke, E. Nanni, W. Putnam, K. Ravi, F. Reichert, I. Sarrou, X. Wu, A. Yahagi, H. Ye, L. Zapata, D. Zhang, C. Zhou, R. J. D. Miller, K. K. Berggren, H. Graafsma, A. Meents, R. W. Assmann, H. N. Chapman and P. Fromme, Nucl. Instrum. Methods Phys. Res. A **829**, 24 (2016).

[5] G. Vashchenko, R. W. Assmann, U. Dorda, K. Galaydych, B. Marchetti, T. Vinatier, M. Fakhari, A. Fallahi, F. X. Kärtner, N. H. Matlis, W. Qiao and C. Zhou, "Characterization of the electron beam from the THz driven gun for AXSIS", *in Proceedings 8th Int. Part. Accel. Conf. (IPAC'17), Copenhagen, Denmark,* MOPIK006, 509 (2017).

[6] C. Zhou, F. Ahr, A. –L. Calendron, H. Cankaya, M. Fakhari, A. Fallahi, F. X. Kärtner, N. H. Matlis, W. Qiao, X. Wu, D. Zhang, R. W. Assmann, U. Dorda, K. Galaydych, B. Marchetti, G. Vashchenko and T. Vinatier, "Electron acceleration with a ultrafast gun driven by single-cycle terahertz pulses", *in Proceedings 8th Int. Part. Accel. Conf. (IPAC'17), Copenhagen, Denmark,* TUPAB038, 1406 (2017).

[7] G. Vashchenko, R. Assmann, U. Dorda, M. Fakhari, A. Fallahi, K. Galaydych, F. Kärtner, B. Marchetti, N. Matlis, T. Vinatier, W. Qiao and C. Zhou, Nucl. Instrum. Methods Phys. Res. A **909**, 177 (2018).

[8] S. Frankel, J. Appl. Phys. **18**, 650 (1947).

[9] C. T. M. Chang and J. W. Dawson, J. Appl. Phys. **41**, 4493 (1970).

[10] M. Kreh, "The Bessel functions", in Lecture Notes, Penn State-Goettingen Summer School on Number Theory, vol. 82, 2012.

[11] P. Zou, "X-Band Dielectric-Loaded RF Driven Accelerator Structures: Theoretical and Experimental Investigations", Ph. D. dissertation (Illinois Institute of Technology, Chicago, USA, 2001).

[12] K. Flöttmann, "ASTRA manual", Deutsches Elektronen Synchrotron, Hamburg, Germany, 2017.

[13] D. H. Dowell and J. F. Schmerge, Phys. Rev. ST-Accel. Beams **12**, 074201 (2009).

[14] S. G. Anderson, P. Musumeci, J. B. Rosenzweig, W. J. Brown, R. J. England, M. Ferrario, J. S. Jacob, M. C. Thompson, G. Travish, A. M. Tremaine and R. Yoder, Phys. Rev. ST-Accel. Beams **8**, 014401 (2005).

[15] V. Pal, C. Tradonsky, R. Chriki, N. Kaplan, A. Brodsky, M. Attia, N. Davidson and A. A. Friesem, Appl. Opt. **57**:16, 4583 (2018).

[16] K. Galaydych, R. Assmann, U. Dorda, B. Marchetti, G. Vashchenko, I. Zagorodnov, Nucl. Instrum. Methods Phys. Res. A **909**, 181 (2018).

[17] F. Lemery, R. Assmann, K. Flöttmann and T. Vinatier, "A transverse deflection structure with dielectric-lined waveguides in the sub-THz regime", *in Proceedings 8th Int. Part. Accel. Conf. (IPAC'17), Copenhagen, Denmark,* MOPAB052, 215 (2017).

[18] T. Vinatier, R. W. Assmann, U. Dorda, F. Lemery and B. Marchetti, J. Phys. Conf. Ser. **874**, 012042 (2017).

[19]K. Yokoya, "CAIN 2.42 manual", KEK, Japan, 2011.

[20]G. R. Blumenthal and R. J. Gould, Rev. Modern Phys. **42**, 237 (1970).

[21]I. V. Pogorelsky, I. Ben-Zvi, T. Hirose, S. Kashiwagi, V. Yakimenko, K. Kusche, P. Siddons, J. Skaritka, T. Kumita, A. Tsunemi, T. Omori, J. Urakawa, M. Washio, K. Yokoya, T. Okugi, Y. Liu, P. He and D. Cline, Phys. Rev. ST-Accel. Beams **3**, 090702 (2000).

[22]V. Petrillo, A. Bacci, R. Ben Alì Zinati, I. Chaikovska, C. Curatolo, M. Ferrario, C. Maroli, C. Ronsivalle, A. R. Rossi, L. Serafini, P. Tomassini, C. Vaccarezza and A. Variola, Nucl. Instrum. Methods Phys. Res. A **693**, 109 (2012).

[23]A. Bacci, D. Alesini, P. Antici, M. Bellaveglia, R. Boni, E. Chiadroni, A. Cianchi, C. Curatolo, G. Di Pirro, A. Esposito, M. Ferrario, A. Gallo, G. Gatti, A. Ghigo, M. Migliorati, A. Mostacci, L. Palumbo, V. Petrillo, R. Pompili, C. Ronsivalle, A. R. Rossi, L. Serafini, B. Spataro, P. Tomassini and C. Vaccarezza, J. Appl. Phys. **113**, 194508 (2013).

[24]P. Tomassini, A. Giulietti, D. Giulietti and L. A. Gizzi, Appl. Phys. B: Lasers Opt. **80**, 419 (2005).

[25]H. Kiriyama, F. Nakano and K. Yamakawa, Journal of the Optical Society of America B **19**:8, 1857 (2002).

[26]E. A. Nanni, W. R. Huang, K. –H. Hong, K. Ravi, A. Fallahi, G. Moriena, R. J. D. Miller and F. X. Kärtner, Nature Commun. **6**, 8486 (2015).

[27]S. W. Jolly, N. H. Matlis, F. Ahr, V. Leroux, T. Eichner, A. –L. Calendron, H. Ishizuki, T. Taira, F. X. Kärtner and A. R. Maier, "Millijoule-scale narrowband terahertz pulses via phase manipulation of pump laser pulses", arxiv:1802.02508 (2018).

[28]K. Ravi, D. Barre and F. X. Kärtner, Opt. Express **24**, 25582 (2016).

[29]G. Tóth, P. S. Nugraha, G. Krizsán, M. I. Mechler, G. Polónyi, J. Hebling and J. A. Fülop, "Efficient semiconductor source of multicycle terahertz pulses using intensity modulated pump", *in Conference on Lasers and Electro-Optics*, jTh2A, 191 (OSA Technical Digest, 2018).

[30]K. Ravi, M. Hemmer, G. Cirmi, F. Reichert, D. N. Schimpf, O. D. Mücke and F. X. Kärtner, Opt. Lett. **41** (16), 3806 (2016).

[31]V. A. Flyagin, A. V. Gaponov, M. I. Petelin and V. K. Yulpatov, IEEE Transactions on Microwave Theory and Techniques **25**:6, 514 (1977).

[32]D. S. Tax, B. Y. Rock, B. J. Fox, S. K. Jawla, S. C. Schaub, M. A. Shapiro, R. J. Temkin and R. J. Vernon, IEEE Transactions on Plasma Science **42**:5, 1128 (2014).

[33]H. Jory, M. Blank, P. Borchard, P. Cahalan, S. Cauffman, T. S. Chu and K. Felch, AIP conference proceedings **691**, 224 (2003).

[34]S. Ruess, K. A. Avramidis, G. Gantenbein, Z. Ioannidis, S. Illy, P. C. Kalaria, T. Kobarg, I. G. Pagonakis, T. Ruess, T. Rzesnicki, M. Thumm, J. Weggen and J. Jelonnek, "KIT in-house manufacturing and first operation of a 170 GHz 2 MW longer pulse coaxial cavity pre-prototype gyrotron", *in 11th German Microwave Conference (GeMiC)*, 291 (2018).

[35]K. Sakamoto, R. Ikeda, T. Kariya, Y. Oda, T. Kobayashi, K. Kajiwara, K. Hayashi, R. Minami, K. Takahashi, T. Imai and S. Moriyama, "Study of high power and high frequency gyrotron for fusion reactor", *in Proceedings 42nd Int. Conf. on Infrared, Millimeter and Terahertz Waves (IRMMW-THz)*, 1 (2017).

[36]T. L. Grimm, K. E. Kreischer and R. J. Temkin, Physics of Fluids B: Plasma Physics **5**, 4135 (1993).

[37]E. L. Saldin, E. A. Schneidmiller and M. V. Yurkov, Nucl. Instrum. Methods Phys. Res. A **398**, 373 (1997).

[38]D. A. G. Deacon, L. R. Elias, J. M. J. Madey, G. J. Ramian, H. A. Schwettman and T. I. Smith, Phys. Rev. Lett. **38**:16, 892 (1977).

[39]M. Gensch, B. Green, S. Kovalev, M. Kuntzsch, J. Hauser, R. Schurig, U. Lehnert, P. Michel, A. Al-Shemmary, V. Asgekar, T. Golz, S. Vilcins, H. Schlarb, N. Stojanovic, A. S. Fisher, M. Schwarz, A. –S. Mueller, N. Neumann, D. Plettemeier and G. A. Geloni, "THz facility at ELBE: A versatile test facility for electron bunch diagnostics on quasi-CW electron beams", *in Proceedings 5th Int. Part. Acc. Conf. (IPAC'14), Dresden, Germany*, TUZA02, 933 (2014).

[40]P. Boonpornprasert, M. Krasilnikov and F. Stephan, "Calculations for a THz SASE FEL based on the measured electron beam parameters at PITZ", *in Proceedings 38th Int. Free Electron Laser Conf. (FEL2017), Santa Fe, New Mexico, USA*, WEP004, 411 (2017).

[41]W. Gai, P. Schoessow, B. Cole, R. Konecny, J. Norem, J. Rosenzweig and J. Simpson, Phys. Rev. Lett. **61**, 2756 (1988).

[42]G. Andonian, D. Stratakis, M. Babzien, S. Barber, M. Fedurin, E. Hemsing, K. Kusche, P. Muggli, B. O'Shea, X. Wei, O. Williams, V. Yakimenko and J. B. Rosenzweig, Phys. Rev. Lett. **108**, 244801 (2012).

[43]B. D. O'Shea, G. Andonian, S. K. Barber, K. L. Fitzmorris, S. Hakimi, J. Harrison, P. D. Hoang, M. J. Hogan, B. Naranjo, O. B. Williams, V. Yakimenko and J. B. Rosenzweig, Nature Commun. **7**, 12763 (2016).

[44]S. Antipov, M. Babzien, C. Jing, M. Fedurin, W. Gai, A. Kanareykin, K. Kusche, V. Yakimenko and A. Zholents, Phys. Rev. Lett. **111**, 134802 (2013).

[45]S. Antipov, S. V. Baryshev, R. Kostin, S. Baturin, J. Qiu, C. Jing, C. Swinson, M. Fedurin and D. Wang, Appl. Phys. Lett. **109**:14, 142901 (2016).

[46]E. Curry, S. Fabbri, J. Maxson, P. Musumeci and A. Gover, Phys. Rev. Lett. **120**, 094801 (2018).

[47]S. S. Dhillon, M. S. Vitiello, E. H. Linfield, A. G. Davies, M. C. Hoffmann, J. Booske, C. Paoloni, M. Gensch, P. Weightman, G. P. Williams, E. Castro-Camus, D. R. S. Cumming, F. Simoens, I. Escorcia-Carranza, J. Grant, S. Lucyszyn, M. Kuwata-Gonokami, K. Konishi, M. Koch, C. A. Schmuttenmaer, T. L. Cocker, R. Huber, A. G. Markelz, Z. D. Taylor, V. P. Wallace, J. A. Zeitler, J. Sibik, T. M. Korter, B. Ellison, S. Rea, P. Goldsmith, K. B. Cooper, R. Appleby, D. Pardo, P. G. Huggard, V. Krozer, H. Shams, M. Fice, C. Renaud, A. Seeds, A. Stöhr, M. Naftaly, N. Ridler, R. Clarke, J. E. Cunningham and M. B. Johnston, Journal of Physics D: Applied Physics **50**, 043001 (2017).

[48]U. Dorda, B. Marchetti, J. Zhu, F. Mayet, W. Kuropka, T. Vinatier, G. Vashchenko, K. Galaydych, P. A. Walker, D. Marx, R. Brinkmann, R. Assmann, N. H. Matlis, A. Fallahi and F. X. Kaertner, Nucl. Instrum. Methods Phys. Res. A **909**, 239 (2018).

[49]B. Marchetti, R. Assmann, C. Behrens, R. Brinkmann, U. Dorda, K. Floettmann, I. Hartl, M. Huening, Y. Nie, H. Schlarb and J. Zhu, Nucl. Instrum. Methods Phys. Res. A **829**, 278 (2016).

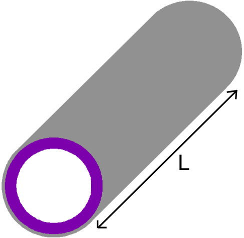
L

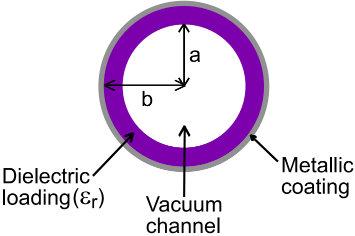
a
b
Dielectric loading(ε_r)
Vacuum channel
Metallic coating

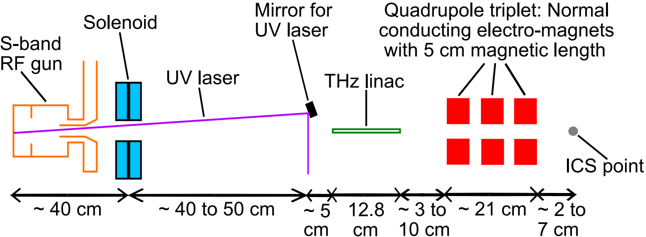
Mirror for UV laser
Quadrupole triplet: Normal conducting electro-magnets with 5 cm magnetic length
Solenoid
S-band RF gun
UV laser
THz linac
ICS point
~ 40 cm
~ 40 to 50 cm
~ 5 cm
12.8 cm
~ 3 to 10 cm
~ 21 cm
~ 2 to 7 cm

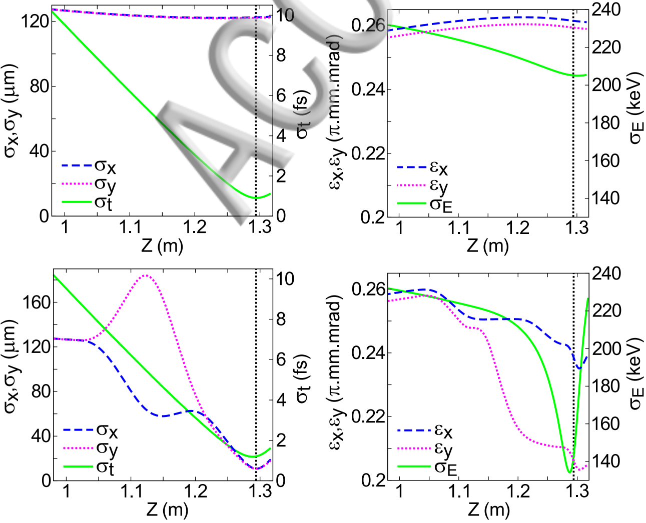
σx,σy (μm)
σt (fs)
Z (m)
σx
σy
σt
εx,εy (π.mm.mrad)
σE (keV)
εx
εy
σE
0
40
80
120
160
0
2
4
6
8
10
1
1.1
1.2
1.3
0.2
0.22
0.24
0.26
140
160
180
200
220
240

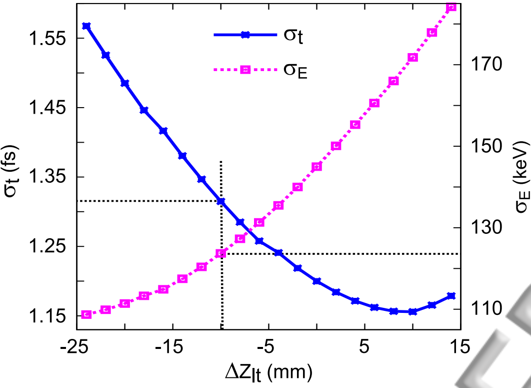
σt
σE
σt (fs)
σE (keV)
1.55
1.45
1.35
1.25
1.15
170
150
130
110
-25
-15
-5
5
15
ΔZlt (mm)

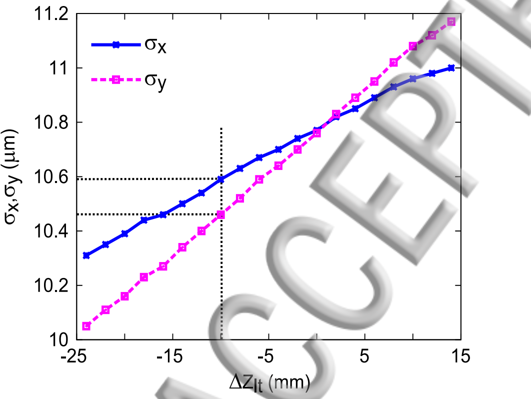
σx
σy
σx,σy (µm)
11.2
11
10.8
10.6
10.4
10.2
10
-25
-15
-5
5
15
ΔZlt (mm)

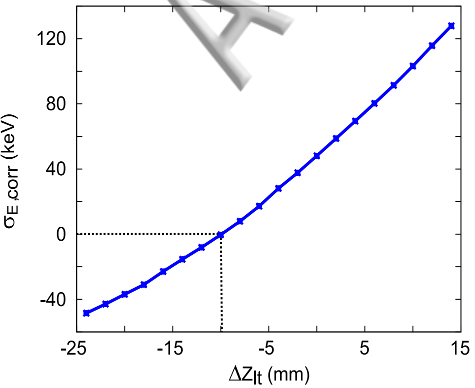
σE,corr (keV)
120
80
40
0
-40
-25
-15
-5
5
15
ΔZlt (mm)

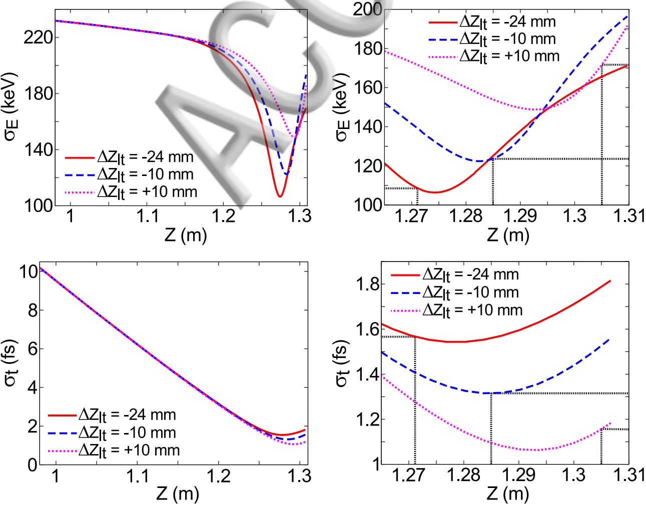

σ_E (keV)
220
180
140
100
1
1.1
1.2
1.3
Z (m)
ΔZ_{lt} = -24 mm
ΔZ_{lt} = -10 mm
ΔZ_{lt} = +10 mm
200
180
160
140
120
100
1.27
1.28
1.29
1.3
1.31
σ_t (fs)
10
8
6
4
2
0
1.8
1.6
1.4
1.2
1

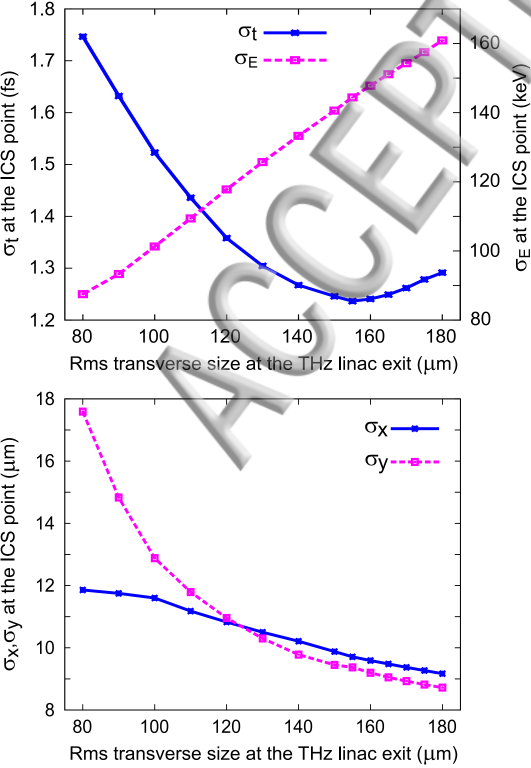
σt
σE
1.8
1.7
1.6
1.5
1.4
1.3
1.2
σt at the ICS point (fs)
160
140
120
100
80
σE at the ICS point (keV)
80
100
120
140
160
180
Rms transverse size at the THz linac exit (μm)
σx
σy
18
16
14
12
10
8
σx,σy at the ICS point (μm)
80
100
120
140
160
180
Rms transverse size at the THz linac exit (μm)

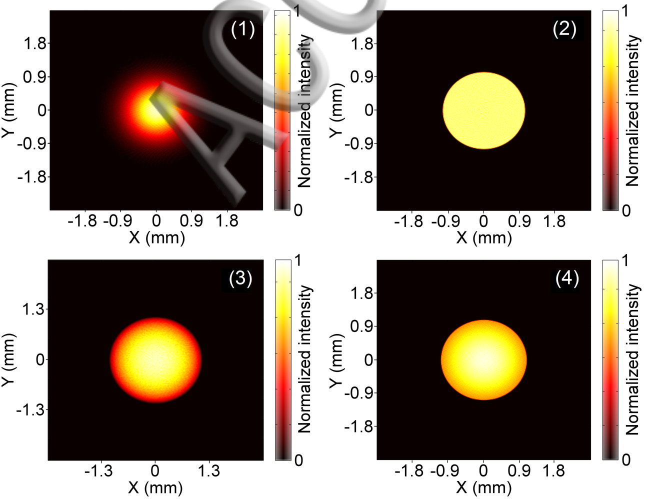
(1)
(2)
(3)
(4)
Y (mm)
X (mm)
1.8
0.9
0
-0.9
-1.8
1.3
-1.3
Normalized intensity
1
0

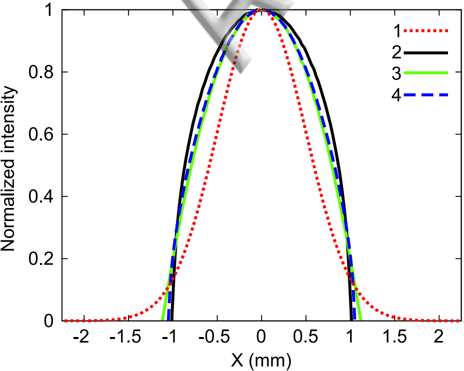
1
2
3
4
Normalized intensity
0
0.2
0.4
0.6
0.8
1
-2
-1.5
-1
-0.5
0
0.5
1
1.5
2
X (mm)

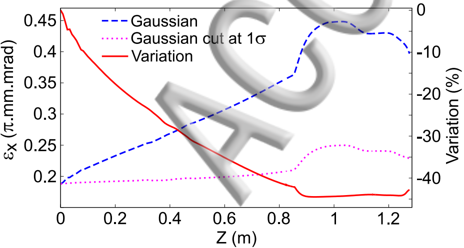

Gaussian
Gaussian cut at 1σ
Variation
εx (π.mm.mrad)
0.45
0.4
0.35
0.3
0.25
0.2
0
0.2
0.4
0.6
0.8
1
1.2
Z (m)
Variation (%)
0
-10
-20
-30
-40

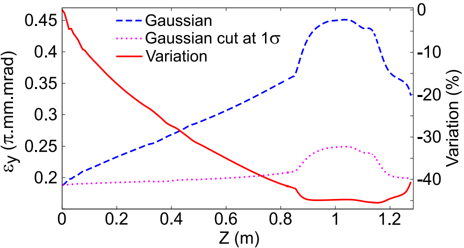

Gaussian
Gaussian cut at 1σ
Variation
εy (π.mm.mrad)
0.45
0.4
0.35
0.3
0.25
0.2
0
0.2
0.4
0.6
0.8
1
1.2
Z (m)
Variation (%)
0
-10
-20
-30
-40

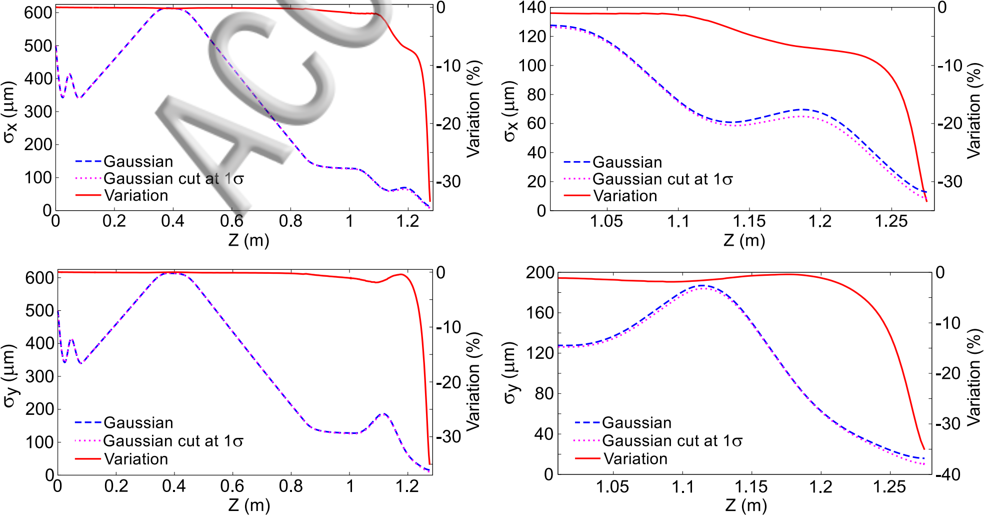
600
500
400
300
200
100
0
σ_x (µm)
0
-10
-20
-30
Variation (%)
0
0.2
0.4
0.6
0.8
1
1.2
Z (m)
Gaussian
Gaussian cut at 1σ
Variation
140
120
100
80
60
40
20
0
σ_x (µm)
0
-10
-20
-30
Variation (%)
1.05
1.1
1.15
1.2
1.25
Z (m)
Gaussian
Gaussian cut at 1σ
Variation
600
500
400
300
200
100
0
σ_y (µm)
0
-10
-20
-30
Variation (%)
0
0.2
0.4
0.6
0.8
1
1.2
Z (m)
Gaussian
Gaussian cut at 1σ
Variation
200
160
120
80
40
0
σ_y (µm)
0
-10
-20
-30
-40
Variation (%)
1.05
1.1
1.15
1.2
1.25
Z (m)
Gaussian
Gaussian cut at 1σ
Variation

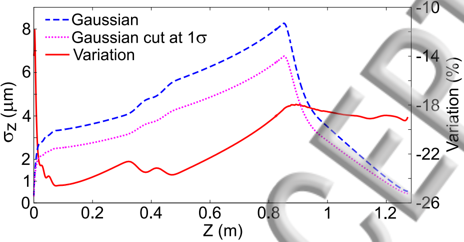
Gaussian
Gaussian cut at 1σ
Variation
σz (µm)
0
1
2
4
6
8
Variation (%)
-10
-14
-18
-22
-26
Z (m)
0
0.2
0.4
0.6
0.8
1
1.2

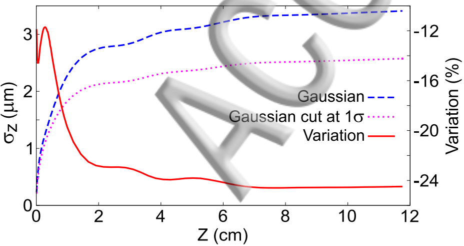
Gaussian
Gaussian cut at 1σ
Variation
σz (µm)
0
1
2
3
Variation (%)
-12
-16
-20
-24
Z (cm)
0
2
4
6
8
10
12

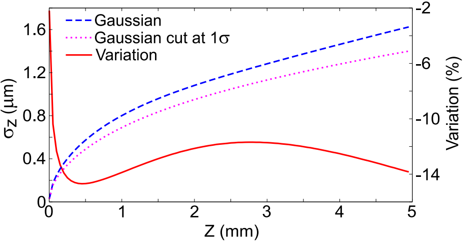
Gaussian
Gaussian cut at 1σ
Variation
σz (µm)
0
0.4
0.8
1.2
1.6
Variation (%)
-2
-6
-10
-14
Z (mm)
0
1
2
3
4
5

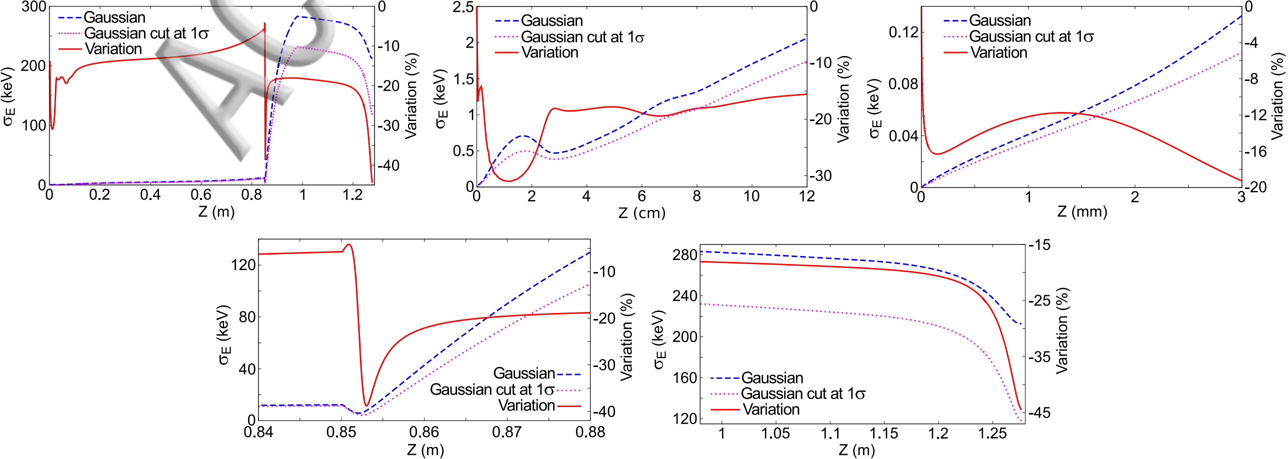
Gaussian
Gaussian cut at 1σ
Variation
σ_E (keV)
Variation (%)
Z (m)
Z (cm)
Z (mm)
300
200
100
0
0
-10
-20
-30
-40
0.2
0.4
0.6
0.8
1
1.2
2.5
2
1.5
1
0.5
4
6
8
10
12
0.12
0.08
0.04
-4
-8
-12
-16
-20
3
120
80
40
0.84
0.85
0.86
0.87
0.88
280
240
200
160
-15
-25
-35
-45
1.05
1.1
1.15
1.2
1.25

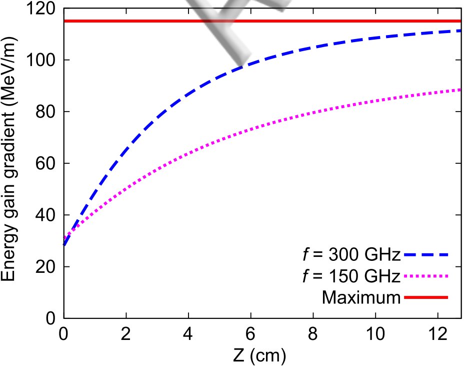
Energy gain gradient (MeV/m)
Z (cm)
0
20
40
60
80
100
120
0
2
4
6
8
10
12
f = 300 GHz
f = 150 GHz
Maximum

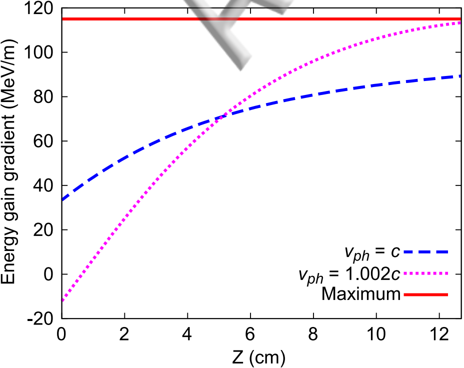
Energy gain gradient (MeV/m)
120
100
80
60
40
20
0
-20
Z (cm)
0
2
4
6
8
10
12
$v_{ph} = c$
$v_{ph} = 1.002c$
Maximum

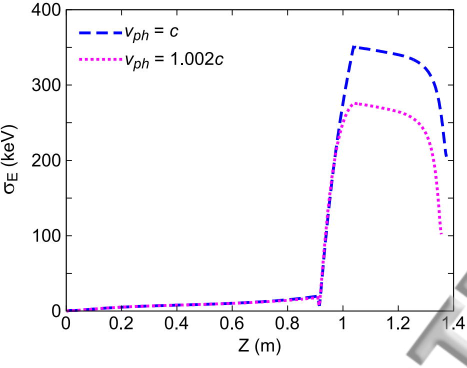
$v_{ph} = c$
$v_{ph} = 1.002c$
σ_E (keV)
400
300
200
100
0
0
0.2
0.4
0.6
0.8
1
1.2
1.4
Z (m)

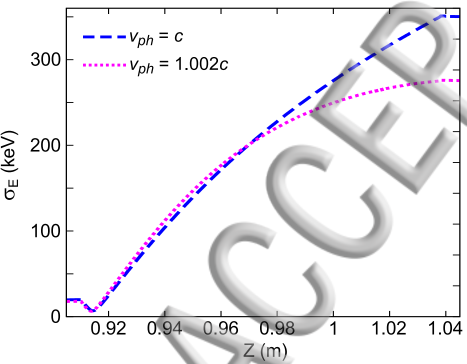
$v_{ph} = c$
$v_{ph} = 1.002c$
σ_E (keV)
300
200
100
0
0.92
0.94
0.96
0.98
1
1.02
1.04
Z (m)

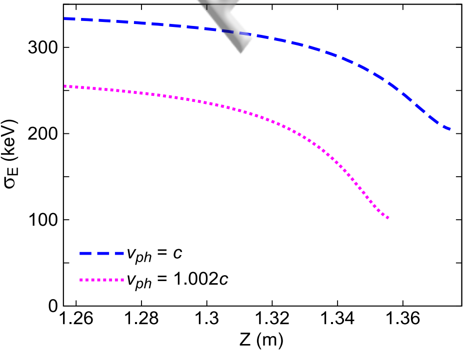
σ_E (keV)
300
200
100
0
$v_{ph} = c$
$v_{ph} = 1.002c$
1.26
1.28
1.3
1.32
1.34
1.36
Z (m)

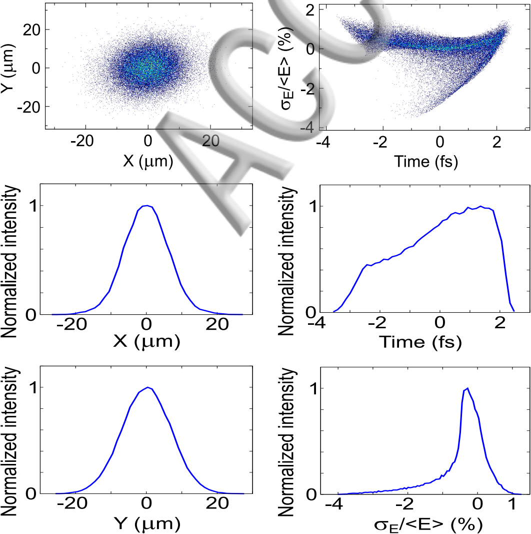
Y (μm)
X (μm)
20
0
-20
σ_E/<E> (%)
Time (fs)
2
-2
-4
Normalized intensity
1
0
X (μm)
Time (fs)
Y (μm)
σ_E/<E> (%)

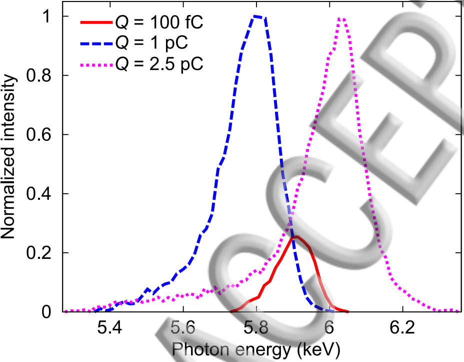
Q = 100 fC
Q = 1 pC
Q = 2.5 pC
Normalized intensity
0
0.2
0.4
0.6
0.8
1
5.4
5.6
5.8
6
6.2
Photon energy (keV)

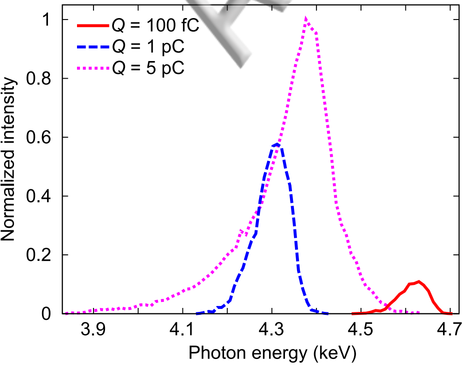
Q = 100 fC
Q = 1 pC
Q = 5 pC
Normalized intensity
0
0.2
0.4
0.6
0.8
1
3.9
4.1
4.3
4.5
4.7
Photon energy (keV)

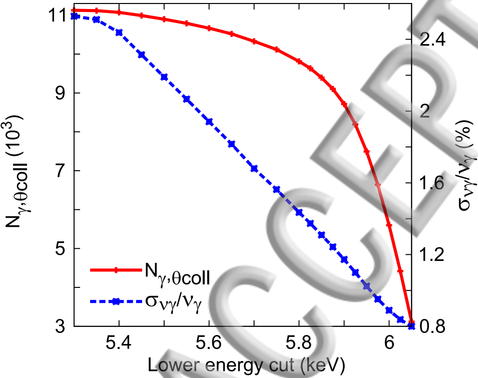
11
9
7
5
3
$N_{\gamma,\theta coll}$ (10^3)
2.4
2
1.6
1.2
0.8
$\sigma_{\nu\gamma}/\nu_\gamma$ (%)
5.4
5.6
5.8
6
Lower energy cut (keV)
$N_{\gamma,\theta coll}$
$\sigma_{\nu\gamma}/\nu_\gamma$

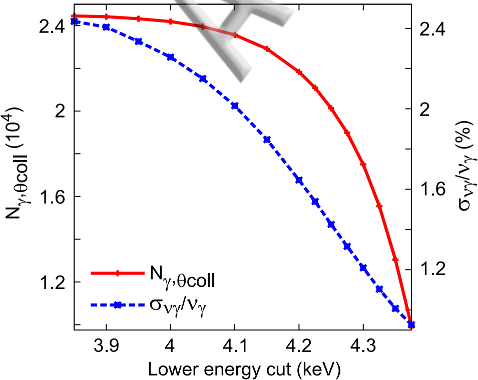
2.4
2
1.6
1.2
$N_{\gamma,\theta coll}$ (10^4)
2.4
2
1.6
1.2
$\sigma_{\nu\gamma}/\nu_\gamma$ (%)
3.9
4
4.1
4.2
4.3
Lower energy cut (keV)
$N_{\gamma,\theta coll}$
$\sigma_{\nu\gamma}/\nu_\gamma$

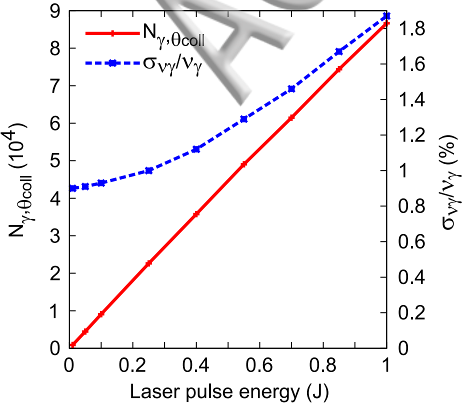
$N_{\gamma,\theta_{coll}}$
$\sigma_{\nu\gamma}/\nu_{\gamma}$
$N_{\gamma,\theta_{coll}}$ (10^4)
$\sigma_{\nu\gamma}/\nu_{\gamma}$ (%)
Laser pulse energy (J)
0
1
2
3
4
5
6
7
8
9
0
0.2
0.4
0.6
0.8
1
1.2
1.4
1.6
1.8
0
0.2
0.4
0.6
0.8
1

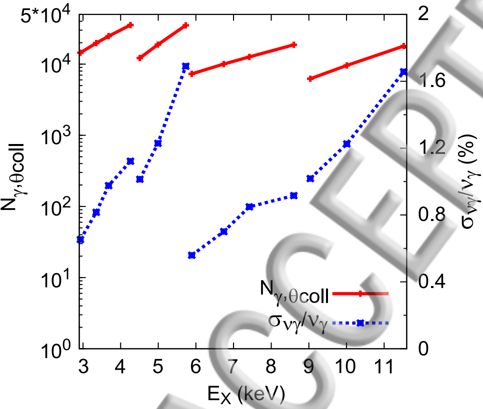
5*10^4
10^4
10^3
10^2
10^1
10^0
N_{γ,θcoll}
2
1.6
1.2
0.8
0.4
0
σ_{νγ}/ν_γ (%)
3 4 5 6 7 8 9 10 11
E_X (keV)
N_{γ,θcoll}
σ_{νγ}/ν_γ

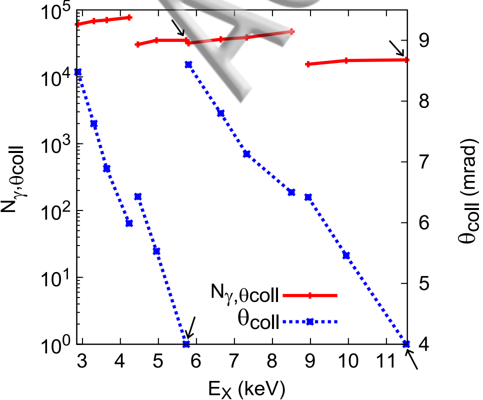
10^5
10^4
10^3
10^2
10^1
10^0
N_{γ,θcoll}
9
8
7
6
5
4
θ_coll (mrad)
3 4 5 6 7 8 9 10 11
E_X (keV)
N_{γ,θcoll}
θ_coll

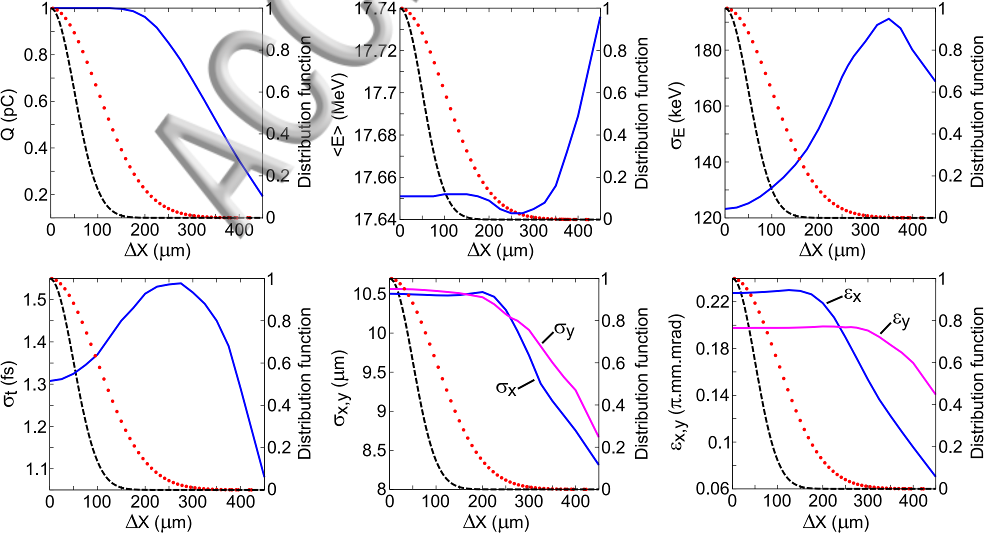
Q (pC)
1
0.8
0.6
0.4
0.2
0
100
200
300
400
ΔX (μm)
Distribution function
1
0.8
0.6
0.4
0.2
0
<E> (MeV)
17.74
17.72
17.7
17.68
17.66
17.64
σ_E (keV)
180
160
140
120
σ_t (fs)
1.5
1.4
1.3
1.2
1.1
$\sigma_{x,y}$ (μm)
10.5
10
9.5
9
8.5
8
σ_y
σ_x
$\varepsilon_{x,y}$ (π.mm.mrad)
0.22
0.18
0.14
0.1
0.06
ε_x
ε_y

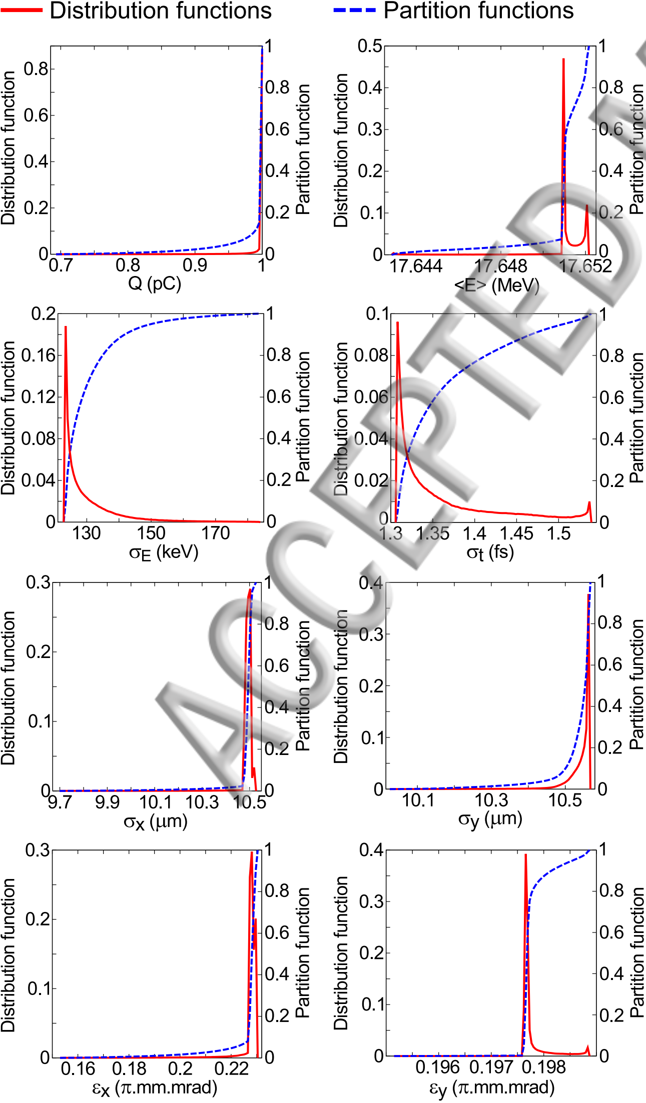
Distribution functions
Partition functions
Distribution function
Partition function
Q (pC)
0.7
0.8
0.9
1
<E> (MeV)
17.644
17.648
17.652
σE (keV)
130
150
170
σt (fs)
1.3
1.35
1.4
1.45
1.5
σx (μm)
9.7
9.9
10.1
10.3
10.5
σy (μm)
10.1
10.3
10.5
εx (π.mm.mrad)
0.16
0.18
0.2
0.22
εy (π.mm.mrad)
0.196
0.197
0.198

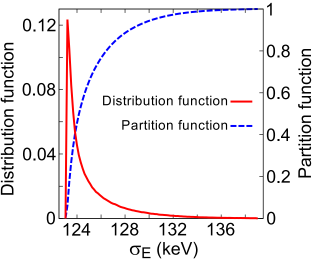
0.12
0.08
0.04
0
Distribution function
124
128
132
136
σ_E (keV)
1
0.8
0.6
0.4
0.2
0
Partition function
Distribution function
Partition function

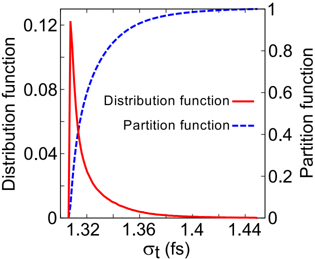
0.12
0.08
0.04
0
Distribution function
1.32
1.36
1.4
1.44
σ_t (fs)
1
0.8
0.6
0.4
0.2
0
Partition function
Distribution function
Partition function

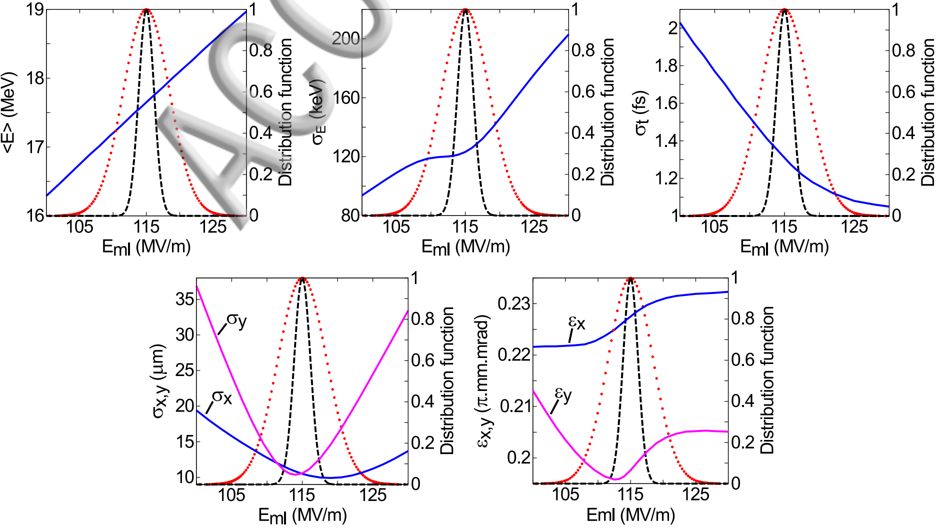
<E> (MeV)
16
17
18
19
σE (keV)
80
120
160
200
σt (fs)
1
1.2
1.4
1.6
1.8
2
Distribution function
0
0.2
0.4
0.6
0.8
1
Eml (MV/m)
105
115
125
σx,y (μm)
10
15
20
25
30
35
σy
σx
εx,y (π.mm.mrad)
0.2
0.21
0.22
0.23
εx
εy

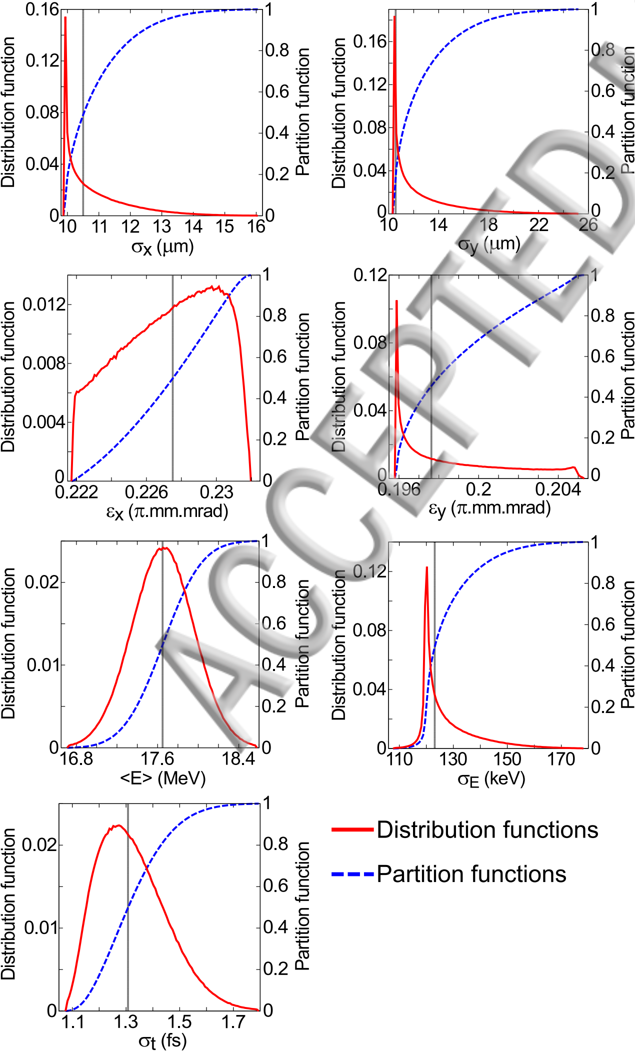
Distribution function
Partition function
σX (μm)
σy (μm)
εX (π.mm.mrad)
εy (π.mm.mrad)
<E> (MeV)
σE (keV)
σt (fs)
Distribution functions
Partition functions

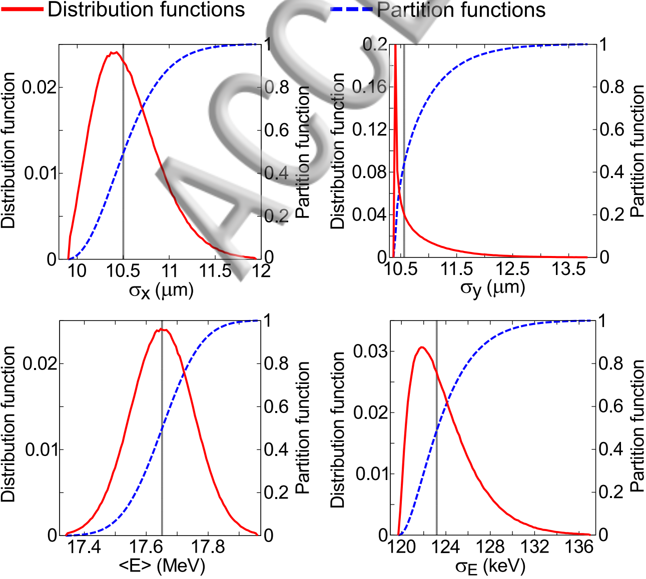
Distribution functions
Partition functions
Distribution function
Partition function
0.02
0.01
0
1
0.8
0.6
0.4
0.2
0
10
10.5
11
11.5
12
σx (μm)
0.2
0.16
0.12
0.08
0.04
0
10.5
11.5
12.5
13.5
σy (μm)
0.02
0.01
0
17.4
17.6
17.8
<E> (MeV)
0.03
0.02
0.01
0
120
124
128
132
136
σE (keV)

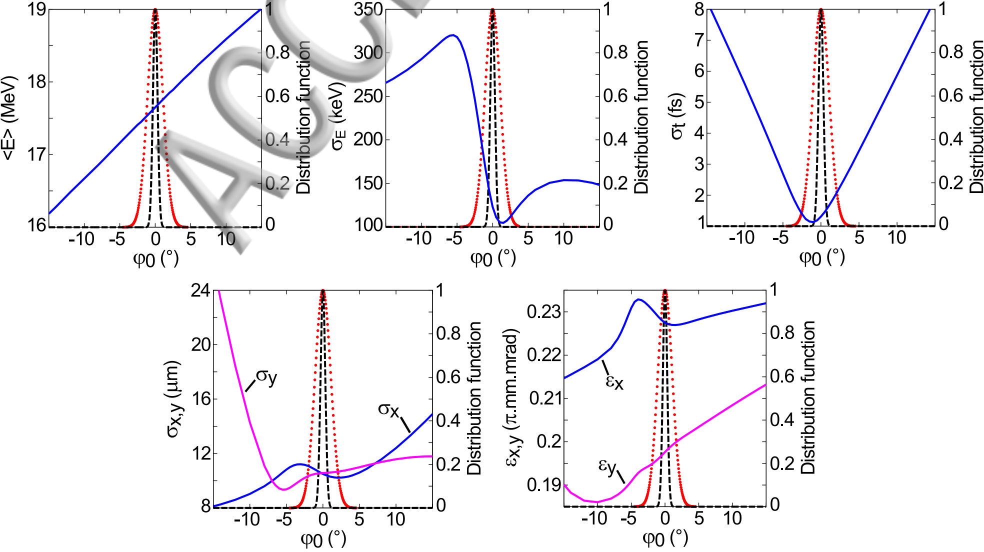

<E> (MeV)
19
18
17
16
-10
-5
0
5
10
φ0 (°)
Distribution function
1
0.8
0.6
0.4
0.2
0
σ_E (keV)
350
300
250
200
150
100
σ_t (fs)
8
7
6
5
4
3
2
1
$\sigma_{x,y}$ (μm)
24
20
16
12
8
σ_y
σ_x
$\varepsilon_{x,y}$ (π.mm.mrad)
0.23
0.22
0.21
0.2
0.19
ε_x
ε_y

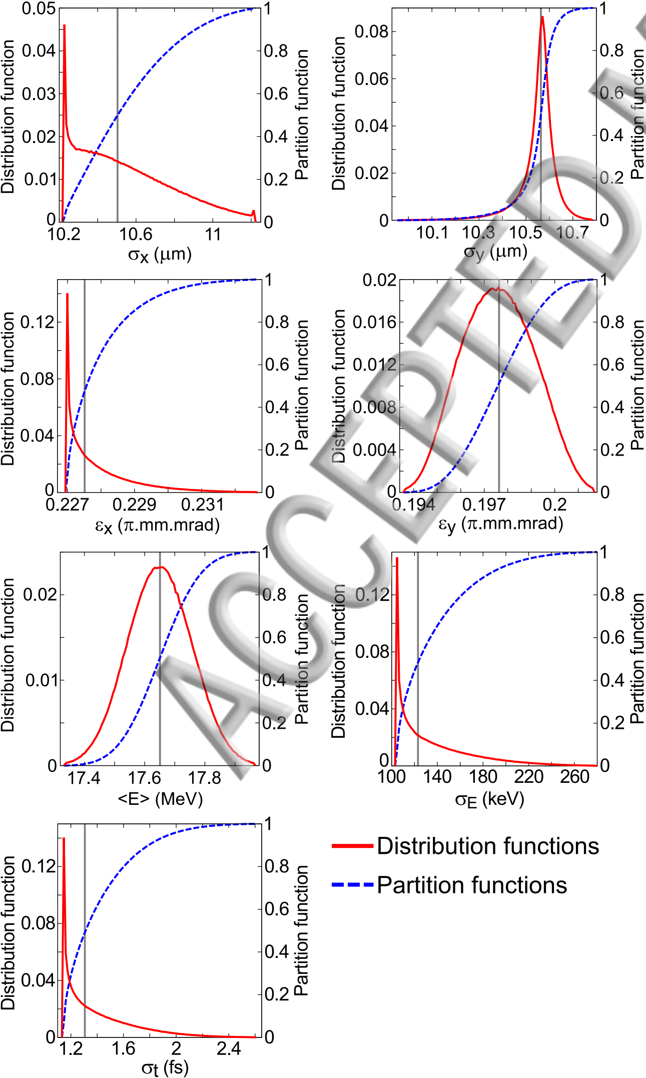

Distribution function
Partition function
σx (μm)
10.2
10.6
11
0
0.01
0.02
0.03
0.04
0.05
0.2
0.4
0.6
0.8
1
σy (μm)
10.1
10.3
10.5
10.7
0.02
0.04
0.06
0.08
εx (π.mm.mrad)
0.227
0.229
0.231
0.04
0.08
0.12
εy (π.mm.mrad)
0.194
0.197
0.2
0.004
0.008
0.012
0.016
0.02
<E> (MeV)
17.4
17.6
17.8
0.01
0.02
σE (keV)
100
140
180
220
260
0.04
0.08
0.12
σt (fs)
1.2
1.6
2
2.4
0.04
0.08
0.12
Distribution functions
Partition functions

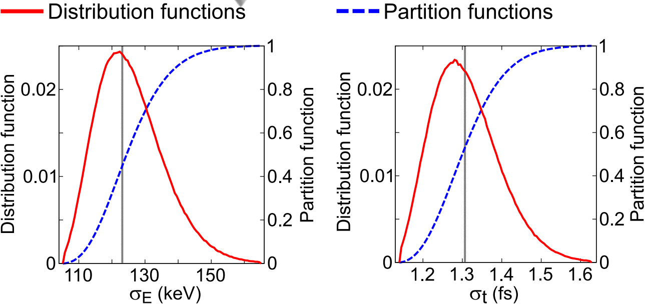
Distribution functions
Partition functions
Distribution function
Partition function
0
0.01
0.02
0
0.2
0.4
0.6
0.8
1
110
130
150
σE (keV)
Distribution function
Partition function
0
0.01
0.02
0
0.2
0.4
0.6
0.8
1
1.2
1.3
1.4
1.5
1.6
σt (fs)

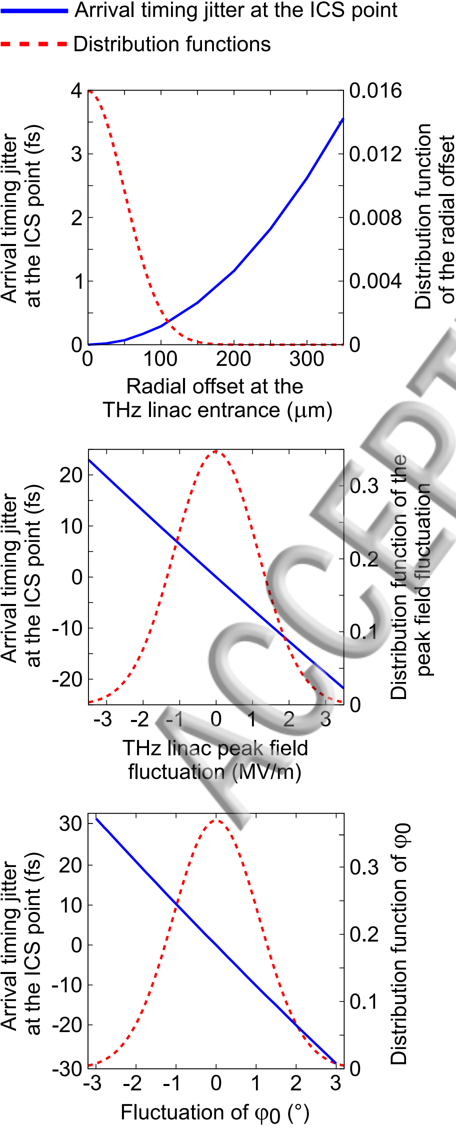
Arrival timing jitter at the ICS point
Distribution functions
Arrival timing jitter at the ICS point (fs)
Distribution function of the radial offset
Radial offset at the THz linac entrance (μm)
0
1
2
3
4
0
0.004
0.008
0.012
0.016
0
100
200
300
Arrival timing jitter at the ICS point (fs)
Distribution function of the peak field fluctuation
THz linac peak field fluctuation (MV/m)
-20
-10
0
10
20
0
0.1
0.2
0.3
-3
-2
-1
0
1
2
3
Arrival timing jitter at the ICS point (fs)
Distribution function of φ0
Fluctuation of φ0 (°)
-30
-20
-10
0
10
20
30
0
0.1
0.2
0.3
-3
-2
-1
0
1
2
3